ABSTRACT

CRITES, ERIN LYNNE. Impacts on Polymer Composites from the Photothermal Heating of Metallic, Organic, and Carbonaceous Nanoparticles (Under the direction of Dr. Laura Clarke and Dr. Jason Bochinski).

Photothermal heating is a process where nanoparticles convert light into heat. In composites, photothermal heating can be used to create heterogeneous heating patterns within a system, such that there are high temperatures near the particle, but the sample is cool far away from the particle. This dissertation explores the wide applications in selective treatment and heating control that photothermal heating allows, while also investigating the heating differences in metallic, organic, and carbonaceous nanoparticles. This will be done in three polymer/nanoparticle systems. The first uses multi-walled carbon nanotubes (MWCNTs) as a conductive filler, and demonstrates photothermal heating as a post-manufacturing process to increase the conductivity. From experimental data and a simple heat transport model, the conductivity increase is shown to be driven by the local temperature around the MWCNT percolating pathway. The second system investigates the deswelling behavior of hydrogels placed under conventional and photothermal heat from two types of nanoparticles. The photothermal heating effects of gold nanoparticles are compared to melanin nanoparticles (a more biologically friendly nanoparticle). It is seen that while the MNPs may be a less efficient heater, MNPs are able to drive the deswelling process similarly to the GNPs. An additional comparison of the metallic (GNP) and organic (MNP) nanoparticles is done in the third system, where both nanoparticles are embedded into poly(vinyl alcohol). The degradation signals of PVA are monitored during photothermal heating and compared to conventional heating in a low temperature oven. A universal degradation process is observed in both bulk PVA (conventional and photothermal heating) and in the MNP themselves.

Impacts on Polymer Composites from the Photothermal Heating of Metallic, Organic, and Carbonaceous Nanoparticles

By
Erin Lynne Crites

A dissertation submitted to the Graduate Faculty of
North Carolina State University
in partial fulfillment of the
requirements for the degree of
Doctor of Philosophy

Physics

Raleigh, North Carolina
2025

APPROVED BY:

_____	_____
Dr. Laura Clarke	Dr. Jason Bochinski
Co-Chair of Advisory Committee	Co-Chair of Advisory Committee
_____	_____
Dr. Karen Daniels	Dr. Thomas Schroeder
_____	
Dr. Keith Weninger	

BIOGRAPHY

Erin Crites was raised in Orlando, Florida and was encouraged from a young age to be curious about the world. This joy of learning led her through classes in science, math, pottery, drawing, bookbinding, and many more. She chose to study physics for her bachelor's degree at the University of Central Florida and truly began her journey in research when she began to work in Dr. Michael Chini's ultrafast laser lab. She enjoyed taking part in the scientific process, from the initial conception and rough setups in the lab to the presentation of the work at conferences. She moved to North Carolina in 2020 to attend graduate school at North Carolina State University, where she broadened her research to encompass polymer science.

Erin loves to spend her time in the sunshine, petting dogs, and doing crafts with friends. She plans to continue her quest to learn obscure skills both in her career as a scientist and her personal life.

FUNDING ACKNOWLEDGMENTS

This material is based upon work supported by the National Science Foundation Graduate Research Fellowship Program under Grant No. DGE-2137100. Any opinions, findings, and conclusions or recommendations expressed in this material are those of the author(s) and do not necessarily reflect the views of the National Science Foundation.

This work was performed in part at the Analytical Instrumentation Facility (AIF) at North Carolina State University, which is supported by the State of North Carolina and the National Science Foundation (award number ECCS-2025064). The AIF is a member of the North Carolina Research Triangle Nanotechnology Network (RTNN), a site in the National Nanotechnology Coordinated Infrastructure (NNCI).

PERSONAL ACKNOWLEDGMENTS

Like so many others, my journey in physics began with a phenomenal high school physics teacher. Thank you, Ms. Carroll Stoner, for dropping watermelons off bleachers and calculating the index of refraction of food. Your class really taught me about the joy of science.

I would not be in graduate school without the guidance and support from Dr. Michael Chini. Thank you for giving a shy (but curious!) undergraduate student a chance to do a summer research project that turned into three years. Thank you for pushing me towards opportunities to write and present, and for mentoring me in both how to think like a researcher and in preparing for a career in science.

My PhD was done in a community that I am profoundly grateful for.

To Mom: thank you for teaching us from the beginning to not be afraid of math and science, but also for signing me up for whatever weird art classes I wanted to try next.

To Dad: thank you for pulling out all the tools when I decide I want to build a shelf, or make magnets, or design a coat hanger.

To Amy: thanks for trading pictures of our wonderful silly dogs and talking about books and proofreading emails.

To Sonali, Roman, and Zain: you all made my bachelor's degree so much fun. Thanks for the weekly catchups and long-distance games and internet analysis.

To LauraGrace and Dane: thanks for being such excellent sources of gossip and for all the laughter around board games and dinners. LG, I can't wait to make so many silly little crafts with you and discuss terrible books in between the excellent books.

To Carmen: thanks for the new pottery hobby and the (more dangerous) knitting hobby. I'm so thankful our timing here lined up like it did.

To Caroline: you are absolutely incredible, and I am so happy that our paths crossed. Thank you for being there in the hard times and for knowing so many people (still hilarious) and for proofreading and for discussing baking techniques. You are such a bright spot in my graduate journey, and I am so, so thankful to call you a friend.

To Geoff: you should get an honorary degree, frankly. I could fill another dissertation about how this wouldn't have happened without you. Thank you for everything.

To Koda, Lola, Bart, and Jim: you are all so cute and so silly. Thank you for letting me force my affection onto you.

I would finally like to acknowledge the NCSU Craft Center, which has cultivated such a welcoming community and provided a space to be creative and learn. I managed to take a class in nearly every studio during my PhD, and had so much fun doing so. (Everyone should go to the Craft Center!)

TABLE OF CONTENTS

ABSTRACT i
BIOGRAPHY ii
FUNDING ACKNOWLEDGMENTS iii
PERSONAL ACKNOWLEDGMENTS iv
TABLE OF CONTENTS v
LIST OF FIGURES vii
LIST OF TABLES xiv
Chapter 1 1
1.1 Optical Properties of Nanoparticles 1
1.2 Photothermal Heating Mechanisms 2
1.3 Photothermal Applications 7
Chapter 2: Photothermal heating to improve particle-particle contacts and electrical conductivity in MWCNT: polymethyl methacrylate composites 10
2.1: Conductive Composites and Carbon Nanotubes 10
2.2 Material and Methods 14
2.2.1 Materials and Sample Preparation 14
2.2.2 Sample Characterization 16
2.2.3 Photothermal Treatment 18
2.2.4 Conventional Heating 19
2.3 Results and Discussion 19
2.3.1. Basic Composite Properties 19
2.3.2. Increase in Conductivity due to Photothermal Heating 21
2.3.3. Effect of particle concentration 25
2.3.4. The role of T_{local} 28
2.3.5. Visualization of the Network and Matrix Stability 35
2.4 Conclusions 38
Chapter 3: Water Evaporation from Hydrogels via Photothermal heating of Nanoparticles 40
3.1 Hydrogels 40
3.2 Materials and Methods 43
3.2.1 Hydrogel Synthesis 43

3.2.1 Nanoparticle Synthesis 45
3.2.3 Thermal Treatment 47
3.3 Characterization of the Hydrogel System 48
3.3.1 Basic Swelling and Deswelling Behavior 48
3.3.2 Particle Concentrations and Length Scales 53
3.4 Hydrogel Deswelling 56
3.4.1 Simple Deswelling Behaviors 57
3.4.2 Impact of Heat on Water Output 66
3.5: Conclusions and next steps 75
Chapter 4: Degradation of PVA and Melanin Nanoparticles under Photothermal Heating 78
4.1: Melanin Nanoparticles and Polymer Degradation 78
4.2: Materials and Methods 80
4.3: Results 85
4.3.1 Absorption, Mass, and Temperature 86
4.3.2 Universal Luminescence from Degradation 91
4.3.3 Chemical Structure Changes from Thermal Treatment 98
4.4 Conclusion 106
Chapter 5: Conclusions 107
5.1 Conclusions and Outlook 107
5.2 New Directions 110
REFERENCES 112

LIST OF FIGURES

Figure 1: Schematic of the LSPR. The gold circles represent a metallic nanosphere. As the light creates an electric field around the particle, the electron cloud on the surface of the nanoparticle begins to move with the electric field, generating a resonance effect that increases the absorption at the light's wavelength. Energy absorbed by the nanoparticle may exit as heat. 2

Figure 2: Sketch of photothermal particles (gold circles surrounded by a red gradient to represent heat) interacting with light (blue squiggles). A general temperature profile from the photothermal heating is shown with a red line. 7

Figure 3: Cartoon of the goals of CNT:polymer composites. a) depicts the desire for a dispersed network, which can be solved by adding a surfactant. However, b) displays the desire for good nanotube contact, which is necessarily reduced with the addition of surfactant. 10

Figure 4: 0.125 wt% MWCNT composite conductivity versus the age of the sonicated MWCNT/Triton-X/DMF solution used to make the samples. Average conductivity (over all samples) was $2.5\times10^{-4} \pm 3.0 \times10^{-4}$ S/cm. Sample thickness was approximately 0.06 mm. 15

Figure 5: a) Optical extinction of MWCNT:PMMA composites. Characteristic broad absorption from MWCNTs increases with increasing nanotube concentration with minimal contribution from PMMA in the visible range. The vertical line represents the illumination of the 450 nm source for photothermal heating. b) Transmission through the sample at 450 nm for varying MWCNT loading. c) Transmission through 0.125 wt% MWCNT:PMMA samples at 450 nm for different thicknesses of the sample. . 17

Figure 6: 0.125 wt% MWCNT composite conductivity versus photothermal heating time. The fit line has a time constant of 0.52 hours 18

Figure 7: a) Characteristic current versus voltage scans for 0.125 wt% (black squares) and 0.250 wt% (red circles) MWCNT:PMMA composites. Inset: Photo of characteristic 0.125 wt% sample. b) Conductivity versus volume fraction (black squares). Percolation model (dotted line). Inset: power law scaling used to determine crit and β (see text).20

Figure 8: Relative conductivity (i.e., the ratio of final to initial conductivity) for different MWCNT concentrations and laser intensity. Points are slightly offset in laser intensity to aid in viewing. The data at each concentration is limited to a maximum laser intensity where the global temperature reached ~110 °C (above the PMMA T_g) and bulk sample deformation occurred. Cases where the sample deformed (e.g., intensities greater than

0.55 W/cm^2 for 0.125 wt% MWCNT: PMMA or 0.34 W/cm^2 for 0.5 wt% MWCNT:PMMA) are not included and were associated with lower relative conductivity gain, as discussed in greater detail below. The largest conductivity increase occurs for moderate (0.125-0.25 wt%) loading exposed to the highest laser intensity possible without bulk deformation. Sample measurement consistency is visible in the 0 W/cm^2 point, where an untreated sample was repeatedly measured over multiple days. 20

Figure 9: Measured global (bulk) temperature at a given laser intensity. All samples experience solidification in an oven at 65 °C during fabrication. Below T_g, temperature has a roughly linear dependence on laser intensity, with a slope that increases with MWCNT concentration 22

Figure 10: Relative conductivity increase versus laser intensity, plotted by global temperature group. Each temperature range contains samples of varying MWCNT concentrations and laser intensities that were measured to have the same bulk temperature during photothermal treatment. The overlapping plots indicate that conductivity change is not determined by global temperature during treatment. A linear fit from 0.25 W/cm^2 – 0.55 W/cm^2 is applied to all data (solid black line). 23

Figure 11: Conductivity for 0.125 wt% samples before treatment with varying thicknesses. Thickness does not significantly impact the starting conductivity of the sample..... 26

Figure 12: a) Relative conductivity increase and b) global treatment temperature versus thickness for 0.125 wt% MWCNT samples due to photothermal treatment for 1 hour at 0.35 W/cm^2. Thinner samples exhibited lower conductivity increases, likely due to heat transport along MWCNTs in contact with the sample surface. For thicker samples, MWCNTs on the light-entry side may shadow those deeper in the composite, leading to non-uniform photothermal heating and thus a reduced response. 27

Figure 13: a) Model of the MWCNT network from above showing individual MWNCT (black lines) and one sample-spanning path. The matrix relatively close to the sample spanning pathway (shown in red) is considered heated to T_{local} in this simple model. The meandering tube where $T = T_{local}$ has order of magnitude dimensions with the characteristic radius set to the MWCNT length and characteristic length set to the sample dimension. b) The approximated temperature profile in a cross section showing a linear temperature difference between T_{local} and T_{global}. 29

Figure 14: Relative conductivity versus estimated local temperature near the effective internal heater formed by the MWCNT network (from the model described in text) for four different MWCNT concentrations. The PMMA T_g of 105 °C is indicated by a vertical line. For 0.125 wt% samples, three different external conditions (ambient, forced

convection with a fan, and elevated temperature represented by black diamonds, open circles, and open left pointing triangles, respectively) were utilized to tune the temperature profile, while keeping MWCNT concentration and light intensity constant. This enabled a clearer delineation of the role of T_{local}. The 0.0625 wt% (blue squares), 0.25 wt% (red upward triangles), and 0.5 wt% (green downward triangles) composites were treated under ambient conditions. Error bars indicate standard deviation of average conductivity change for samples with similar local temperatures..... 31

Figure 15: FTIR of 0.125 wt% samples before and after photothermal treatment at 0.35 and 0.55 W/cm^2. Plot is normalized to 1140 cm^{-1} (corresponding to C-O) for ease of viewing. Vertical dashed lines indicate 1088 and 1676 cm^{-1}, which are associated with DMF (C-N and C=O bonds, respectively) and decrease with treatment, as the T_{boil} of DMF is 153 °C and local temperatures are estimated to approach that (0.35 W/cm^2 had estimated local temperatures of 110 °C, while 0.55 W/cm^2 had estimated local temperatures of 140 °C. Peaks associated with PMMA, such as 1721 cm^{-1} (C=O stretching), 1432 cm^{-1} (CH_3 stretching), and 1189 cm^{-1} (-OCH_3 stretching), remain unchanged with treatment, suggesting no PMMA degradation from photothermal treatment 36

Figure 16: Transmission electron micrographs of MWCNT:PMMA composite samples showing the distribution of nanotubes. a) 0.125 wt% untreated, b) 0.125 wt% treated with 0.45 W/cm^2 for one hour, c) 0.25 wt% untreated, d) 0.25 wt% treated with 0.5 W/cm^2 for one hour. Figure a) includes a cluster of tangled nanotubes mentioned in the text. Images were analyzed by measuring the size of individual nanotubes and counting tangled clusters of nanotubes. 37

Figure 17: Photo of a) dried hydrogel powder and b) swollen hydrogel 43

Figure 18: Microhydrogel diameter as measured from microscope images of powder (inset). ... 45

Figure 19: Extinction of stock solutions of GNP and MNP, normalized to the laser wavelength at 520 nm. TEM images of b) GNP and c) MNP. 46

Figure 20: Depiction of hydrogel on string for treatment. The laser beam is expanded to cover the entire hydrogel, which is suspended on a string that is stretched over a petri dish. ... 48

Figure 21: Images of a swollen hydrogel at a) Q=6, b) Q=12, and c) Q=24, made by adding the appropriate amount of water to dried hydrogel powder, mixing, and allowing it to sit for several minutes until the powder had fully absorbed the water. The hydrogel becomes increasingly translucent with the addition of water, but also loses structural integrity. d) Swelling value over time when hydrogel powder is placed in a dialysis bag and allowed to freely absorb water. 49

Figure 22: DLS measurement of heated swollen hydrogel. The large error bars are an artifact of the lack of uniformity of the hydrogel particles, as DLS measurements are not well suited to particles with large polydispersity..... 51

Figure 23: Deswelling of hydrogels with varying surface areas. There is a steady increase in the time for 50% of the water to come out with increasing overall surface area..... 52

Figure 24: Images taking during the deswelling process of a Q=6 hydrogel in a) ambient conditions and b) with embedded GNP undergoing photothermal heating. There is a 0.5 cm by 0.5 cm grid pictured behind the hydrogels..... 57

Figure 25: The a) evaporated water and b) temperature over deswelling time. Points are averaged within groups of data within 30 minute increments. The horizontal line in b) marks room temperature. 58

Figure 26: Sketch of how local temperatures contribute to the global temperature, such that (a) nanoparticles with more separation will result in a lower global temperature than (b) nanoparticles with less separation. c) Temperature of a GNP hydrogel undergoing photothermal heating plotted against the swelling throughout the deswelling process. Initial temperature data (when the laser was not on) is removed. In this plot, increasing treatment time goes from left to right. The temperatures for different hydrogel swellings collapse onto a similar curve, regardless of the initial swelling. 60

Figure 27: a) Time for 50% of the water to be removed from the hydrogel under various heating conditions. b) Swelling Q over time for initial Q=6 to Q=40 hydrogels in a 33 °C oven. 61

Figure 28: Diagram of water (blue circles) bonded to NIPAM. 62

Figure 29: a) The evaporated water over time and b) temperature of hydrogels in ambient conditions at multiple swellings. The swelling dependence is less than the impact on humidity level, as the humidity drives the water loss in this hydrogel system..... 64

Figure 30: Time for 50% of water to leave the hydrogel for different humidities. Only the hydrogels at ambient conditions display any dependence on the humidity; any applied heat drives the water loss more effectively than the humidity of the environment is able to. 65

Figure 31: Swelling over time for varying oven temperatures. A warmer oven results in a higher rate of water evaporation, which is expected, and indicates the hydrogel is not interfering with the deswelling process. 66

Figure 32: a) Temperature of and b) water evaporated from the hydrogel versus time during photothermal treatment with variable quantities of particles. More nanoparticles increased the temperature and consequently increased the water output at a given time. 67

Figure 33: The natural log of the rate vs inverse temperature of conventionally and photothermally heated cases, using the average measured temperature during photothermal heating. Linear fits allow for the calculation of activation energy for removing water from the hydrogels. E_a is calculated to be 31.5 ± 3.4 kJ/mol, 52.6 ± 11.9 kJ/mol, 74.8 ± 6.5 kJ/mol for oven, GNP photothermal heating, and MNP photothermal heating, respectively. 69

Figure 34: Natural log of the rate versus inverse temperature of conventionally and photothermally treated hydrogels, now with the maximum recorded temperature from the photothermally heated samples. E_a for dotted line (all samples) is 37.0 ± 0.2 kJ/mol 70

Figure 35: Sketch of the way the temperature profile within the hydrogel may change for close together particles. 71

Figure 36: The percent water evaporated over time for Q=12 cases, with points labeled as either the first half of deswelling (solid shapes) or second half (open shapes). The slope of these regions, when compared to each other for a given heating method, are indicators of changes in the dewatering process. 72

Figure 37: The a) rate of water evaporation versus the average temperature during the period of deswelling. A linear fit of a) was used to calculate the b) percent difference of the rate of deswelling at a given temperature. Data from the first time interval is presented as solid shapes, while the second interval is presented with open markers. 73

Figure 38: Diagram of the case hardening effect in an oven heated hydrogel and photothermally heated hydrogel. In an oven, a hydrogel (a) is exposed to heat (b). Water from the edges is removed (c), creating a hydrophobic shell (d) until the hydrogel cools or otherwise reswells (e) In contrast, a hydrogel with nanoparticles (f) has heat throughout the system (g), allowing water to exit without the formation of shell on the edge of the polymer (h). 74

Figure 39: a) Absorption of the four fluorophores in solution used to measure and calculate b) the G-factor. The G-factor is a wavelength-dependent intensity correction used in the calculation of the r-factor. 84

Figure 40: PVA sample treated at 145 °C for 0 hour to 69 hours. With treatment, the sample yellows and eventually browns. 86

Figure 41: Absorption spectra of PVA treated in an oven at a) 110 °C, b) 145 °C, and c) 183 °C for variable amounts of time, as determined by the treatment temperature. The visual yellowing of the sample is represented by the formation of an absorption wall centered at 480 nm. Noisy signal near an extinction of 4 indicates a maximum measurement of the equipment..... 87

Figure 42: Absorption spectra of a) GNP and b) MNP. Both spectra include characteristic signals from the nanoparticles - a 555 nm peak from the GNP, and a broad absorption signal from the MNP (250 nm – 1100 nm). Noisy signal near an extinction of 4 indicates a maximum measurement of the equipment. 88

Figure 43: Bulk temperature measured during photothermal treatment for both GNP and MNP. Error bars for PVA-GNP samples are calculated from the standard deviation of temperature measurements across multiple samples at a given time treated. 90

Figure 44: The PVA chemical structure. 92

Figure 45: Luminescence measurements for a) 110 °C, b) 145 °C, and c) 183 °C treated PVA samples. The degradation luminescence is associated with a broad increase in luminescence, shift in wavelength, then decrease in luminescence. This is primarily seen in the higher temperature treatments, as the low temperature is not enough to fully degrade the PVA. 93

Figure 46: R-factor for the a) 145 °C and b) 183 °C oven treated PVA at both 423 nm (near the innate luminescence) and 555 nm (the final location of the degradation luminescence). For each data point, the intensity of the luminescence signal was extracted at the appropriate wavelength and used in Equation 11. Although the 183 °C oven was measured at longer treatment times, the signal was below the background noise level of the equipment for one of the polarization components, and thus unsuitable for an r-factor calculation. 94

Figure 47: Fluorescence throughout photothermal treatment for a) GNP-PVA and b) MNP-PVA. c) The r-factor of the GNP and MNP treated samples at 475 nm, which is expected to be the degradation peak for photothermal treatment. For each data point, the intensity of the fluorescence signal was extracted at the appropriate wavelength and used in Equation 11. For the 42 hour MNP photothermal treatment, the signal was below the noise level of the machine for one of the polarization components at this wavelength, and thus unsuitable for an r-factor calculation. d) Peak intensity of the PVA-MNP fluorescence. Between 21 and 23 hours of thermal treatment, the peak intensity switches from indicating the MNP (0-21 hours) to indicating the PVA universal degradation fluorescence (23-42 hours)..... 96

Figure 48: The peak location measured at different treatment times, with preference given for the degradation peak. Peak location is found at the highest intensity value of a smoothed luminescence curve. Time is normalized to the final time the sample was treated to. All samples start at the same innate PVA luminescence wavelength, except for the MNP-PVA samples, as the MNP overpowered the innate PVA luminescence. For the MNP-PVA sample, the first half of the data points correspond to the MNP, while the second half correspond to the PVA degradation luminescence. 98

Figure 49: FTIR spectra for all samples. Vertical lines are placed at the notable wavenumbers of (from left to right) 1710,1576, 1141, 1095, 1089, and 1022 cm^{-1}. 100

Figure 50: Crystallinity ratio for all thermally treated samples, plotted with time normalized to the end of the treatment process. 101

Figure 51: Chemical diagram showing the potential restructuring of bonds with PVA during degradation. a) As energy enters the system, the polymer side group undergoes oxidation (loss of an electron or hydrogen) of the side chains. The radicals are then able to either form C=O bonds or b) C-O-C crosslinking bonds. Based on work by Ref [206,212]. 102

Figure 52: Tracking the C=O peak at 1710 cm^{-1} over normalized time to the end of the treatment process. The photothermal treated cases show an immediate increase in C=O, with the 183C oven treated sample following after an initial decrease indicating a removal of PVAc. The two lower oven temperatures did not ever reach the same final amounts of C=O bonds, as indicated by the comparatively lower ratio values. 103

Figure 53: Transmission peak at 1576 cm^{-1} over time for all treatment cases. The 110 °C continues at the same level for the entire treatment time and is not included to ensure visibility of data at lower time scales. 104

LIST OF TABLES

Table 1: Features in TEM images of 0.125 wt% samples treated at 0.6 W/cm^2. 38

Table 2: Hypothetical gold nanoparticle concentration in hydrogel of different swellings using hydrogel with 2.46×10^{10} particles per gram polymer 53

Table 3: Experimental gold nanoparticle concentration in hydrogel of different swellings made by varying the number of particles per polymer 54

Table 4: Mass loss of PVA exposed to different treatment times, temperatures, and methods.... 89

Table 5: Swelling test of PVA after thermal treatment..... 105

Chapter 1

1.1 Optical Properties of Nanoparticles

Imagining gold or silver objects brings to mind warm yellows or a reflective grey color. However, when these materials are used to create nanoscale objects, there are dramatic changes in the optical properties. The Lycurgus Cup is a famous example of such properties, as a glass made in 4th-century Rome that appears green in reflected light, but dramatically switches to red when illuminated from behind [1,2]. We understand today that gold and silver nanoparticles dispersed throughout the glass provide its unique color properties [3,4].

The mechanisms behind these optical properties are relatively well understood for metallic nanoparticles [5,6]. Metallic nanoparticles, such as gold [7], silver, or platinum nanoparticles, have a localized surface plasmon resonance (LSPR). When light interacts with the nanoparticle at a wavelength corresponding to the LSPR, the free electrons within the particle begin to resonate and absorb the energy of the light. The most obvious manifestation of this is the visual appearance of a nanoparticle solution, as the color of the solution is dependent on the LSPR location [8–11], which corresponds to the peak absorption of the nanoparticles. This light-nanoparticle interaction also leads to a useful application- the absorbed energy can exit the nanoparticle as heat [5,6,12].

This process is called photothermal heating, and can occur in a wide variety of nanoparticles, including carbon nanotubes and melanin nanoparticles used later in this work. Although these carbon-based materials do not have a LSPR, they still absorb light, do not have a mechanism to expel that energy as light, and thus release heat instead. The mechanisms by which the heat is released, as well as the variety of nanoparticles that release it, make photothermal heating an interesting process to study and useful tool in a range of applications.

1.2 Photothermal Heating Mechanisms

The vast selection of nanoparticles available means that when choosing nanoparticles for a system, one must consider characteristics such as the shape, size, material, solubility, toxicity, cost, and more. Furthermore, the mechanisms driving the photothermal conversion process depends on the material, thus allowing further tailoring of the nanoparticle for the environment. This section will describe the three photothermal conversion mechanism that arise from different material families – metallic, semiconductor, and carbon-based materials – and notable characteristics of nanoparticles within each group.

Perhaps the most common and most utilized nanoparticles for photothermal heating are plasmonic metallic nanoparticles, such as gold, silver, and platinum. As previously discussed, these nanoparticles have a localized surface plasmon resonance (LSPR) based on the size, shape, and material of the nanoparticle [9,13–17]. When light hits a metallic nanoparticle, the nanoparticle absorbs photons at the same frequency as the LSPR. Free electrons within the metallic structure are brought to the surface of the nanoparticle and begin to oscillate with the light wave

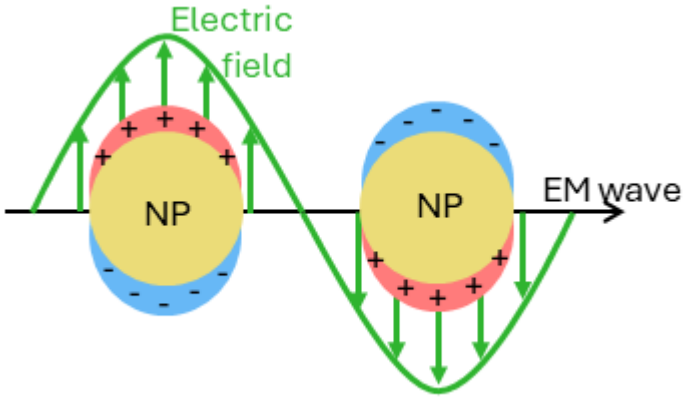

Figure 1: Schematic of the LSPR. The gold circles represent a metallic nanosphere. As the light creates an electric field around the particle, the electron cloud on the surface of the nanoparticle begins to move with the electric field, generating a resonance effect that increases the absorption at the light's wavelength. Energy absorbed by the nanoparticle may exit as heat.

(Figure 1). Electron-hole pairs are generated and undergo electron-electron collisions that convert the energy into heat, resulting in photothermal heating [5,6,12,18].

Nanoparticles with LSPR have relatively narrow wavelength ranges that they strongly absorb, ranging on the order 100 nm depending on the particle size distribution, as compared to the absorption across the entire visible spectrum seen by carbon-based particles. This can be either a limiting factor or a benefit. For example, LSPR allows photothermal heating to be activated only when a specific wavelength is present, creating a useful 'switch' to control the heat. However, this is only useful if that light source is accessible, and often limits these nanoparticles to laboratory settings, as using a broad light source (like the Sun or a lamp) includes energy that is not usable for photothermal conversion by the nanoparticles. When the wavelength of the light source matches the nanoparticle absorption, the photothermal conversion efficiency (describing the amount of the input energy that is been converted to heat) can be very high. This is particularly notable in the example of gold nanoparticles [19–21], which have been reported to reach 100% of light energy converted into heat [22,23].

The specific wavelength used can be highly tailored for a desired application. As mentioned earlier, the size, shape, and material of the nanoparticle could all be modified to control the interaction with light [9,13–17]. Even simply changing the orientation of an asymmetric nanoparticle with respect to the incident light polarization can result in an anisotropic heating response [24], which would allow for fine-tuned control of the locations of heating. Furthermore, metallic nanoparticles can also be synthesized into a variety of unique shapes, such as spheres [25,26], rods [11,15,16,27], stars [28,29], cubes [30,31], and triangles [32–34], which all correspond to unique light-matter interactions.

Two significant drawbacks to using metallic nanoparticles in applications come from the cost and toxicity. Metallic nanoparticles are a comparatively more expensive nanoparticles than carbon-based or organic nanoparticles, and require more expertise to synthesize, particularly if making non-spherical particles [10,35]. Gold nanoparticles (GNP, which are particularly relevant to this work) are generally considered to be non-toxic when the diameter is larger than 5 nm [7,36,37], but the coatings required to stabilize the GNPs are generally not safe for biological use [38].

The second family of nanoparticle materials are semiconductor nanoparticles. These are less common than metallic or organic nanoparticles and are not utilized in this work. However, they will be briefly discussed, as materials can sometimes exhibit semiconductor-like properties during the photothermal process. Like metallic nanoparticles, semiconductor nanoparticles must be excited at specific energies, now corresponding to the band gap of the material instead of a surface plasmon resonance. When light illuminates a nanoparticle, photons matching the band gap are absorbed by the valence band electrons. The electrons jump to the conduction band, creating an electron-hole pair. Electrons may return to equilibrium by emitting a photon or through non-radiative processes such as Shockley-Read-Hall and Auger recombination [6]. This recombination is shaped by the defects present in the semiconductor, as the defects encourage heat release over a radiative recombination [18,39].

The final material family broadly includes carbon-based nanoparticles. Carbon materials are generally inexpensive relative to metallic nanoparticles and can be generated as byproducts of other manufacturing processes, making them a compelling choice for any potential applications. Photothermal heating of carbon-based and organic materials occurs through the loosely held π electrons that can be excited by a broad range of wavelengths. As π electrons are excited into $\pi*$

states, internal energy conversions occur between the closely packed energy levels. Excess energy is expelled through bond vibrations and rotations, which in turn results in heat. The broad absorption of carbon may be preferred over the comparatively narrow absorption of metallic nanoparticles for certain applications, such as when using broad light sources like the Sun.

This work explores two carbon-based materials. The first is carbon nanotubes (CNTs), which are, most simply, rolled sheets of graphene. CNTs can have a single wall of graphene (single-walled CNTs, or SWCNTs) or multiple concentric layers (multi-walled CNTs, or MWCNTs). As with other nanoparticles, the structure of the CNTs can be tailored to the specific needs of the situation, as increasing layers of graphene increases the strength and ease of production of the nanotubes at the cost of flexibility and conductivity. CNTs exhibit a broad absorption and subsequently exhibit photothermal heating from a range of wavelengths [40,41]. The structure of the tube contributes to the absorption process, as while some light will be absorbed on the outside surface, light can also enter the hollow tube, bouncing along the tube until it is absorbed and thus increasing the overall absorption and capability for photothermal heating in multi-walled nanotubes [42]. The photothermal conversion efficiencies of CNTs have been reported around 80% [41–44].

Although photothermal heating of CNTs has been studied in biological therapies [45], CNTs are considered to be highly toxic and have been shown to damage the lungs, the genetic material in cells, the liver, and the kidneys [46]. Thus, CNTs are more often used as photothermal heaters in materials, such as in water purification techniques [42,44,47–49] and in polymer composites. The latter will be particularly explored in Chapter 3, as conductive CNTs added to an insulating polymer matrix produces an electrically conductive composite with the mechanical properties of polymers. Indeed, CNT-polymer composites have been studied as flexible

electronics and textiles [50], as mechanical stress release in batteries [51], as gas sensors [52,53], and as strain sensors [54–56].

The second carbon-based nanoparticles featured in this work are melanin nanoparticles (MNP). Melanin nanoparticles are a broad family of biopolymers often found in nature [57,58], from dark skin or hair of humans to ink from squids or dark feathers on birds. While melanin naturally forms nanoparticles and can thus be harvested from natural sources (such as from sepia ink, hair, or pigmented cells [59]), it can also be synthesized through polymerization, such as from dopamine, as used in this work [60,61] or L-dopa [59]. When on the surface of organisms, melanin is considered primarily a means of blocking damaging ultraviolet (UV) light. However, melanin is also a free radical scavenger, and thus functions as an antioxidant, antimicrobial agent, and metal ion reservoir [58,62–64]. The ease and relatively low cost of MNP synthesis [60,61], the natural presence of melanin in nature, and the broad absorption profile [65–67] makes MNP a promising choice for a photothermal heater [57,68] in both biological and material settings.

As such, MNPs have been studied extensively in photothermal therapies, with both near-infrared light [69–71] (which is able to pass through the skin) and UV light [72,73]. The photothermal conversion is suggested to occur via the release of energy through phonons, aligning with the third mechanism of PT conversion common in carbon-based materials. The broad absorption of MNP allows excited electrons to quickly decay into a variety of nearby energy states [74], releasing energy as molecular vibrations, which manifests as heat within the nanoparticle. Because polymeric materials have a relatively low thermal conductivity, and MNP are considered a polymer, there is a buildup of thermal energy, increasing the photothermal conversion efficiency [67], although it has been generally reported to be around 15% to 30% [66,67,70].

1.3 Photothermal Applications

Under certain circumstances [75], this photothermal heating, or the conversion of light into heat, creates intense heat local to the particle and cool temperatures further away (Figure 2) [76,77]. This temperature gradient keeps the bulk temperature relatively low, particularly in comparison to bulk heating, where the temperature is uniformly raised throughout a sample. As the heat comes from exposure to light, photothermal heating allows for external control of internal heat through the presence or removal of light. Photothermal conversion can be tuned by altering the size, shape, or material of the nanoparticles, making this process useful in a broad range of applications. For example, local heat can be selectively applied to certain objects in a system: by intentionally functionalizing nanoparticles to change how the nanoparticle interacts with the surrounding environment [78,79], researchers have created nanoparticles that bind with tumors in the body [80] or perform other targeted heating [37]. When the nanoparticles are illuminated with light (typically using 808 nm light that can pass through the skin), they begin to heat their

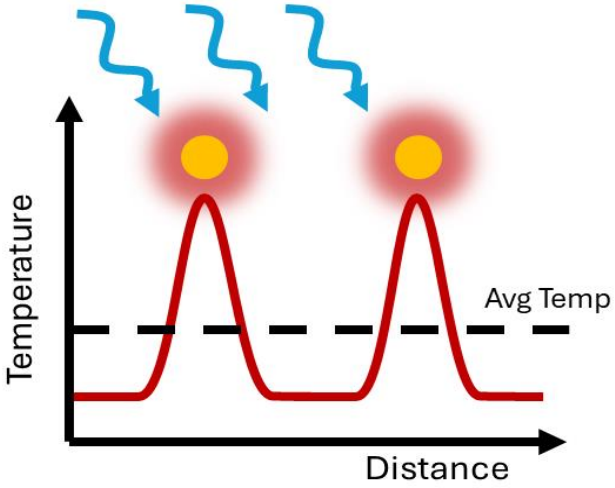

Figure 2: Sketch of photothermal particles (gold circles surrounded by a red gradient to represent heat) interacting with light (blue squiggles). A general temperature profile from the photothermal heating is shown with a red line.

surrounding area, which is primarily the tumor they have bonded to, while leaving the rest of the cells untouched. Photothermal therapy is a promising technique for cancer treatment [81], although there are concerns about nanoparticle biocompatibility [72,82,83] and thus an interest in exploring alternative photothermal heaters beyond the commonly studied metallic nanoparticles.

Photothermal heating has broad applications in non-biological materials as well. With light as the remote control switch for heat, there are possibilities for modifying materials through internal heat. This has been shown in the form of simple actuators using carbon as a photothermal heater that change shape within seconds of being illuminated [84,85]. Similarly, photothermally heated nanoparticles have been shown as nanomotors and nanomachines, allowing for simple motion controlled with the presence of light [86,87]. Furthermore, the internal heat from embedding nanoparticles within materials can selectively cure epoxy [88] or act as a catalyst for other reactions [89,90], thus making photothermal heating a driver of controlled chemical reactions by supplying localized energy only. This local, confined heating and subsequent potential degradation of polymers creates unique pathways down previously established chemical conversions [91,92]. The heat may also provide energy to state changes, as seen by the large interest in using photothermal materials for water vaporization and water purification [49,93–99].

This research is motivated by the unique material processing available from internal, selective heating. In this thesis, we will cover three systems using the photothermal heating of nanoparticles to investigate both (1) the ways that photothermal heating can be utilized to enhance polymer applications and (2) the mechanisms of photothermal heating, particularly for non-metallic nanoparticles. Three independent systems will be considered. To begin, Chapter 2 details how a carbon nanotube filler in a polymer system can be used to create electrically conductive composites. Photothermal heating was then used to improve the electrical contact between the

nanotubes. Chapter 3 will investigate the water loss from hydrogels under both conventional and photothermal heating. The photothermal heating was done with both metallic and melanin nanoparticles in order to compare the photothermal heating of MNPs under visible light with the more commonly used gold nanoparticles. Finally, Chapter 4 will continue to study MNPs as a photothermal heater in polymer by observing the degradation of MNPs and a surrounding polymer. Chapter 5 will discuss potential uses of the systems described and future directions.

Chapter 2: Photothermal heating to improve particle-particle contacts and electrical conductivity in MWCNT: polymethyl methacrylate composites

2.1: Conductive Composites and Carbon Nanotubes

The properties of any composite rely on the matrix, the filler, and the interface between them, which also impacts dispersion. Electrically-conductive polymer nanocomposites (conductive nanoparticles embedded in an insulating matrix) are an interesting case where the desired outcome (increased electrical conductivity) is dominantly influenced by interface conditions [100–102]. High aspect ratio particles, such as carbon nanotubes [100], can achieve sample-spanning conductive networks at low loading, because they have a large effective volume (the region spanned as the particle is rotated over 4π steradians about its center), making overlap to form a many-particle, current-carrying path across the composite more statistically probable [103]. However, these fillers also have strong particle-particle interactions, which lead to side-by-side nanotube aggregation, reducing the beneficial aspect ratio and requiring higher loading to achieve conductivity. Thus, a surfactant is often used to increase particle-matrix compatibility and ensure dispersion (Figure 3a), as surfactants commonly consist of a hydrophilic

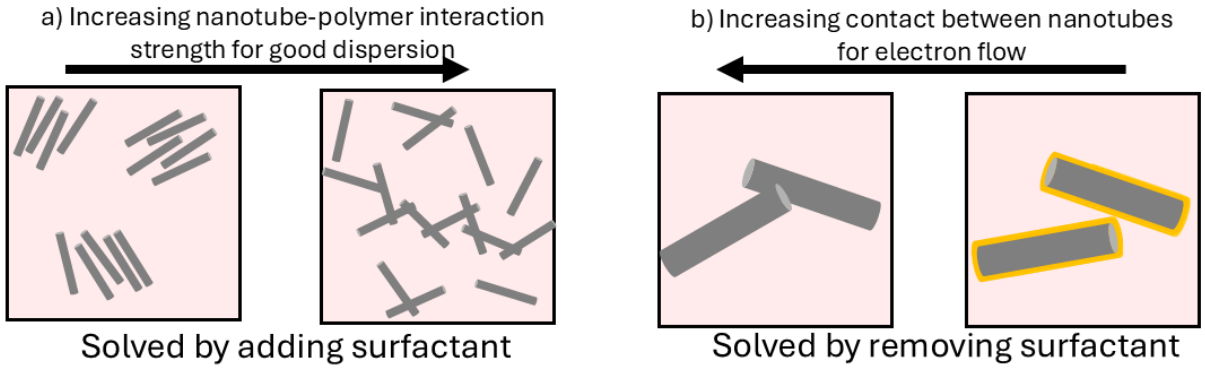

Figure 3: Cartoon of the goals of CNT:polymer composites. a) depicts the desire for a dispersed network, which can be solved by adding a surfactant. However, b) displays the desire for good nanotube contact, which is necessarily reduced with the addition of surfactant.

head and hydrophobic tail that are able to bind with both the carbon nanotube and a solvent. But in the final composite, the strengthened particle-matrix interactions have a deleterious effect: insulating polymer or surfactant residing between particles dramatically decreases resultant conductivity [101] (Figure 3b).

In other words, the goal of conducting particle-insulating matrix composites is that conducting particles "aggregate" beneficially, such that there is end-to-end overlap of the particles without large clumping that prevents the particles from spanning the composite [104]. In theory, this will occur at a critical volume fraction (the percolation threshold) where there are just enough particles to create the network without an excess that drives agglomeration. However, due to the strong particle-particle interactions, network formation cannot take place unless detrimental aggregation (side-to-side stacking) is mitigated. Available strategies for dispersion (such as the addition of a surfactant) also block beneficial particle-particle overlap, where the surfactant reduces the electrical connection between particles. This suggests that there are many particle-polymer-particle junctions within the network that could be improved to improve the electrical conductivity.

Overall, strong particle-matrix interactions are useful during fabrication but unhelpful after the conductive particle network has formed. Recent interventions to address this persistent challenge have focused on manipulating the particle-matrix interaction with time. For instance, pre-assembly of the conductive network in a solvent system and then backfilling with polymer [105–107] utilizes solvent as volatile quasi-matrix, which can be removed upon network formation after aiding dispersion, enabling expulsion from junctions and allowing particle-particle contacts to collapse. Different "matrices" are used at different times. However, in these cases when the true matrix polymer is introduced, difficulty in fully wetting and filling creates new problems,

including lack of the usually beneficial strong contact between the overall network and matrix, leading to poor composite stability. Other strategies to manipulate aggregation over time include particle dispersion in a low viscosity environment with application of shear force after viscosity increases during the solidification [108,109] or crosslinking process [110,111], or manipulating pre-dispersed particle with shear in high viscosity melt [109]. Both approaches require relatively complex, material-specific processing with the goal of entangling tubes in a condition without suitable mobility for side-to-side aggregation.

In this work, an alternative paradigm is explored with polymer composites containing multi-walled carbon nanotubes (MWCNT) where particle and matrix mobility (the ability to aggregate) is different at different times, to optimize for the different goals of a sample at various times in its lifecycle. Using a conventional approach, the particle is dispersed in a low viscosity matrix solution and the extended network forms during solidification: the system is homogeneous with solvated polymer and surfactant/matrix-coated particles mixing freely and then slowing together as solvent is removed. But after solidification, photothermal heating (absorption of light by the particle which is then converted into heat) [5,6,12,24,76,77,81,88,91] is used to pass energy to each carbon nanotube [43,98,112,113] and create heterogeneous local warming (position-dependent increase in mobility) within and around the percolative network, enabling particle and matrix reorganization to improve particle-particle contacts without sufficient mobility that side-to-side aggregation or network damage occurs. Steady-state, elevated local temperatures and a temperature gradient (different steady state temperatures at different locations) from photothermal heating of nanoparticles have been previously reported in solid polymer nanocomposite systems [5,6,76,77,91,114–118]. The region between two nearby particles is expected to have the highest temperature, with that surrounding each particle the next highest [91], and significantly

cooler temperatures in composite regions far from any particle. This particular pattern of heating may enable the interstitial polymer to migrate from junctions and nanotubes to reorient to increase contact, while preventing larger scale mobility that would lead to deleterious particle aggregation.

Applications for electrically-conductive polymer composites utilize the processability, relative light weight, low cost, lack of corrosion, and tunable mechanical properties (from flexible to rigid) of the insulating matrix polymer. Improving energy storage (battery/supercapacitors) [51] and decreasing mass in transportation applications [119] are particular, environmentally-focused targets and both carbonaceous fillers and matrix polymer could ultimately be sourced from waste [117]. This chapter focuses on the moderate conductivity range [100], useful here because the conductivity depends strongly on particle-particle junctions and often targeted for strain and gas sensing applications [54], as interparticle spacing is impacted as the material is stretched or compressed [53,120–125]. A particular application for MWCNT-polymethylmethacrylate (PMMA) composites (as will be utilized in this work) is strain sensing in highways [55,56,126].

Utilizing this scheme and sampling a wide range of initial conductivities and nanotube loading, a proportional increase in conductivity after photothermal heating treatment is observed. This proportional increase is a function of the light intensity applied, and multiple controls are utilized to show a lack of correlation with the global sample background temperature (far from any MWCNT) during treatment. This indicates (1) that the extended MWCNT network is mostly unchanged (e.g., overt side-to-side aggregation is avoided) and (2) that a heterogeneous temperature distribution, with a local temperature near the nanoparticles correlated to light intensity, is present and driving local nanotube mobility. Utilizing a simple heat transport model, we show that when the local temperature in the vicinity of the MWCNT network increases to the polymer glass transition temperature, conductivity increases and grows as this temperature rises.

Local temperature is manipulated by altering laser intensity and the composite surroundings to produce the same local temperature in several different ways. These experiments show that local temperature is the key factor in the increase in electrical conductivity.

2.2 Material and Methods

2.2.1 Materials and Sample Preparation

Multi-walled carbon nanotubes (MWCNTs, outer diameter 15±5 nm, length 5-20 μm, NanoLab, aspect ratio 1500), poly(methyl methacrylate) (PMMA, MW 540,000 g mol^{-1}, Scientific Polymer Products Inc., listed T_g 105 °C), acetone, N, N-dimethylformamide (DMF), and Triton X-100 (all from Sigma Aldrich) were used as received. Triton X-100 was chosen due to its prevalence in research working with CNTs as one of the more effective surfactants available [127–129]. Dynamic scanning calorimetry (Mettler Toledo DSC 1, measured by cooling at 10 K/min from 230 °C) measured a PMMA Tg within the composite of 115 °C. Silver epoxy (EPO-TEK EJ2189-LV, Epoxy Technology) and silver wire (38 AWG, California Fine Wire Company) were utilized to make electrical contacts.

A 20 weight-percent (wt%) PMMA:DMF solution mixed (VWR 325 hotplate/stirrer, approximately 160 rotations per minute) at room temperature overnight in a sealed container until complete dissolution. Separately, equal masses of MWCNTs and Triton-X were added to DMF in amounts depending upon the intended final MWCNT:PMMA weight percent (wt%) and MWCNT were dispersed (Misonix Wand Sonicator 3000, 20kHz one second pulses interspersed with equal rest times (duty cycle of 1) for a total of 10 minutes (5 minutes active)). The suspension was stable and resulted in samples with similar conductivity for up to 55 days (Figure 4).

The casting solution contained volume V of PMMA/DMF solution needed to create the appropriate sample thickness after solvent evaporation, to which a V/2 volume of the MWCNT/Triton-X/DMF solution and V/2 volume of acetone were added, and immediately hand-stirred until the solution was visually homogenous (approximately 60 seconds). An angle-tip cut pipette (FisherBrand Elite Adjustable Volume Pipette, 100 to 1000 μL) was used to measure and transfer solution (e.g., 350 μL for a 0.06 mm thick sample) onto the center of a UV-ozone cleaned (BioForce Nanoscience UV/Ozone ProCleaner; 15 minutes exposure followed by rinsing with DI water and drying in 65 °C oven) borosilicate glass coverslip (VWR 48366-227, 2.2 cm × 2.2 cm area, thickness 0.16 mm to 0.19 mm), which was immediately placed in a 65 °C oven (VWR 1300U) to enhance solvent removal. Solidified samples were removed from the oven after 30

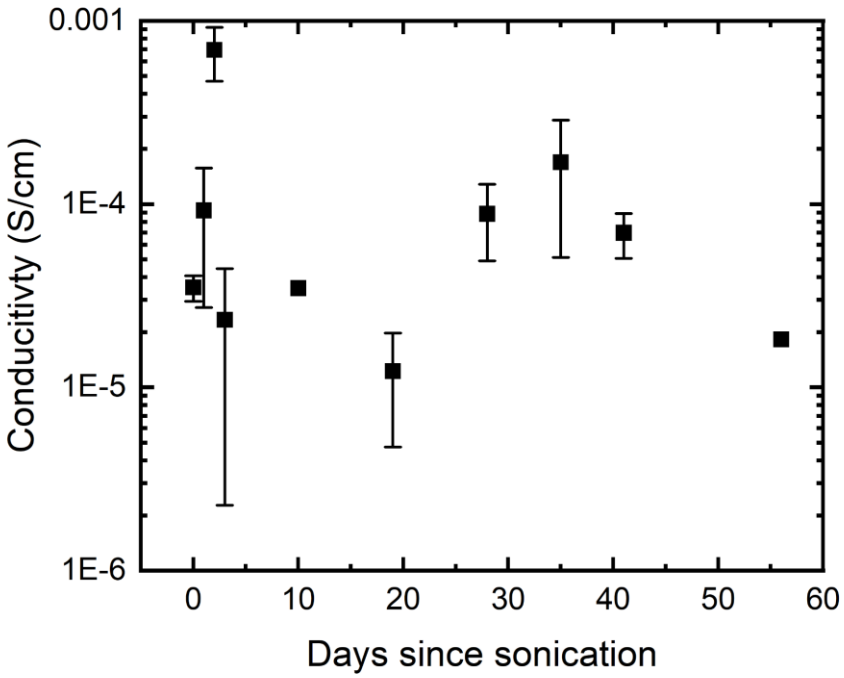

Figure 4: 0.125 wt% MWCNT composite conductivity versus the age of the sonicated MWCNT/Triton-X/DMF solution used to make the samples. Average conductivity (over all samples) was $2.5\times10^{-4} \pm 3.0 \times10^{-4}$ S/cm. Sample thickness was approximately 0.06 mm.

minutes and readily detached from the coverslip after cooling. Samples had 0.0625, 0.125, 0.250, or 0.5 wt% MWCNT:PMMA and ranged in thickness from 0.025 mm to 0.14 mm.

To enable electrical measurements, silver epoxy contacts were painted in two parallel rectangular strips (6 mm x 20 mm) on opposite sides of the top sample surface with a silver wire (subsequently connected to the measurement apparatus) embedded in each contact. Epoxy was cured in a 100 °C oven for 45 minutes. Header pins were attached to the ends of the exposed wires for ease of multiple measurements.

2.2.2 Sample Characterization

Electrical conductivity was determined (Keithley Model 6430 Sub-Femtoamp Remote SourceMeter) from voltage applied – current measured, two-probe measurements, controlled by a specialized LabVIEW program. A standard sweep was 1 V increments (5 second rest time after voltage applied) from zero to 10 V, 10 V to -10 V and -10 V to zero. The slope of the resulting voltage-current plot corresponds to the inverse of sample resistance, which is then used to calculate conductivity σ according to: $\sigma = \frac{L}{RA}$, where L is the separation between the epoxy contacts (as measured with a digital caliper), R the resistance, and A the cross-sectional area calculated from the drop cast volume and confirmed by thickness measurement (The Starrett Co. No. 1230 outside micrometer).

Optical characterization was performed using absorption spectroscopy (Agilent Technologies Cary 60 UV-Visible Spectrometer) and Fourier transform infrared spectroscopy (Agilent Technologies Cary 630 Fourier Transform Infrared (FTIR) Spectrometer) Additionally, transmission electron microscopy (TEM) (Hitachi BioTEM HT7800) was used to image MWCNTs within micro-tomed (Leica Ultracut UCT) approximately 90 nm thick) sample sections

on a sub-visible wavelength scale. For each sample, the diameter of over 600 nanotubes across at least six images was measured by hand in ImageJ.

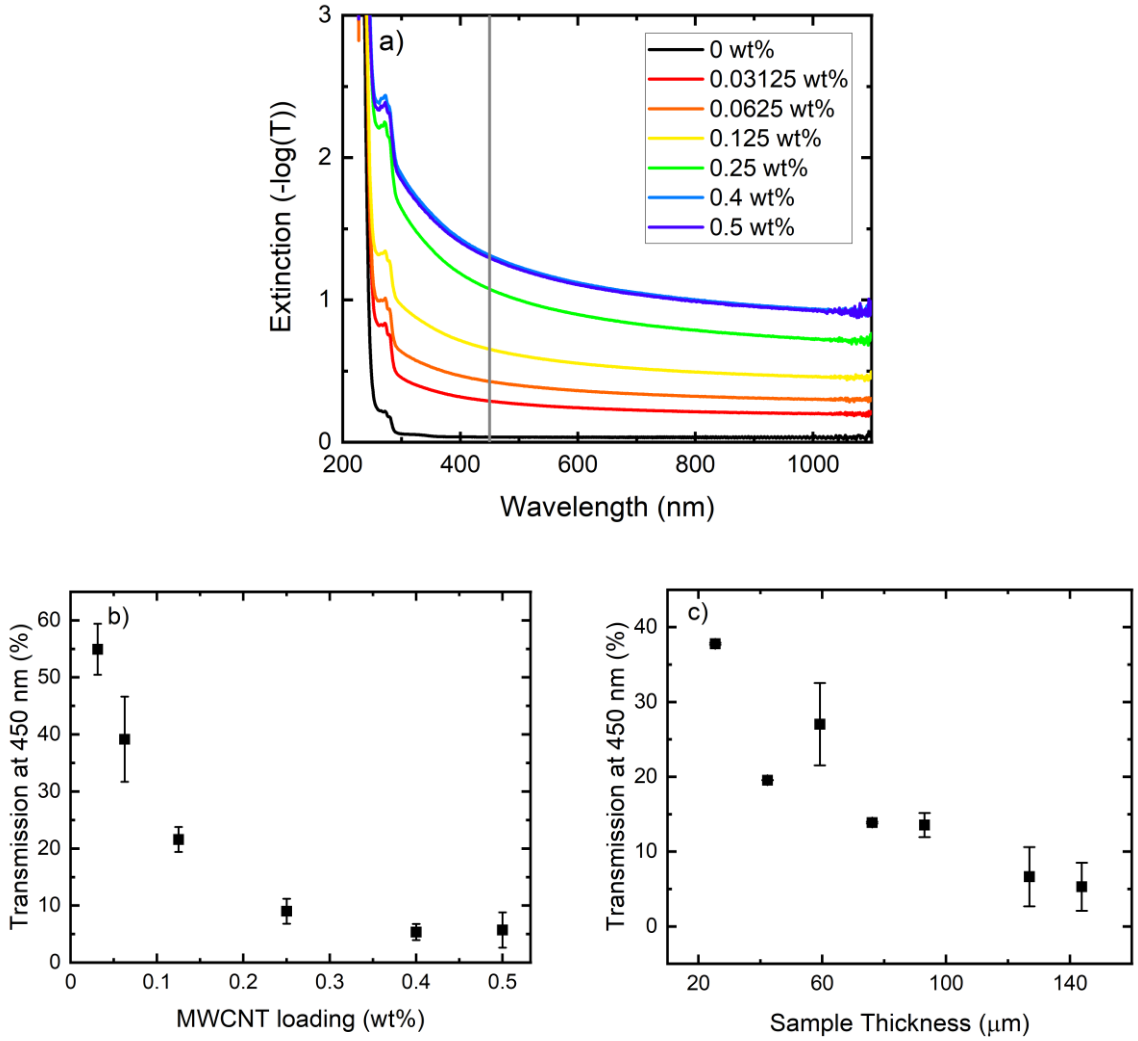

Figure 5: a) Optical extinction of MWCNT:PMMA composites. Characteristic broad absorption from MWCNTs increases with increasing nanotube concentration with minimal contribution from PMMA in the visible range. The vertical line represents the illumination of the 450 nm source for photothermal heating. b) Transmission through the sample at 450 nm for varying MWCNT loading. c) Transmission through 0.125 wt% MWCNT:PMMA samples at 450 nm for different thicknesses of the sample.

2.2.3 Photothermal Treatment

Extinction spectra of MWCNT:PMMA composites (Figure 5a) confirmed that the MWCNT absorb across the visible wavelength range. Photothermal treatment was performed with a 450 nm diode laser (Lasertree 4.5 W) with a variable user-selected (via custom-built input power control) average intensity in the range 0-0.6 W/cm^2. The beam was expanded to uniformly illuminate the entire sample, placed with the epoxy-side down to avoid shadowing due to the electrical contacts and positioned on a glass slide secured 3 mm above the table surface for thermal isolation. A snorkel (18 cm × 18 cm input area) located 23 cm from surface of the sample provided ventilation. Sample temperature was determined by a K-type thermocouple (RisePro Thermocouple) firmly pressed to the nanocomposite surface at consistent time intervals; under continuous photothermal heating, samples typically reached maximum steady state temperature after approximately two minutes. A typical plot of conductivity increase versus treatment time (Figure 6, 0.44 W/cm^2 intensity) shows that ca. 90% of the conductivity increase occurs within the first hour, selected as the standard treatment time for this work.

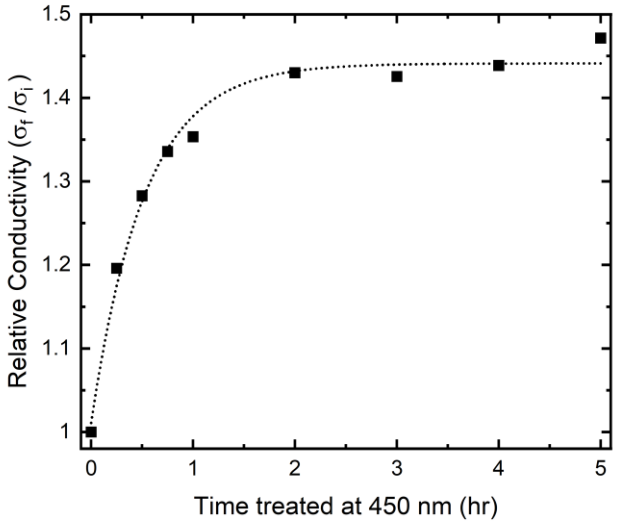

Figure 6: 0.125 wt% MWCNT composite conductivity versus photothermal heating time. The fit line has a time constant of 0.52 hours

2.2.4 Conventional Heating

Conventional heating in an oven or via hotplate was utilized as a control or in conjunction with photothermal heating. For conventional heating, samples were placed in a custom-built oven at a controlled temperature (100-110 °C, Watlow SD Temperature Controller) for one hour. To increase the background temperature during photothermal treatment, samples were placed on glass slides on a hotplate (VWR 120V Hotplate Pro) held at the desired temperature with all other photothermal treatment procedures maintained as previously described. The two forms of conventional heating showed the same results.

2.3 Results and Discussion

2.3.1. Basic Composite Properties

Composites were fabricated using standard laboratory-scale procedures and had expected properties. Figure 7a contains typical current-voltage scans for 0.125 and 0.250 wt% MWCNT:PMMA loading. A linear response is observed. At 0.0625 wt% MWCNT:PMMA (data not shown) some curvature and hysteresis were noted, indicating proximity to the critical volume fraction. Plotting average conductivity σ versus MWCNT loading (Figure 7b) shows the expected dramatic increase around the critical value followed by slower growth. Power law scaling (Figure 7b inset), $\sigma \sim (\rho - \rho_{crit})^{\beta}$ [130] (where σ is the conductivity and ρ is the MWCNT loading), results in critical value of 4 x 10^{-4} volume fraction (which is 0.057 wt%) with β = 2.1, within the range of expected exponents for a three-dimensional sample [131]. The observed critical value is consistent with the classic heuristic of nanotube inverse aspect ratio [132,133], which results in a range of 5 x 10^{-4} - 4 x 10^{-3} using nanotube dimensions and errors from the manufacturer, which are consistent with TEM measurements (Section 2.3.4).

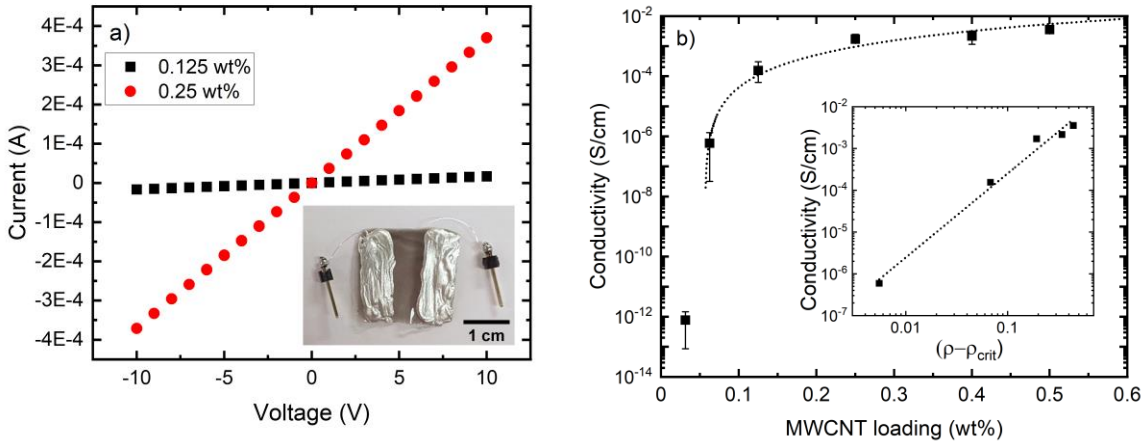

Figure 7: a) Characteristic current versus voltage scans for 0.125 wt% (black squares) and 0.250 wt% (red circles) MWCNT:PMMA composites. Inset: Photo of characteristic 0.125 wt% sample. b) Conductivity versus volume fraction (black squares). Percolation model (dotted line). Inset: power law scaling used to determine crit and β (see text).

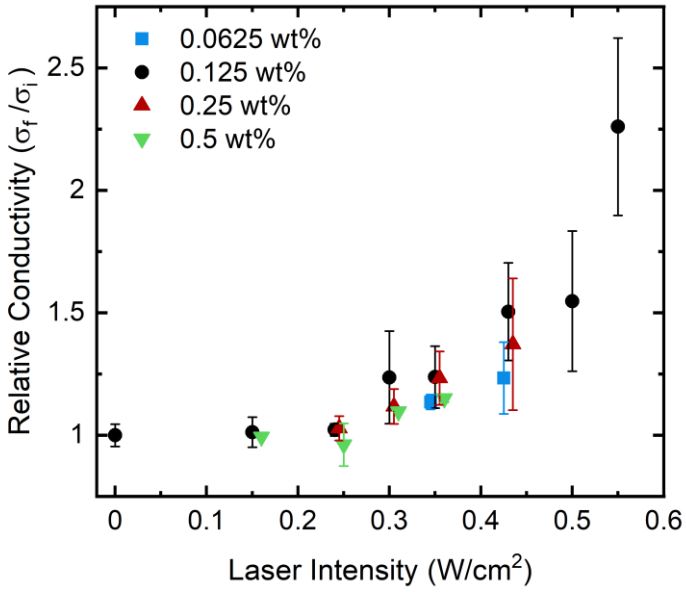

Figure 8: Relative conductivity (i.e., the ratio of final to initial conductivity) for different MWCNT concentrations and laser intensity. Points are slightly offset in laser intensity to aid in viewing. The data at each concentration is limited to a maximum laser intensity where the global temperature reached ~110 °C (above the PMMA T_g) and bulk sample deformation occurred. Cases where the sample deformed (e.g., intensities greater than 0.55 W/cm^2 for 0.125 wt% MWCNT: PMMA or 0.34 W/cm^2 for 0.5 wt% MWCNT:PMMA) are not included and were associated with lower relative conductivity gain, as discussed in greater detail below. The largest conductivity increase occurs for moderate (0.125-0.25 wt%) loading exposed to the highest laser intensity possible without bulk deformation. Sample measurement consistency is visible in the 0 W/cm^2 point, where an untreated sample was repeatedly measured over multiple days.

2.3.2. Increase in Conductivity due to Photothermal Heating

Photothermal treatment increased electrical conductivity, with applied light intensity being the most important experimental factor. MWCNTs absorb across the visible spectra (Figure 5). Exposure of 0.125 wt% MWCNT:PMMA composites to 450 nm light at intensities greater than 0.25 W/cm^2 resulted in a consistent increase in conductivity, by a proportional factor dependent on intensity (Figure 8, black circles). Lower light intensities ($\leq$ 0.25 W/cm^2) had no observable effect. Specifically, the relative conductivity (σ) increase ($\sigma_{final}/\sigma_{initial}$) was 1.01 $\pm$ 0.06 at 0.15 W/cm^2 (no change) compared to 2.5 $\pm$ 0.58 at 0.55 W/cm^2 (maximum change). For any given MWCNT loading, initial sample conductivity could range by up to two orders of magnitude (Figure 4), particularly through manipulating solidification time. Nevertheless, photothermal heating at a given light intensity consistently resulted in a proportional change (e.g.,1.3x the original value).

In photothermal modalities, local temperatures are controlled by laser intensity and the interface between the particle and the rest of the composite. Elevated local temperatures from photothermal heating of nanoparticles have been previously reported in solid polymer nanocomposite systems [76,77,91,114–116]. Global temperature (or the background temperature far from any particles) is also influenced by laser intensity but additionally depends on particle concentration and environment (e.g., heat loss from the sample surfaces) thus enabling one to distinguish the two mechanistic effects.

The observation of proportional conductivity increase, regardless of initial conductivity, is consistent with photothermal treatment enabling modification of the existing percolating network to primarily enhance particle-particle contacts while leaving the extended MWCNT supercluster intact. The results indicate that under photothermal heating, the matrix around and between

MWCNT experiences local temperature rise, enabling improved nanotube-nanotube connections and thus increased composite electrical conductivity. If the effective resistance at each contact decreases while the network remains largely unchanged, then the final and initial conductivities should be proportional, with the scaling factor reflecting the average improvement in each particle-particle contact.

Global temperature increase due to photothermal heating was not the dominant factor causing observed change in conductivity. Figure 9 displays observed global temperature as a function of intensity, which has a roughly linear dependence from room temperature up to the PMMA matrix Tg. Higher particle concentration results in additional MWNCT absorbers per volume and thus raises global temperature at any given intensity (Figure 9, e.g., 0.35 W/cm^2 data.) but as seen in Figure 8, this does not increase the relative conductivity change. In addition, uniform

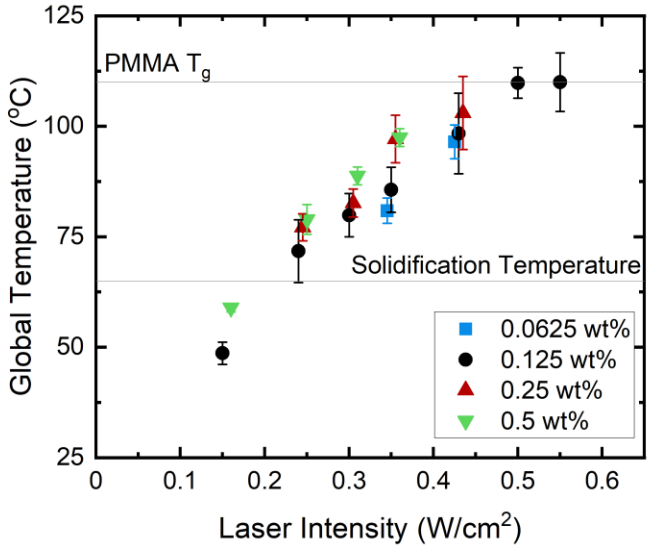

Figure 9: Measured global (bulk) temperature at a given laser intensity. All samples experience solidification in an oven at 65 °C during fabrication. Below T_g, temperature has a roughly linear dependence on laser intensity, with a slope that increases with MWCNT concentration

(where local temperature equals global temperature), conventional heating cannot reproduce the photothermal results. For light intensities above 0.3 W/cm^2 where conductivity changes were observed (see Figure 8), the global temperature varies from 75 to 100 °C. Exposure to these temperatures using conventional means with no light present results in no conductivity increase ($\sigma_f/\sigma_i \sim 1$) as summarized in the 0 W/cm^2 control point in Figure 10.

By creating the same global temperature from different combinations of light intensity and particle concentration, the two effects (global temperature and light intensity) can be further distinguished. Figure 10 plots the data from Figure 8 and Figure 9 in a different way: relative conductivity versus intensity, grouped by global sample temperature (indicated by color) for global temperatures less than the PMMA T_g. For non-zero light intensities, each temperature group includes cases with different concentrations and different intensities - their commonality is they

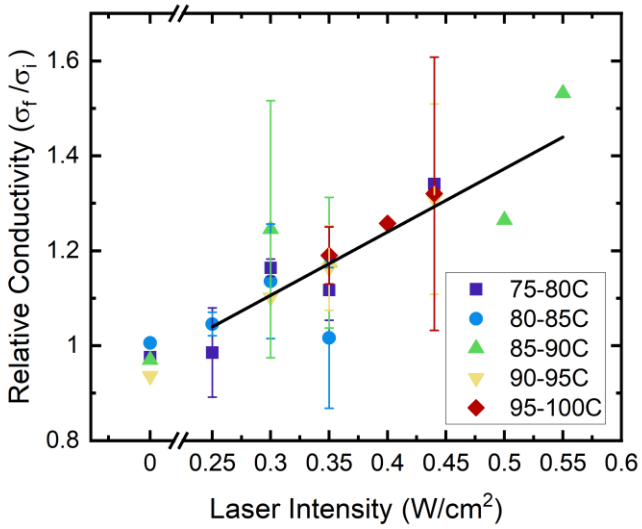

Figure 10: Relative conductivity increase versus laser intensity, plotted by global temperature group. Each temperature range contains samples of varying MWCNT concentrations and laser intensities that were measured to have the same bulk temperature during photothermal treatment. The overlapping plots indicate that conductivity change is not determined by global temperature during treatment. A linear fit from 0.25 W/cm^2 – 0.55 W/cm^2 is applied to all data (solid black line).

result in the same global temperature. If global temperature were a significant factor, different temperatures should be offset with, for instance, higher temperatures showing larger relative change. Instead, the data for 75 °C to 100 °C, are superimposed and the highest temperature range (95-100 °C) displays the same relative conductivity change as a function of intensity as the lowest temperature data (75-80 °C). Examining each intensity, there is no observed trend with temperature. For instance, exposure to 0.43 W/cm^2 results in temperatures that range (depending on MWCNT concentration) from 75 to 100 °C (Figure 9); however, all of these cases have the same relative conductivity increase of approximately 1.3 (Figure 8 and Figure 10). This indicates that the change is driven by the intensity (related to the local heating) rather than the global temperature.

Global background temperatures above 105 °C, which is near the PMMA glass transition temperature, resulted in macroscopic changes to the sample, and thus set a limit on the controlled range of treatment, given that the goal is to manipulate interior morphology without altering the bulk sample size and shape. Thus, for higher concentrations, the maximum useful intensity is restricted as reflected in data plotted in Figure 8. Samples that experienced deformation showed lower average conductivity improvement than counterparts treated at the same laser intensity, even when accounting for the changed geometry. For example, at 0.5 W/cm^2, samples that did not deform had a relative conductivity of 1.55 ± 0.29, while those that reached global temperatures resulting in shape change had a relative conductivity of 1.15 ± 0.11. Combined with results above, these observations indicate that elevated global temperature during photothermal treatment has either a neutral (providing it remains below T_g) or detrimental effect on conductivity The effect of global temperature above T_g is discussed further in Section 2.3.4.

2.3.3. Effect of particle concentration

Altering concentration provides additional insights into the mechanisms that lead to increased conductivity upon photothermal treatment. Higher concentration samples (0.25 and 0.5 wt%) have a 10x and 20x, respectively, larger average initial conductivity compared to the 0.125 wt% composites (Figure 7b). Moving down the percolation curve to lower concentrations, 0.0625 wt% composites have two orders of magnitude lower average conductivity (Figure 7b). Considering all loading levels, initial conductivity spans three orders of magnitude. However, the dominant effect of photothermal treatment is a proportional increase in conductivity as shown in Figure 8, largely independent of the initial value. These results support the hypothesis that the primary effect of photothermal treatment is altering the junctions within the particle network, resulting in a proportional increase in conductivity, and that the exact nature of the particle supercluster (branching, connectivity, and particle density, which depend on dispersion and MWCNT concentration) has only a secondary effect, as discussed below.

Beyond global temperature (see Section 2.3.2) at a given intensity, there are three changes with concentration: 1) the nature of the particle network, i.e., the characteristic distance between particles as determined by MWCNT concentration, 2) the uniformity of light illumination throughout the samples due to shadowing (absorption of light by particles closer to the light source), and 3) changes in the temperature gradient pattern due the density of particles within the sample. These are discussed in the next two paragraphs and Section 2.3.4, respectively.

The nature of the percolating network has a secondary effect on the relative conductivity increase with particular loading values showing greater enhancement. The moderate concentration of 0.125 wt% lies just above the dramatic increase in conductivity occurring at the critical volume fraction (Figure 7b), indicating that a robust but relatively unbranched network has formed, and

exhibits the largest change. At higher (0.25 and 0.5 wt%) MWCNT concentration, branching and a more complete network may enable current flow to circumvent high resistance junctions, which could decrease the conductivity impact of improving particle-particle junctions. Conversely, the just-forming network at lower concentration (in the 0.0625 wt% case), may have larger particle-particle junctions and/or more high resistance "pinch points" that cannot be productively altered. These observations match the understanding of gauge factor (change in conductivity with applied strain) sensitivity when similar composites are stretched or compressed to alter particle-particle junctions [54]. Gauge factor is maximized in the region of the percolation transition. Thus, the nature of the network influences conductivity improvement.

Because the photothermal process utilizes light to carry energy into the interior of the composite, which is then collected by the MWCNT and converted to heat, optical transparency (i.e., providing for uniform illumination throughout the entire sample thickness) is an important factor for higher concentration samples. "Shadowing," where the effective illumination in lower (away from light entry) sample regions is reduced, will impact the ability to photothermal heat. The fraction of light fully transversing a 60 μm (the standard thickness used in this work) thick

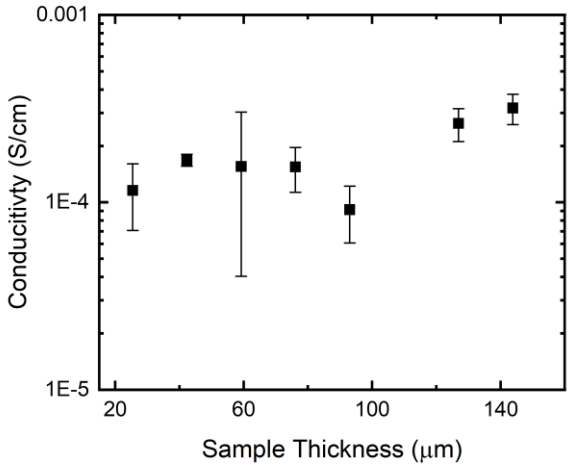

Figure 11: Conductivity for 0.125 wt% samples before treatment with varying thicknesses. Thickness does not significantly impact the starting conductivity of the sample.

sample decreases from 37 to 5% as the concentration increases from 0.0625 wt% to 0.5 wt% (Figure 4b). To deconvolve innate concentration (nature of the network) and illumination effects, 0.125 wt% samples with thickness varying from 25 to 140 μm, (leading to transmittance values from 40 to 3%, Figure 4c) were tested (Figure 12). Initial conductivity was unchanged with thickness (Figure 11). Bulk temperature under photothermal heating (for a fixed intensity of 0.35 wt%) increased with sample thickness, spanning the range of 75 - 95 °C. (Figure 12b). Sample thickness had a non-monotonic effect on relative conductivity (Figure 12a). Samples with thickness on the order of the MWCNT length (15 μm), showed decreased response. This may be due to the inability to localize heat at junctions, as the MWCNTs (which are expected to be 15 um long) are more likely to be in contact with the surface (and air that is cooler than the sample) in these thinner samples than in a thicker sample. The MWCNTs within a percolating path are therefore more likely to conduct energy to the surface of the sample, providing a means of heat transfer away from the junctions. The maximum relative conductivity occurred for samples with

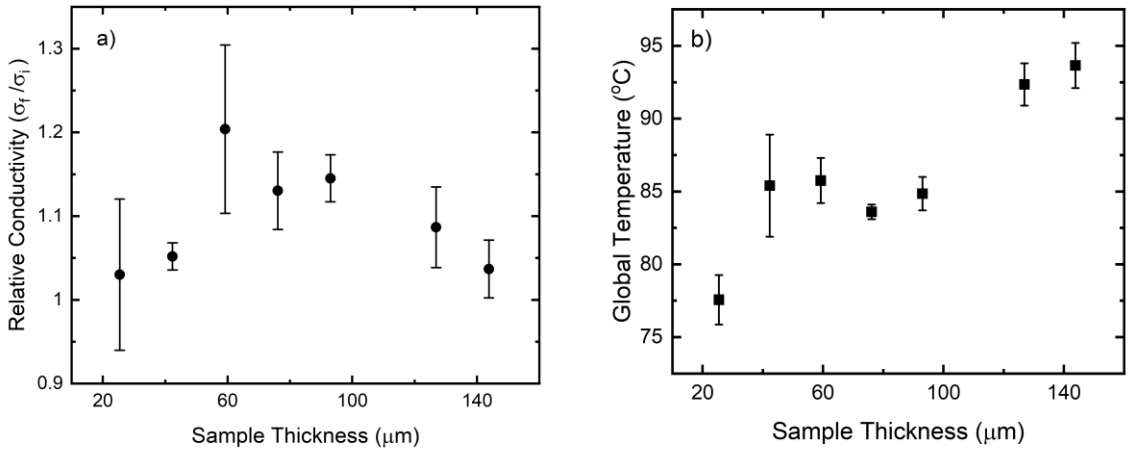

Figure 12: a) Relative conductivity increase and b) global treatment temperature versus thickness for 0.125 wt% MWCNT samples due to photothermal treatment for 1 hour at 0.35 W/cm^2. Thinner samples exhibited lower conductivity increases, likely due to heat transport along MWCNTs in contact with the sample surface. For thicker samples, MWCNTs on the light-entry side may shadow those deeper in the composite, leading to non-uniform photothermal heating and thus a reduced response.

transmittance values around 20%, corresponding to samples with a thickness near the standard 60 μm. For thicker samples, shadowing effects are more likely and the relative conductivity change decreased. For example, a 140 μm thick 0.0125 wt% MWCNT:PMMA sample with transmittance of 5%, comparable to the transmission of a standard 60 μm thick 0.5 wt% composite, had a 10% decrease in relative conductivity change compared to the thinner samples. This could explain the approximately 5-8% decrease in relative conductivity when comparing 0.5 wt% and 0.125 wt% results (with the same thickness) at various intensities the surface.

2.3.4. The role of T_{local}

The photothermal process here utilized produces heat at light-absorbing particles, surrounded by transparent polymer that will not directly absorb the incoming light energy. In many solid polymeric systems, photothermal heating results in a steady state temperature gradient from each particle outward [76,77,91,114–116]. However, there are several complications when utilizing particles that form sample-spanning networks, rather than heating isolated objects. Compared to isolated particles, where all heat must transfer through the polymer matrix to reach the sample's surface, sample-spanning MWCNT pathways enable heat flow to the surface along the particle network without passing through the bulk polymer. The polymer residing in inter-particle junctions within the network will likely experience the highest temperature, with matrix near the sides of each MWCNT (moving outward into the polymer) the second warmest, and temperature decaying to a global background (the lowest temperature in the system) in regions far from any particle.

We constructed a simple model of heat flow with the goals of estimating the local temperature near the sides of the MWCNT, connecting this local temperature to the observed

results, and comparing data from experiments that create different internal temperature patterns (different concentrations, intensities, and surface heat loss conditions). As summarized in Figure 13, energy is captured by the MWCNT network, which warms and forms an extended heated source within the matrix. For cases near the critical volume fraction (the "percolation threshold"), a rough model of this aggregate internal heater is a meandering cylinder of order-of-magnitude length equal to the sample size and a characteristic radius (probably a few times the MWCNT length). One can approximate the smooth decrease in temperature outward from the nanotube network into three steps: a local region within the characteristic radius where the average temperature is high (and called T_{local}), matrix relatively far from the percolating cylinder where the average temperature is T_{global}, and a linear transition between these two regions over a length scale similar to the characteristic radius. Such a construct results in two macroscopic interfaces through

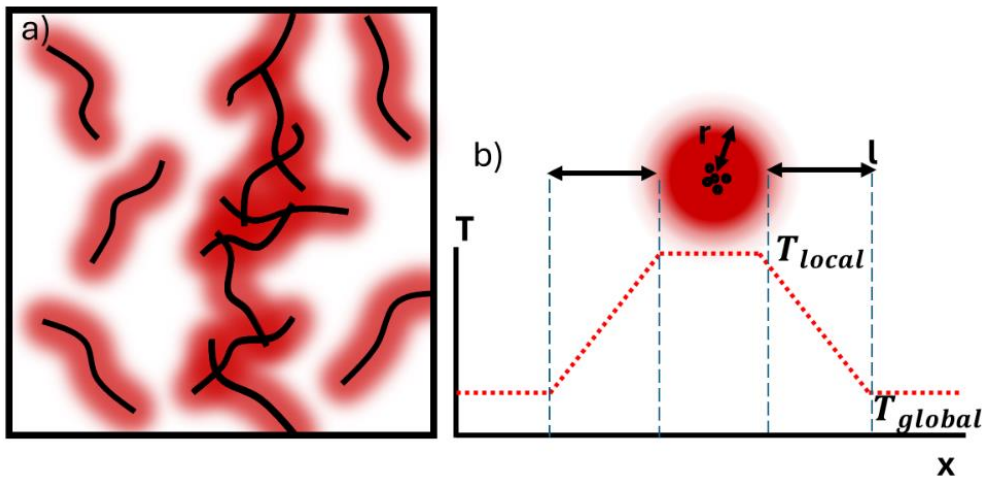

Figure 13: a) Model of the MWCNT network from above showing individual MWNCT (black lines) and one sample-spanning path. The matrix relatively close to the sample spanning pathway (shown in red) is considered heated to T_{local} in this simple model. The meandering tube where $T = T_{local}$ has order of magnitude dimensions with the characteristic radius set to the MWCNT length and characteristic length set to the sample dimension. b) The approximated temperature profile in a cross section showing a linear temperature difference between T_{local} and T_{global}.

which heat flows: conductive heat flow through the matrix in the transition region from T_{local} to T_{global}

$$\frac{dQ}{dt} = \frac{\kappa(2\pi rL)\left(T_{local} - T_{global}\right)}{r} = \kappa(2\pi L)\left(T_{local} - T_{global}\right) \quad (1)$$

and convective heat flow through the composite surface to the surrounding air (with a temperature $T_{external}$)

$$\frac{dQ}{dt} = HA_{sample}\left(T_{global} - T_{external}\right) \quad (2)$$

where κ is the thermal conductivity of the polymer, L is the length of the aggregate internal heater, T is the temperature at a given location, H is the convective heat transfer coefficient, and A_{sample} is the surface area of the bulk sample. In steady state, the heat flow is in balance:

$$\kappa(2\pi L)\left(T_{local} - T_{global}\right) = HA\left(T_{global} - T_{external}\right). \quad (3)$$

This order of magnitude approach enables an estimate of T_{local} based on T_{global} measurements, which can then be correlated with the observed conductivity changes. Utilizing H = 12 $Wm^{-2}K^{-1}$ for natural air convection, the thermal conductivity of PMMA as 0.2 $Wm^{-2}K^{-1}$, $T_{external}$ = 23 °C, and measured T_{global} values for varying laser intensity, the T_{local} for the 0.125 wt% composites ranges from 60 to 150 °C, when heated only with photothermal means in a still air environment. Plotting the relative change in conductivity versus T_{local} (Figure 14, black diamonds) shows conductivity changes begin to occur when T_{local} is around 105 °C (which is the PMMA matrix glass transition temperature) and increases as T_{local} increases. Electrical conductivity continues to improve with higher T_{local} until T_{global} reaches T_g (as discussed in Section 2.3.2, data not shown) and the bulk properties of the sample begin to change.

Overall, this analysis indicates that two conditions must be present to result in conductivity change: light to drive photothermal heating and a $T_{local} > T_g$, the latter of which presumably enables MWCNT rearrangement. Regarding the first condition, as discussed in Section 2.3.2, control experiments where composites are heated conventionally (uniformly) to temperatures near T_g do not result in conductivity increase. Above T_g, composites experience deformation and have a lower conductivity change. The requirement for light is likely related to the need for different temperatures in different parts of the sample - in particular, temperature rise within and near the

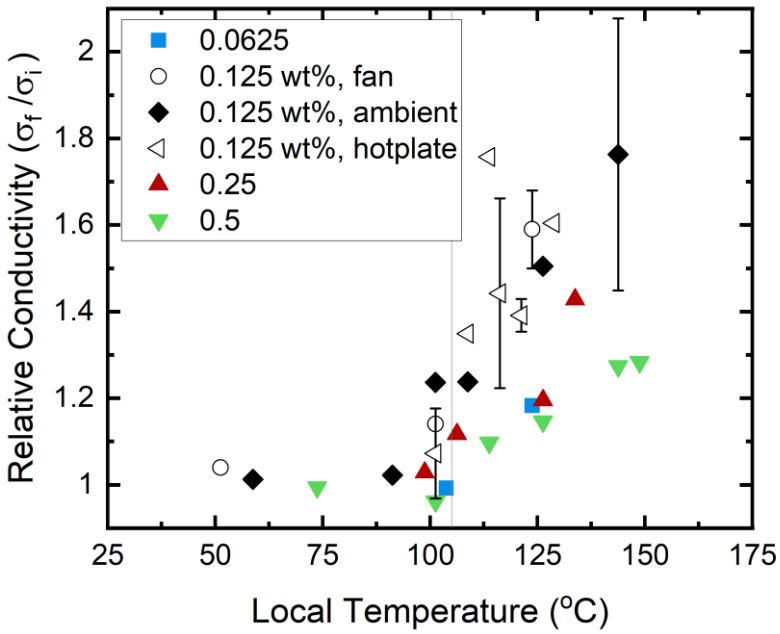

Figure 14: Relative conductivity versus estimated local temperature near the effective internal heater formed by the MWCNT network (from the model described in text) for four different MWCNT concentrations. The PMMA T_g of 105 °C is indicated by a vertical line. For 0.125 wt% samples, three different external conditions (ambient, forced convection with a fan, and elevated temperature represented by black diamonds, open circles, and open left pointing triangles, respectively) were utilized to tune the temperature profile, while keeping MWCNT concentration and light intensity constant. This enabled a clearer delineation of the role of T_{local}. The 0.0625 wt% (blue squares), 0.25 wt% (red upward triangles), and 0.5 wt% (green downward triangles) composites were treated under ambient conditions. Error bars indicate standard deviation of average conductivity change for samples with similar local temperatures.

particle network enables rearrangement without overall bulk heating that may damage the network (e.g., enabling side-by-side aggregation).

The observation that T_{local} plays a crucial role in enabling conductivity increase can be further supported and delineated by manipulating heat loss at the external surface. This creates situations where concentration and intensity are fixed but the internal temperature pattern during treatment is alternated (e.g., pushing T_{local} above or below T_g) and the resultant conductivity change can be observed. Heat loss at the external surface was changed by altering $T_{external}$ (the environmental temperature around the composite) or by changing H (adding a fan to remove heat from the composite surface, forced convection). Using eq. (3) with the appropriate external temperature or H for forced convection (here, 30 $Wm^{-2}K^{-1}$) results in T_{local} estimates represented by empty shapes in Figure 14. Notably, as discussed further below, T_{local} estimates from the simple model again show that conductivity changes begin to occur when T_{local} reaches T_g. Thus, even with changing external conditions, T_{local} controls the conductivity change, such that the highest T_{local} without T_{global} exceeding the T_g results in the largest conductivity increase.

This experimental set represents three different internal temperature profiles within the 0.125 wt% composites. When the only heating source is MWCNT and still air surrounds the composite, the difference between local and global temperatures ranges from 10 to 40 °C and increases approximately linearly with applied intensity. As intensity increases, both temperatures increase but T_{local} increases more rapidly enabling $T_{local} > T_g$ and $T_{global} < T_g$ at sufficiently high intensity. Lower intensity leads to a smaller $T_{local} - T_{global}$ and in ambient conditions, lower intensity (e.g., 0.25 W/cm^2) does not result in $T_{local} > T_g$, thus no conductivity increase is observed. However, conditions with $T_{local} > T_g$ can be created with low intensity light and an elevated, because all temperatures increase with $T_{external}$. The difference between local and global

temperature is still dominantly determined by the intensity, regardless of the external temperature, such that a 0.25 W/cm^2 and 0.35 W/cm^2 treatment results in an average T_{local} - T_{global} of 7.5 °C and 9.8 °C, respectively. However, raising to temperatures ranging from 70 to 95 °C, results in values from 100 to 128 °C (Figure 14, open left pointing triangles) and again an increase in conductivity occurs when is greater than T_g. These samples experience deformation and for higher values, $T_{global} > T_g$, but conductivity increase is observed, indicating that even with relatively low intensity light, the difference between T_{local} and T_{global} is sufficient to improve particle-particle junctions while mitigating side-to-side aggregation and network collapse from a breaking of the percolating pathway through significant nanotube movement. Therefore, one can increase conductivity by either increasing intensity (which directly raises T_{local}) or keeping intensity fixed at a low level and increasing $T_{external}$ to elevate T_{local} above T_g.

Accelerating heat loss from the surface with a fan resulted in lower T_{local} and T_{global} values, and a higher difference between T_{local} and T_{global} for a given intensity compared to ambient or heated conditions. Here, higher light intensities (which in still air conditions would result in $T_{global} > T_g$, sample deformation, and no or a decreased conductivity increase) are needed to bring T_{local} to T_g and thus enable conductivity changes. Intensities of 0.35 - 0.77 W/cm^2 resulted in T_{local} values from 50 to 122 °C (open circles, Figure 14). The same trend that requires $T_{local} > T_g$ is again observed. The collapse of data from these three different temperature profiles indicates that the predominant effect controlling the conductivity increase is the local temperature, however that is achieved.

As discussed in Section 2.3.3, altering the MWNCT concentration will change the nature of the percolating network: 1) providing greater or lesser ease in heat transport through the MWCNT network directly to the surface rather than flowing through the matrix and 2) changing

the surface area and branching of the extended heat source tube (where the average temperature is T_{local}) and thus the geometry associated with eq. (3). In steady state, heat power entering the sample must be balanced by heat power leaving the sample along either the MWCNT network or via the matrix to the composite surface. The relative importance of the two exit pathways can be probed by estimating the total heat power into the system from the light intensity, photothermal conversion efficiency, and number of absorbers and comparing it with heat loss (through the matrix) from the surface (eq (2)). Utilizing measured intensity and absorption values and an estimate of the MWCNT photothermal efficiency of 60% [41–44] for 0.125 wt% and above, the ratio between power in and power exiting through the polymer is 2.2 ± 0.2 with no change as a function of concentration from 0.125 - 0.5 wt%. This indicates that a significant portion of the heat generated in the sample (~70%) travels directly through the MWCNT network to the surface with the remaining ~30% moving through the matrix. The lack of concentration dependence indicates that both processes increase relatively proportionally with increased doping above the critical volume fraction. At higher doping there are a larger number of MWCNT pathways to the surface but these pathways also produce a larger surface area of the T_{local} region to drive heat through the matrix. Composites with only 0.0625 wt% (very near the critical fraction) show a lower ratio (1.81 ± 0.03) which indicates the particles are more isolated, with a smaller fraction of the heat flowing through the MWCNT network. This makes sense given the more fragile and unbranched nature of the particle network just above the percolation threshold.

As discussed in Section 2.3.2, the conductivity increase under the same conditions is smaller for MWCNT concentrations significantly above the critical volume fraction (e.g., at 0.5 wt%). Applying eq. (3) to higher concentration composites without any adjustments to account for the larger surface area and branching results in T_{local} values (Figure 14, colored symbols) that are

upper estimates. These values support the conclusion that temperatures near T_g are needed to result in conductivity increases. The slight shift of the curves to higher T_{local} values likely reflects a more branched and larger surface area region of T_{local}, which we have not included in our model. However, the slope of the curves indicating less gain in conductivity as temperature increases for higher concentration cases is consistent with earlier analysis (Section 2.3.3). The largest rise in relative conductivity as T_{local} increases occurs for 0.125 wt% case, where a robust but relatively unbranched MWCNT network is present. For this situation, utilizing photothermal heating to reduce interparticle junction resistance is particularly fruitful.

2.3.5. Visualization of the Network and Matrix Stability

The goal of photothermal heating in this context is to locally warm regions within the composite so MWCNT can slightly reorient to reduce particle-particle contact resistance. Ideally this occurs without damage to the matrix (via for instance, thermal degradation). T_{local} estimates in Figure 14 exceed 150 °C, which is still below the lowest temperature PMMA degradation process (165 °C, [134]). Infrared spectroscopy of composites before and after photothermal treatment indicated no evidence of bulk degradation (Figure 15). Peaks associated with PMMA [135–138], such as 1721 cm^{-1} (C=O stretching), 1432 cm^{-1} (CH3 stretching), and 1189 cm^{-1} (-OCH3 stretching), remain unchanged with treatment. Residual DMF from sample casting contributes to features at 1088 (C-N) and 1676 cm^{-1} (C=O), which decrease in size with heating (T_{boil} for DMF = 153 °C).

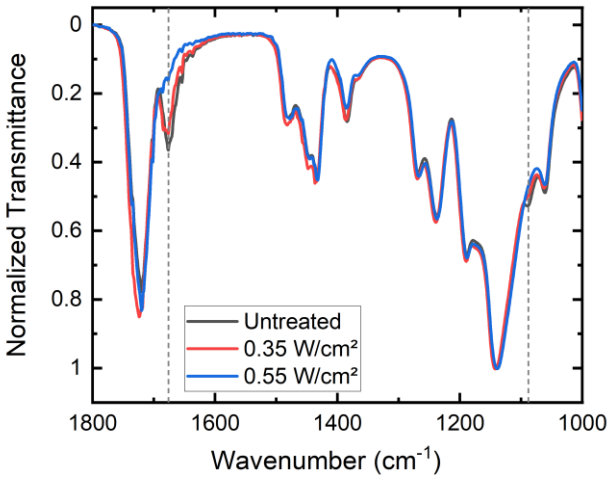

Figure 15: FTIR of 0.125 wt% samples before and after photothermal treatment at 0.35 and 0.55 W/cm^2. Plot is normalized to 1140 cm^{-1} (corresponding to C-O) for ease of viewing. Vertical dashed lines indicate 1088 and 1676 cm^{-1}, which are associated with DMF (C-N and C=O bonds, respectively) and decrease with treatment, as the T_{boil} of DMF is 153 °C and local temperatures are estimated to approach that (0.35 W/cm^2 had estimated local temperatures of 110 °C, while 0.55 W/cm^2 had estimated local temperatures of 140 °C. Peaks associated with PMMA, such as 1721 cm^{-1} (C=O stretching), 1432 cm^{-1} (CH_3 stretching), and 1189 cm^{-1} (-OCH_3 stretching), remain unchanged with treatment, suggesting no PMMA degradation from photothermal treatment

Transmission electron microscopy enabled visualization of the cross-section of the MWCNT network (Figure 16). Current flows into or out of the page in this geometry. Particle counting (see Section 2.2.2 for procedure) was consistent with the expected MWCNT loading with roughly twice as many MWNCT observed per image for 0.25 wt% composites as 0.125 wt% cases. The number of MWCNT in each case was the correct order of magnitude considering the volume accessed (as based on the image size and 90 nm thickness of microtomed slide) and the stated MWCNT concentration. Adequate dispersion was observed with only 1/500 tubes appearing in non-network related aggregates (see Figure 16b) characterized by tangled nanotubes and general collection of material no larger than 500 nm across.

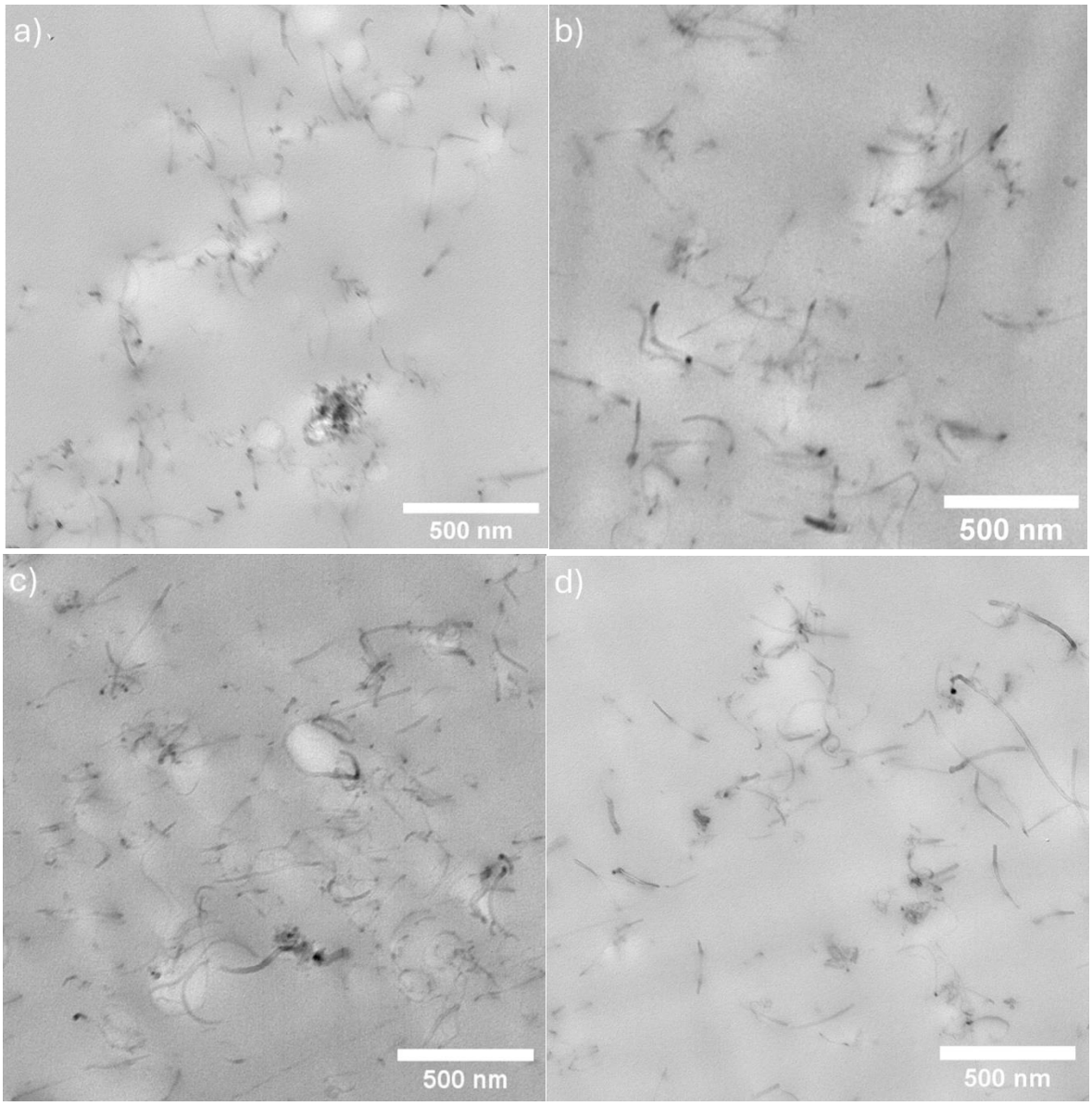

Figure 16: Transmission electron micrographs of MWCNT:PMMA composite samples showing the distribution of nanotubes. a) 0.125 wt% untreated, b) 0.125 wt% treated with 0.45 W/cm^2 for one hour, c) 0.25 wt% untreated, d) 0.25 wt% treated with 0.5 W/cm^2 for one hour. Figure a) includes a cluster of tangled nanotubes mentioned in the text. Images were analyzed by measuring the size of individual nanotubes and counting tangled clusters of nanotubes.

Images were analyzed for changes in dispersion and general clustering before and after treatment. The estimated number of nanotube clusters (found by counting the number of tangled clusters across all images and dividing by the number of images analyzed) is presented in Table

1b. There is no consistent trend for the number of clusters after photothermal treatment, which is consistent with the discussion above. Furthermore, if polymer degradation were present due to treatment, it might manifest as additional electron-absorbing material forming around each carbon nanotube. MWCNT diameter was studied for composites having experienced 0.6 W/cm^2 intensity light from 2 to 20 hours (Table 1c). No significant trend was observed from as-made sample MWCNT diameter (9.6 ± 4.1 nm) to that in a composite treated for 20 hours (12.0 ± 3.6). Thus, electron microscopy and spectroscopy studies are consistent by showing no systematic evidence of matrix degradation or MWCNT damage.

Table 1: Features in TEM images of 0.125 wt% samples treated at 0.6 W/cm^2.

a) Time treated (hr)	b) Number of Nanotube Clusters per Image	c) Diameter of Nanotubes (nm)
0	0.59	10.5 ± 3.9
2	0.83	10.5 ± 3.5
5	0.35	10.9 ± 3.9
10	0.06	11.3 ± 4.2
20	0.58	11.1 ± 3.8

2.4 Conclusions

Photothermally heating MWCNTs in PMMA has been shown to improve the electrical conductivity of the composites by 2.25 times the initial conductivity. The conductivity change was based upon the local temperature of the sample, which could be controlled with the incident laser intensity, as the local temperature provide increased contact between nanotubes without sacrificing the bulk distribution of the MWCNTs. Samples were tested in a range of concentrations and laser intensities to manipulate the heating conditions to fully map out these conductivity improvements.

There are a few interesting avenues for additional research. For example, a shorter nanotube may be more free to move within the sample, thus allowing better overall contact between nanotubes to be achieved with photothermal heating and consequently higher conductivity improvements. Similarly, the conductivity gains may be improved by changing surfactants to one more prone to degradation. While Triton X-100 (as used in this work) is a very common surfactant, it requires temperatures above 200 °C [139] to degrade or evaporate. In contrast, a surfactant such as polysorbate 20 (referred to as Tween 20) exhibits a degradation around ~100 °C [140], and thus may degrade into a conductive carbonaceous material around the nanotube, providing a different mechanism of improving the conductivity.

Chapter 3: Water Evaporation from Hydrogels via Photothermal heating of Nanoparticles

3.1 Hydrogels

Hydrogels are crosslinked polymer networks known for their swelling ability. These water-based networks can then be engineered with specific structures to support cells, tissue growth, or mechanical stability. Stimuli-responsive hydrogels have become a subject of growing interest [141] recently due to their broad potential in applications such as water purification, tissue engineering, drug delivery, and more. These hydrogels respond to environmental stimuli through structural changes, mechanical properties, or chemical bonding energy. Environmental changes can include simple changes such as heat, pressure, or pH, but can also include more complex situations, such as the presence of specific enzymes or an electric field [142–146].

The potential for both quick water uptake and release through environmental changes has placed stimuli-responsive hydrogels as a contender for driving water purification processes [142,146–149]. Water purification through forward osmosis is one such process, where contaminated water is placed on one side of a membrane and a draw agent on the other. The draw agent applies osmotic pressure upon the water, pulling it through the membrane and separating the water from any contaminants. The now-fresh water can be separated from the draw agent, and the process can begin again with the reused draw agent [150–153]. The choice of draw agent is a critical factor in this process, as the energy requirements to separate the draw agent from the fresh water can rival that of other water purification techniques like forward osmosis [151,154], which reduces the application potential. In other words, increasing the water recovery rate or decreasing the energy of these water purification processes is limited by the draw agent. Thus, the potential for using stimuli responsive hydrogels to release water through environmental conditions alone would be a notable improvement in water purification processes.

For example, one of the most famous thermally-responsive hydrogels is poly(N-isopropylacrylamide) (NIPAM). When raised to 32 °C, NIPAM switches from a hydrophilic polymer to hydrophobic one, rejecting all water within the hydrogel as the polymer chains collapse in on themselves [148,155–158]. In the context of water purification, this allows for a quick transition between absorbing water and releasing it, without a large temperature increase. This 32 °C transition point is referred to as the lower critical solution temperature (LCST). The thermal response is reversible, such that once NIPAM is cooled below the 32 °C LCST, it will once again become hydrophilic. This relatively low LCST has led to a variety of interesting applications in biology and medicine [73], but also allows the release of water well below the vapor point of water, providing a natural solution to the energy intensive separation of water from the draw agent.

Promising results using hydrogels as water purification drivers have been reported [99,142,146], though there are other ways to utilize the hydrogels. For example, the structure of the hydrogels can be engineered to act as both membrane and draw agent [99,143,144]. Layering different types of hydrogels allows for the isolation of specific environmental responses that can increase the efficiency of a water purification system [159,160]. Alternatively, using hydrogels as the coatings of other structures can increase the mechanical stability of the hydrogels [161,162] while preserving their swelling potential. The hydrogel itself can also be made into micron-sized particles which increase the surface area to volume, creating microhydrogels that become more sensitive to the environment due to the quick diffusion of water through the microhydrogel, as compared to macrogels [163–166]. While microgels are of particular interest in biological applications due to their size and the quick swelling and collapsing of the gels [163,167], there has been interest in them as well for water purification [168–170].

Alternatively to physical changes, the chemical composition of the hydrogel can be modified to balance maximum water draw with water release [148,170–177]. In particular, the combination of NIPAM (a hydrogel with a strong LCST response) with sodium acrylate (SA) (an ionic hydrogel able to quickly draw water) has been of interest. However, the mixing of these hydrogels changes the water release and reduces the LCST response expected from NIPAM, encouraging more research into water removal processes from this composite hydrogel.

Deswelling can be triggered by several environmental parameters. The temperature of the hydrogel is a simple example. While this heat can come from a conventional oven, there has been much interest in utilizing photothermal heating to drive the dewatering process. Photothermal heating opens avenues for heat to come from the Sun, making hydrogel-based water purification processes accessible off the grid [42,178,179]. Beyond water purification processes, light controlled hydrogels have potential as biological switches [167], especially with the ability to tailor the nanoparticles to specific wavelengths.

While these works demonstrate excellence in application, few investigate the mechanics behind the deswelling process. However, understanding the deswelling process gives insight into the limiting factors preventing further energy or time-based improvements to water purification processes. Therefore, this dissertation investigates the differences between the thermally driven deswelling via either conventional heating or photothermal heating. Furthermore, the photothermal capability of a biologically friendly material – melanin nanoparticles – was compared to the more commonly used metallic nanoparticles, to better understand how the deswelling process may change with the heating source. In addition, the basic behaviors of the composite hydrogel were tested, including the swelling properties, dependence on surface area for deswelling, and the LCST.

For this study, hydrogels were made with and without nanoparticles, then either treated in a conventional oven or through photothermal heating. The water loss from the hydrogel and the temperature were tracked over time and used to compare the water loss process from each heating method (oven heating, photothermal heating with GNP, photothermal heating with MNP).

3.2 Materials and Methods

3.2.1 Hydrogel Synthesis

The hydrogels used in this work were based on previously established procedures [169,170], using an equal parts mix of sodium acrylate (SA) and N-isopropylacrylamide (NIPAM). Throughout this work, the hydrogel powder will refer to the dry, 2-30 μm diameter microhydrogel particles (Figure 17a). More broadly, 'hydrogel' will refer to the collection of powder that has been swollen with water (resembling a vicious, sticky gel, Figure 17b) and potentially de-swollen but not ground up, and thus treated as one object.

All materials were used as received. To synthesize the microhydrogels, one gram each of SA (Sigma Aldrich) and NIPAM (Fisher Scientific) were dissolved through vigorous magnetic

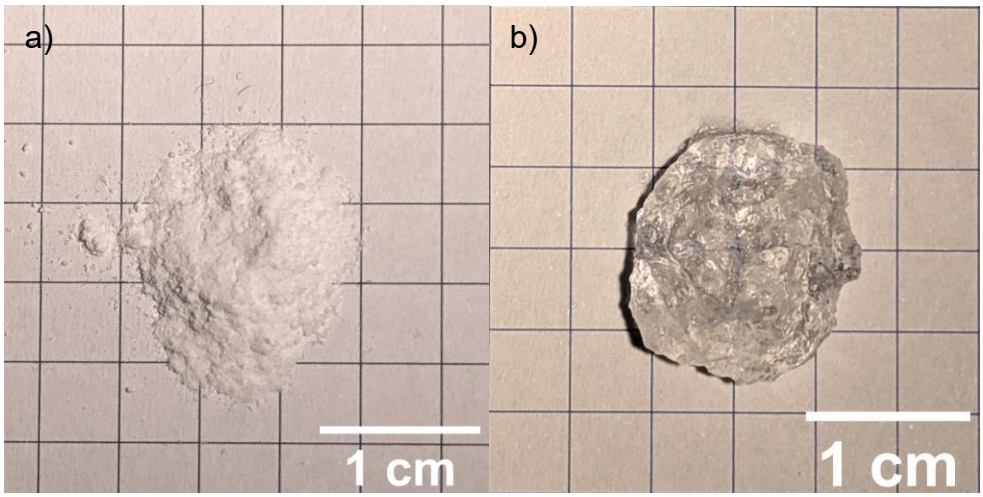

Figure 17: Photo of a) dried hydrogel powder and b) swollen hydrogel

stirring in 9.13 g deionized (DI) water (VWR 325 hotplate/stirrer). Then 0.028 g of the crosslinker N,N′-methylenebisacrylamide (MBA, Sigma Aldrich) was added and stirred vigorously. Nanoparticles were added according to the desired final concentration (8×10^{-4} wt% for GNP, and 3.1 wt%, 4.1 wt%, and 14.6 wt% for MNP), followed by the addition of 0.02 g of the initiator ammonium persulfate (APS, Sigma Aldrich). Concentration of the nanoparticles was set to have equal extinction values at the laser wavelength for both nanoparticles, or in other words, a 2×10^{-4} wt% GNP concentration had equal extinction at 520 nm as the 0.8 wt% MNP concentration. To ensure the homogeneous dispersion of the nanoparticles, the solution was sonicated with a wand sonicator (Misonix Wand Sonicator 3000, 20kHz one second pulses with one second rest times) until the solution reached 70 °C, at which point, the solution turned into a gel and the nanoparticles were locked in place within the polymer network. The gel was placed in a 70 °C oven overnight to ensure the polymerization stopped and to remove excess water. The hydrogel was then removed from the oven and washed over a period of 48 hours, where water was replaced at least twice a day to remove any leftover reactants. Finally, the swollen hydrogel was placed in an 80 °C oven to remove all water.

To create the microhydrogel, the fully dried hydrogel was cryo-ground (SPEX SamplePrep 6870 freezer mill) into 2-30 μm diameter particles (Figure 18 inset) and stored in airtight glass containers until testing. Microhydrogel size was determined through dynamic light scatter (DLS) of the dry hydrogel powder in acetone (Malvern Zetasizer Nanoseries with temperature control) and through observation under a Nikon 80i Fluorescence Microscope (20x magnification). The DLS measurement determined the microhydrogel diameter to be 3.7 μm ± 0.5 μm, while the microscope measurement found the highest number of particles in the 3-6 μm, with more that were significantly larger (Figure 18). The microscope measurements resulting in larger particles than

the DLS measurement is expected due to the likely clumping of the powder, as this would be broken up in solution. Thus, the average size of the microhydrogel was considered to be about 4 μm for the remainder of this work.

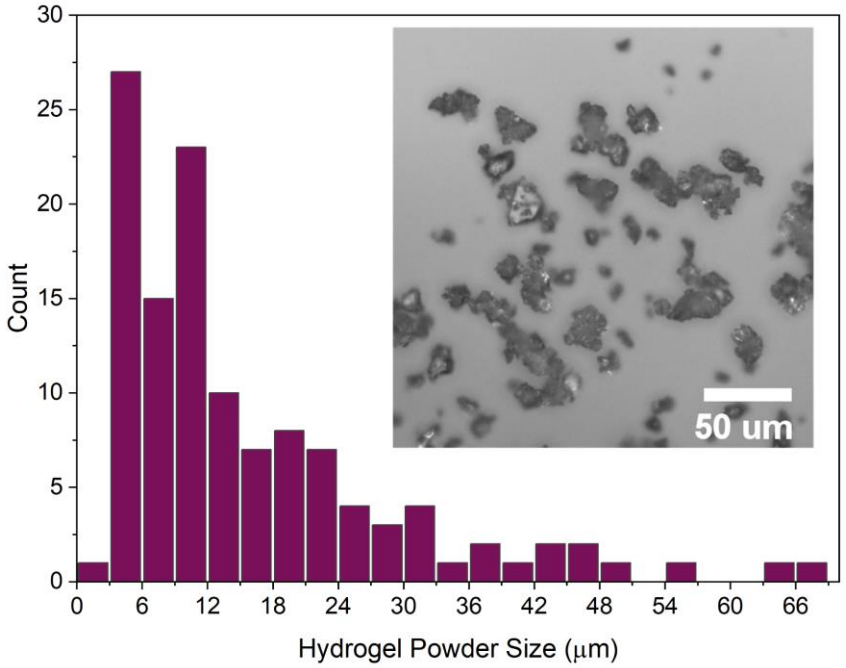

Figure 18: Microhydrogel diameter as measured from microscope images of powder (inset).

3.2.1 Nanoparticle Synthesis

Gold nanoparticles were harvested from aged cetyltrimethylammonium bromide (CTAB) stabilized gold nanorods. Absorption spectroscopy (Agilent Technologies Cary 60 UV-Visible Spectrometer) indicated a peak LSPR absorption of 542 nm (Figure 19a). Transmission electron microscopy (TEM, Hitachi BioTEM HT7800) (Figure 19b) analysis of 190 particles on stabilized TEM grids (Ted Pella Inc, Prod 01800-F, Formvar/Carbon support films, 200 nm Cu mesh) confirmed that the gold nanoparticles used in the hydrogels consisted of 80% spheres (diameter 44 ± 23 nm), 14% triangles (height of 113 nm ± 65 nm), and 6% rods with an aspect ratio of 3.5 (102

nm ± 58 nm by 29 nm ±14 nm). As the absorption (LSPR peak) matches well with the laser wavelength, the mixture of shapes generalizes the photothermal heating process described later to include non-specific particle sizes or shapes. All of the gold nanoparticles are much smaller than the average hydrogel power as well, such that the different shapes should not interact with the hydrogel differently.

Melanin nanoparticles were synthesized from the neutralization and auto-oxidation of dopamine hydrochloride [60,61]. To make the nanoparticles, 90 mL of DI water was heated and held at 50 °C on a hotplate. Under vigorous stirring, 180 mg of dopamine hydrochloride (Sigma Aldrich) was added, followed by 760 µL of 1 N NaOH solution (Sigma Aldrich). Upon the addition of NaOH, the solution immediately turned yellow, then gradually transitioned to a dark brown (over approximately 10 minutes). The solution continued to stir while held at 50 °C for five hours to form nanoparticles of approximately 100 nm diameter. The size of the MNPs was controlled by the time and temperature of this solution. After five hours, the solution was centrifuged (Eppendorf

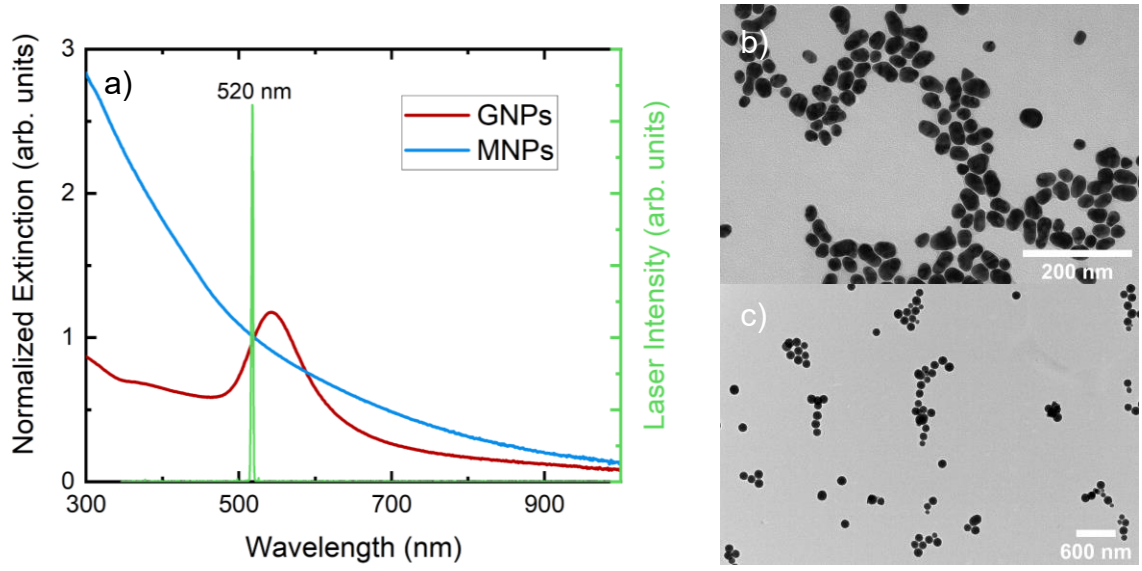

Figure 19: Extinction of stock solutions of GNP and MNP, normalized to the laser wavelength at 520 nm. TEM images of b) GNP and c) MNP.

Centrifuge 5702) at 4400 RPM for three minutes and the top 60% was collected as the supernatant. This supernatant, which contained the desired MNPs, was further centrifuged (Eppendorf Centrifuge 5418) at 14000 RPM for 3 minutes to form a pellet, which was extracted and rehydrated with fresh DI water.

The MNPs were measured with absorption spectroscopy to confirm the existence of a broad absorber (Figure 19a). The MNPs were then dried onto TEM grids (Figure 19c). An analysis of over 350 particles indicated an average MNP size of 78 nm ± 25 nm. The MNPs were added into the hydrogel solution immediately to prevent aggregation.

3.2.3 Thermal Treatment

Thermal treatment of the hydrogels was performed while the hydrogels were suspended on a clear, monofilament nylon string, such that all sides of the hydrogels were exposed to the air (Figure 20). This also isolated the hydrogels from any heat coming off any surface it otherwise may have been placed on. Room temperature measurements were taken by leaving the hydrogel in a well-ventilated space. Oven measurements were done in a laboratory oven with a vent at the top (VWR 1300U Oven). Photothermal treatment was done with a 0.5 W 520 nm diode laser beam expanded to cover the entire hydrogel, resulting in a 0.25 W/cm^2 intensity. Thermal measurements were taken by placing the K-type thermocouple on the hydrogel (RisePro Thermocouple). Temperature and humidity were monitored for room temperature, photothermal and low temperature oven treatments using a relative humidity meter. Samples were weighed (Ohaus Pioneer Balance, 0.001 g) at regular intervals throughout treatment in order to track water loss. The initial mass for the swollen hydrogel was kept at 0.5 grams during thermal treatment unless otherwise noted (as in Section 3.3.1). The mass of the hydrogels was monitored throughout the deswelling process for all treatments. The treatment concluded once 97% of the water had left the

hydrogel, as determined by the starting mass of the sample and initial water content. The concentration of nanoparticles within the hydrogel was determined and changed by mixing a microhydrogel containing nanoparticles with a microhydrogel without nanoparticles. This is discussed further in Section 3.3.2.

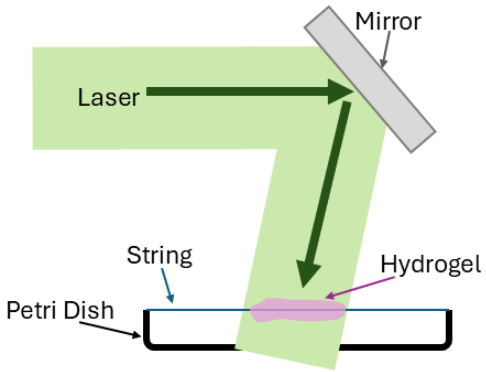

Figure 20: Depiction of hydrogel on string for treatment. The laser beam is expanded to cover the entire hydrogel, which is suspended on a string that is stretched over a petri dish.

3.3 Characterization of the Hydrogel System

This work is interested in the differences between the deswelling process for photothermally heated and oven-heated hydrogels. However, there are some basic system characteristics that must be understood before directly comparing the deswelling behaviors. These include the swelling characteristics of the hydrogels, the LCST of the mixed-polymer system, and the nanoparticle concentrations and spacings throughout the process.

3.3.1 Basic Swelling and Deswelling Behavior

Before treatment, hydrogels were swollen to a specific water content, which is referred to as the Q value:

$$Q = \frac{w_t - w_d}{w_d} = \frac{\Delta w}{w_d} \tag{4}$$

where w_t is the total mass of the swollen hydrogel (powder plus water added), and w_d is the mass of just the dried hydrogel powder. Using this equation, a swollen hydrogel can be said to have Q times the amount of water as the mass of dry hydrogel powder. The visual differences in Q values can be seen in (Figure 21a-c). The Q value will change with time as the hydrogel loses water. The swelling behavior of the hydrogels was tested by placing 0.1 g of hydrogel powder into a water-permeable dialysis bag (Sigma Aldrich). The bag was then placed in an excess of water for approximately nine days. At regular intervals (twice a day), the hydrogel and bag were removed

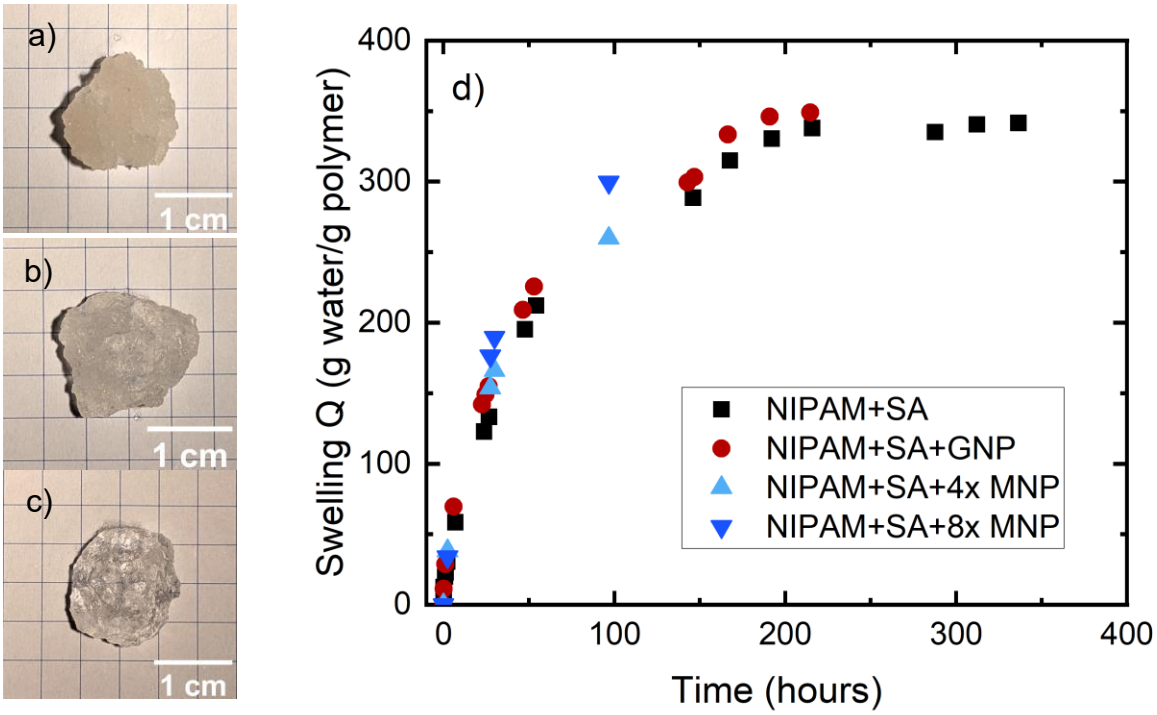

Figure 21: Images of a swollen hydrogel at a) Q=6, b) Q=12, and c) Q=24, made by adding the appropriate amount of water to dried hydrogel powder, mixing, and allowing it to sit for several minutes until the powder had fully absorbed the water. The hydrogel becomes increasingly translucent with the addition of water, but also loses structural integrity. d) Swelling value over time when hydrogel powder is placed in a dialysis bag and allowed to freely absorb water.

from the water and weighed, and the swelling of the hydrogel calculated (Figure 21d). Any water on the surface of the bag was wiped off before measurement, and the weight of the bag was subtracted from the measured value. This was repeated for two independent batches of hydrogels, to confirm consistency in the procedure, as well as for a hydrogel with gold nanoparticles, to test any potential interference caused by the nanoparticles.

The swelling behavior was consistent across all hydrogels (Figure 21d), regardless of the addition of nanoparticles, and matched previously reported data [169], indicating that the nanoparticles do not interrupt nor change the swelling behavior. Past work has suggested that while the nanoparticles (tens to hundreds of nanometers in diameter) may interrupt the hydrogel chemical crosslinks (thus increasing the swelling ratios possible, as the hydrogel is bound to itself and can contain more water between polymer chains [180]), they may effectively act as physical crosslinks (by holding the hydrogel together, and decreasing the swelling ratio), thus keeping the swelling behavior consistent with or without nanoparticles [181–184].

Although the LCST of NIPAM is expected to be approximately 33 °C, this will change with the addition of SA. To gauge the LCST for the mixed hydrogel, the hydrogel was swollen and measured by DLS while undergoing thermal treatment. When a swollen hydrogel becomes hydrophobic, it experiences a collapse and formation sphere-like structures expected to be the similar size as the microhydrogel particles measured earlier. This size change can be tracked with DLS, where a decreasing particle size suggests a transition to hydrophobic behavior. While DLS is typically not suited for non-spherical and non-monodisperse particles, and thus results in fairly noisy data, the general temperature transition can still be measured.

Figure 22 shows the diameter (as measured by DLS) for NIPAM, SA, and the NIPAM+SA used in this work. NIPAM and SA were synthesized with the same method as described previously

and simply replaced the other polymer in the recipe. The smaller initial size for the NIPAM and SA swollen hydrogels is likely due to the cryogrinding process, as the NIPAM and SA were both cryoground in smaller batches than the NIPAM+SA microhydrogel. Cryogrinding small batches achieves smaller particles than a larger batch. As the goal of this plot is to note the transition of the polymers, which should be unaffected by the starting size of the microhydrogel.

NIPAM shows the expected decrease at 33 °C [148,155–158], which is marked by a vertical line in Figure 22. There is a decrease in the size of the SA particles from 45 °C to 90 °C, suggesting a wider temperature range through which SA transitions from hydrophilic to hydrophobic (as compared to the ~15 °C range for the NIPAM). The NIPAM+SA, which is the recipe used throughout this work, has a much noisier size distribution with increasing temperature, but does have a generally decreasing size with heat. This suggests that there is still thermal response of the NIPAM+SA used for deswelling in this work, however, that response requires a higher temperature than pure NIPAM.

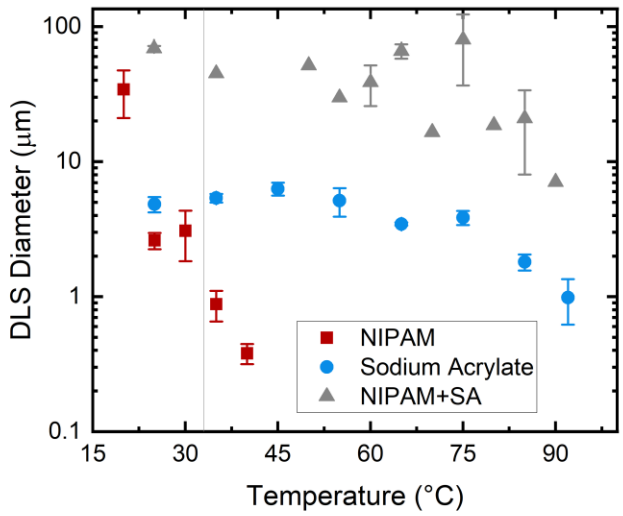

Figure 22: DLS measurement of heated swollen hydrogel. The large error bars are an artifact of the lack of uniformity of the hydrogel particles, as DLS measurements are not well suited to particles with large polydispersity.

The surface area of the swollen hydrogel is an important factor in how quickly water can escape it. Figure 23 displays the deswelling curve (evaporated water over time) of initially Q=24 hydrogels with variable starting masses from 0.5 to 3 grams, and thus with variable starting surface areas. A smaller initial mass results in more evaporated water at a given time. This can be further seen in Figure 23 inset, where a six times increase in mass nearly doubles the time for half of the water to leave the hydrogel. In order to remove this variable from consideration, the starting mass of the total hydrogel was kept constant at 0.5 g for all further experiments, as the goal was to investigate deswelling behaviors driven by heat. This did result in the mass of dried hydrogel (once the water fully leaves) varying in size when the Q value was changed, where a Q=6 hydrogel had 0.07 g of dry hydrogel, while Q=24 had 0.02 g. That being said, the difference (0.05 g of dry hydrogel powder, or 10% of total starting mass) is relatively small, such that other variables impact the water loss more considerably.

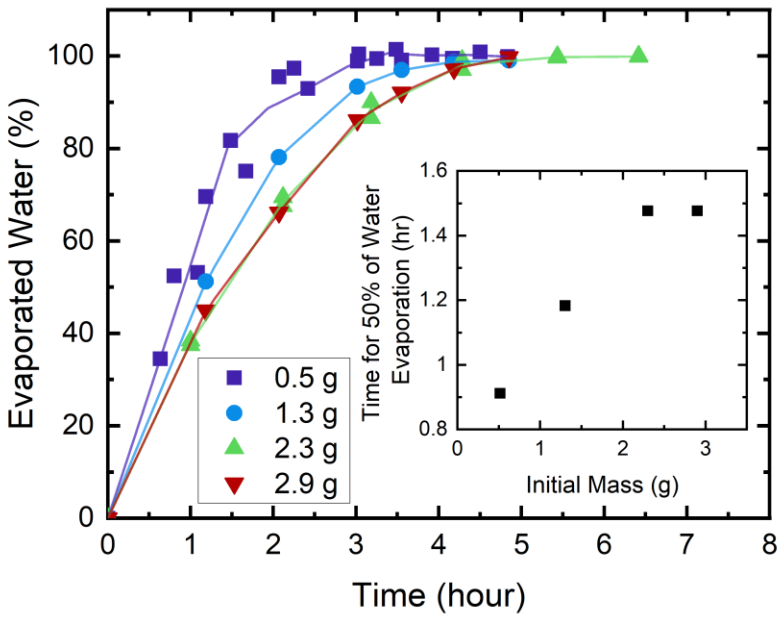

Figure 23: Deswelling of hydrogels with varying surface areas. There is a steady increase in the time for 50% of the water to come out with increasing overall surface area.

3.3.2 Particle Concentrations and Length Scales

The separation of the nanoparticles is an important factor in the heating process, as the more isolated a particle is or the fewer nanoparticles there are, the higher the temperature difference between the global and local temperature. The spacing within the system used in this work will be described here.

As discussed previously, the starting mass of the swollen hydrogels was kept at 0.5 grams to remove dependence on the surface area. This means that

$$m_{water} + m_{hydrogel\ powder} = 0.5\ grams. \quad (5)$$

The relationship between the mass of the water and the mass of the dried hydrogel was determined by the swelling:

$$Q = \frac{m_{water}}{m_{\ hydrogel\ powder}} \quad (6)$$

Thus, the amount of hydrogel powder in a swollen sample was determined using the Q value:

$$m_{hydrogel\ powder\ } = \frac{0.5\ \mathrm{g}}{Q+1}. \quad (7)$$

The amount of hydrogel powder used for GNP hydrogels with varying Q values is in Table *2*.

Because there is a different amount of hydrogel powder in each sample if a single, nanoparticle-containing hydrogel formulation was used, there would be a different number of nanoparticles present in samples with different Q values (Table 2). Furthermore, the number of

Table 2: Hypothetical gold nanoparticle concentration in hydrogel of different swellings using hydrogel with 2.46×10^{10} particles per gram polymer

starting Q (g water/g polymer)	Total Starting Mass (g)	Mass of Dried Hydrogel (g)	Mass of Water (g)	Particles/g polymer	Particles/g water
6	0.5	0.071	0.428	2.46×10^{10}	4.10×10^{9}
12	0.5	0.038	0.462	2.46×10^{10}	2.05×10^{9}
24	0.5	0.020	0.480	2.46×10^{10}	1.03×10^{9}

particles per gram of water would be different in these three swelling examples, making the Q=6 case likely an overall warmer sample, simply due to the presence of more heaters within the system. To combat this, the hydrogel and particle concentrations were prepared in such a way as to keep the particle number per gram of water constant across different samples, which necessarily means that at lower values of Q, the number of particles per polymer must decrease.

The particle number per water ratio of 1×10^{9} particles/g water was chosen as the desired ratio for all samples. The standard hydrogel recipe with GNP created a hydrogel powder that was 8×10^{-4} wt% GNP to polymer, or 2.46×10^{10} particles/g polymer. In a Q=24 hydrogel, this creates a ratio of 1×10^{9} particles/g water, as desired. However, a Q=6 hydrogel created using the same recipe had a 4×10^{9} particles/g water ratio. This is self consistent, as the Q=6 hydrogel has four times more hydrogel powder than Q=24, and thus the ratio is also four times greater. Therefore, to meet the goal of maintaining an equal number of particles per water, the Q=6 swelling must be made from a hydrogel with a quarter the concentration of nanoparticles as the standard hydrogel recipe.

This could have been done with a new recipe for the hydrogels, but it could also be done by simply mixing a hydrogel powder containing nanoparticles (H-GNP) with a hydrogel powder containing no nanoparticles (H). In such a case, the Q=6 hydrogel would be made with one part H-NP and three parts H. This creates a hydrogel with 6.9×10^{9} particles/g polymer, or a 2×10^{-4} wt% GNP, which corresponds to a 1.2×10^{9} particle/g water ratio, as desired (Table 3).

Table 3: Experimental gold nanoparticle concentration in hydrogel of different swellings made by varying the number of particles per polymer

starting Q	Total Starting Mass (g)	Mass of Dried Hydrogel (g)	Mass of Water (g)	Particles/g polymer	Particles/g water
6	0.5	0.071	0.428	6.89×10^{9}	1.15×10^{9}
12	0.5	0.038	0.461	1.28×10^{10}	1.07×10^{9}
24	0.5	0.020	0.480	2.46×10^{10}	1.03×10^{9}

To summarize, the method utilized for this research proceeded as follows: starting with the microhydrogel powder with 2.46×10^{10} particles/g polymer, microhydrogel powder with no particles was added to reach the necessary particle concentration that kept the particle per gram water ratio constant at 1×10^{9} particles/g polymer.

The downside of this method was that the separation of particles within the hydrogel would vary between each hydrogel, which is not ideal for comparison of different hydrogels. However, the nature of microhydrogels minimizes this effect. Again, using the GNP samples as an example, the average density of the polymer mixture as 1.3 g/cm^2 was used to determine the spacing of the particles. In the standard recipe (2.46×10^{10} particles/g polymer), each gold nanoparticle in the dried hydrogel was approximately 4.1 μm away from the closest other nanoparticle. However, the microhydrogel size was determined to be approximately 4 μm, implying that each microhydrogel contained, on average, only one nanoparticle.

In comparison, the hydrogel recipe that would have resulted in four times less nanoparticles (as required for a 1×10^{9} particle/g water ratio when swollen to Q=6), would lead to nanoparticles being approximately 7.4 μm away from any other nanoparticle in the hydrogel powder, on average. This increased spacing would have resulted in microhydrogels which have, on average, either one or no nanoparticles. Thus, making a new hydrogel with lower concentration is equivalent to the method used in this work of mixing H with H-GNP. In both cases, the microhydrogel has either no particles or just one particle.

The melanin nanoparticles were larger (diameter of 78 nm ± 25 nm), and more were required to match the extinction at 520 nm as compared to the GNP. The lowest concentration of particles was 3.1 wt%, corresponding to a separation of approximately 0.3 μm and a particle per water value of 4×10^{12} when at Q=24 swelling. The same particle per water amount in a Q=6

swelling was done with a 0.8 wt%, again made using one part H-MNP and three parts H. This lower concentration results in a separation of 0.83 μm. Both of these concentrations and all others done for the MNP had multiple MNPs in each microhydrogel particle. This may have interacted with the deswelling behaviors slightly in the diluted cases, as in these cases, the melanin nanoparticles were not as evenly dispersed. This was more apparent for the low concentrations of Q=6 cases, as these are mixed with the most non-nanoparticle microhydrogel.

Throughout this work, microhydrogels with nanoparticles and without nanoparticles were mixed to create variable effective concentrations. While all the following notation will reference the comparative extinction values of these hydrogels at the laser wavelength to the standard GNP recipe extinction value, the particles per water would also be a reasonable equivalent naming convention (using the baselines of 1×10^{9} particles/g water for GNP hydrogels and 4×10^{12} particles/g water for MNP).

3.4 Hydrogel Deswelling

With a more complete understanding of the hydrogel system, attention can now turn to how the application of heat impacted the deswelling behaviors. This section will compare the deswelling behavior of hydrogels in three different heating scenarios: ambient heating at room temperature, heating within an oven, and photothermal heating with the two types of nanoparticles. A visual for the hydrogel during ambient deswelling and photothermal heating of GNPs is shown in Figure 24. The analysis will begin with typical deswelling curves, then a discussion of the impact of starting swelling on the deswelling process, followed by investigation of the role of humidity and heat.

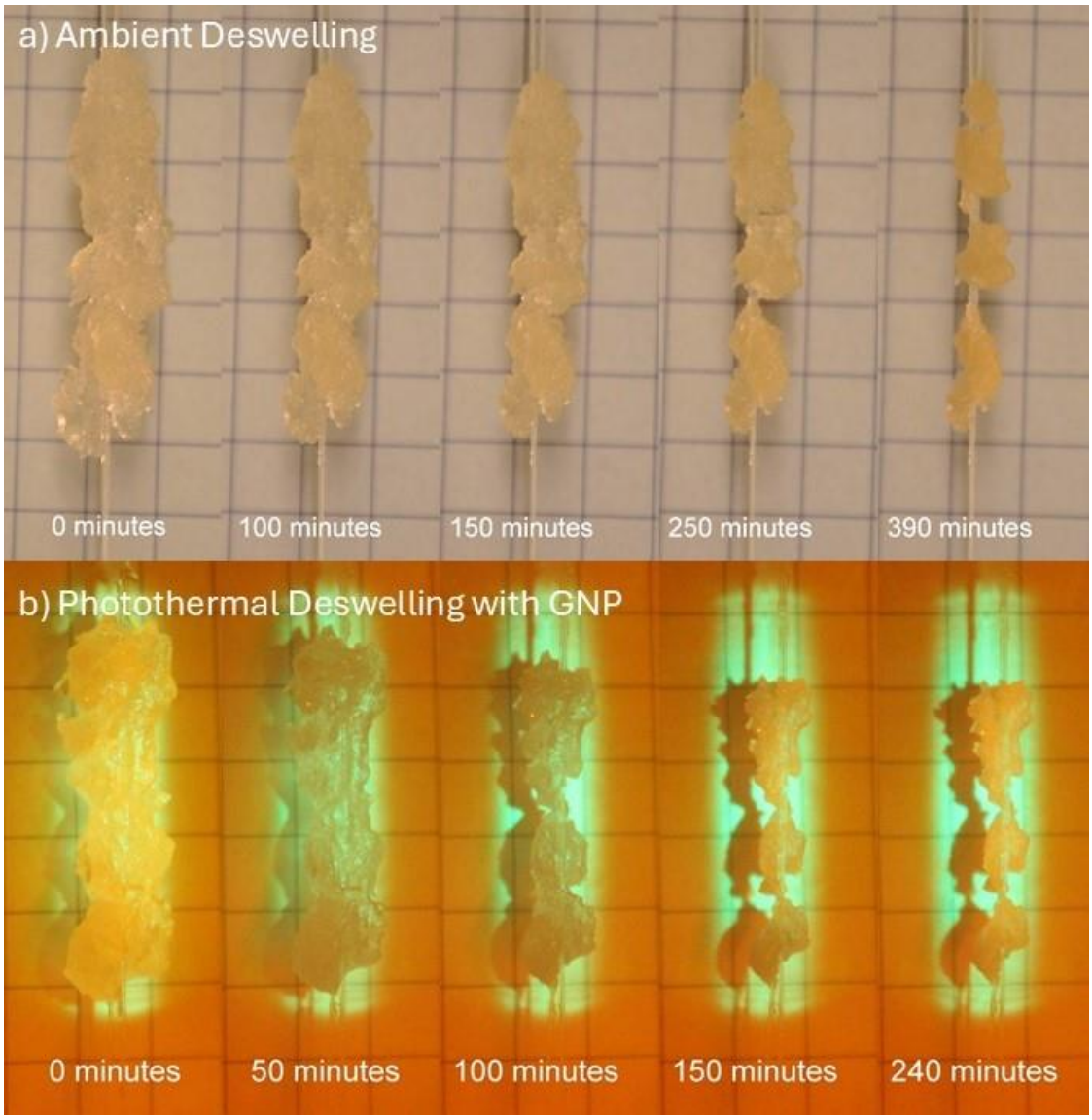

Figure 24: Images taking during the deswelling process of a Q=6 hydrogel in a) ambient conditions and b) with embedded GNP undergoing photothermal heating. There is a 0.5 cm by 0.5 cm grid pictured behind the hydrogels.

3.4.1 Simple Deswelling Behaviors

Figure 25a and Figure 25b shows a typical deswelling curve and the corresponding temperature of the hydrogel for the different heating methods starting at the same Q=12 swelling amount. Oven heating was selected to be done at the hydrogel temperature measured at the end of

photothermal heating of GNPs. The hydrogels used in the ambient and oven cases contained no nanoparticles, while the MNP photothermal heating case used hydrogels containing nanoparticles with two times the extinction value of the GNP case, which corresponds to a MNP concentration of approximately 3.1 wt%.

Looking first at Figure 25b, the temperatures during photothermal heating ranged between the temperatures from ambient deswelling temperatures before the laser was tuned on to temperatures of the oven deswelling process at the end of the photothermal deswelling process. The temperature during photothermal heating is due to the water content and spacing of the nanoparticles, which will be discussed further later. The 2x extinction concentration of MNP and 1x extinction concentration of GNP resulted in similar temperatures. Ambient deswelling conditions exhibited temperatures lower than room temperature, suggesting evaporative cooling (which occurs as evaporating water takes energy, and thus heat, with it from the sample, resulting in a cooling effect).

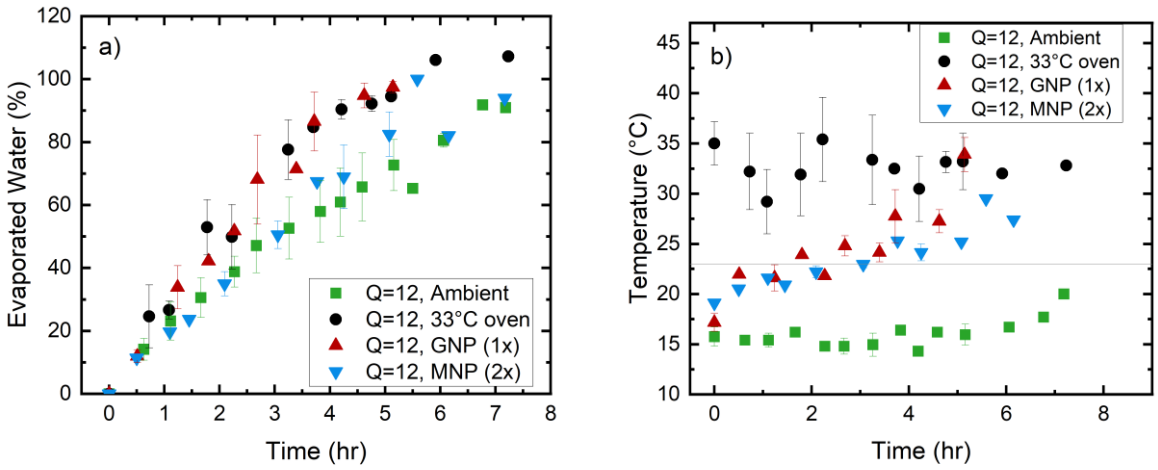

Figure 25: The a) evaporated water and b) temperature over deswelling time. Points are averaged within groups of data within 30 minute increments. The horizontal line in b) marks room temperature.

Figure 25a shows the water loss over time. The ambient conditions resulted in the slowest water evaporation, as expected, however, the 2x extinction concentration of MNP appeared to have a very similar rate of water loss, despite being at a higher temperature for most of the deswelling process. Interestingly, the GNP and 33 °C oven heated hydrogels had similar rates of water evaporation, although the GNP-hydrogel was measured at a lower temperature than the oven except for at the very end of the deswelling process.

Figure 25 gives a few insights into the deswelling process. Firstly, the two photothermal particles are not driving the deswelling process at the same rate, suggesting that the MNPs are a less efficient photothermal heater, especially because there is a higher extinction value for the MNP than the GNPs. This is an expected outcome, however, as GNP are an excellent photothermal converter with a conversion efficiency at minimum to be 70% [19–21], while MNPs are reported to have conversion efficiencies around 40% [66,68,185]. Secondly, comparable deswelling rates of the GNP photothermal heating and the oven heating would suggest higher temperatures driving the photothermal deswelling process than what is measured in the bulk hydrogel.

To investigate the latter of these two insights, we can think about the geometry that occurs during hydrogel deswelling. As the hydrogel loses water and collapses, the nanoparticles gradually get closer together. This raises the bulk temperature, or average temperature, to be closer to the local temperature near the nanoparticles (Figure 26a, Figure 26b). The final temperature is thus also a rough measure of concentration, as if the nanoparticles have the same spacing at the end of the deswelling, the average temperature should be approximately the same for all deswollen hydrogels with that nanoparticle concentration. Plotting the temperature vs water content Q (Figure 26c) for GNP photothermal heating aligns with this conclusion, as the measured temperature of

the hydrogels is consistent for hydrogels of the same swelling, regardless of the starting water content.

The initial swelling does impact the overall rate at which water loss occurs, particularly at high initial swellings. To display this, the swelling over time is plotted for the 33 °C oven treatment, along with the time for half the water to come out for all heating cases. Using the 33 °C

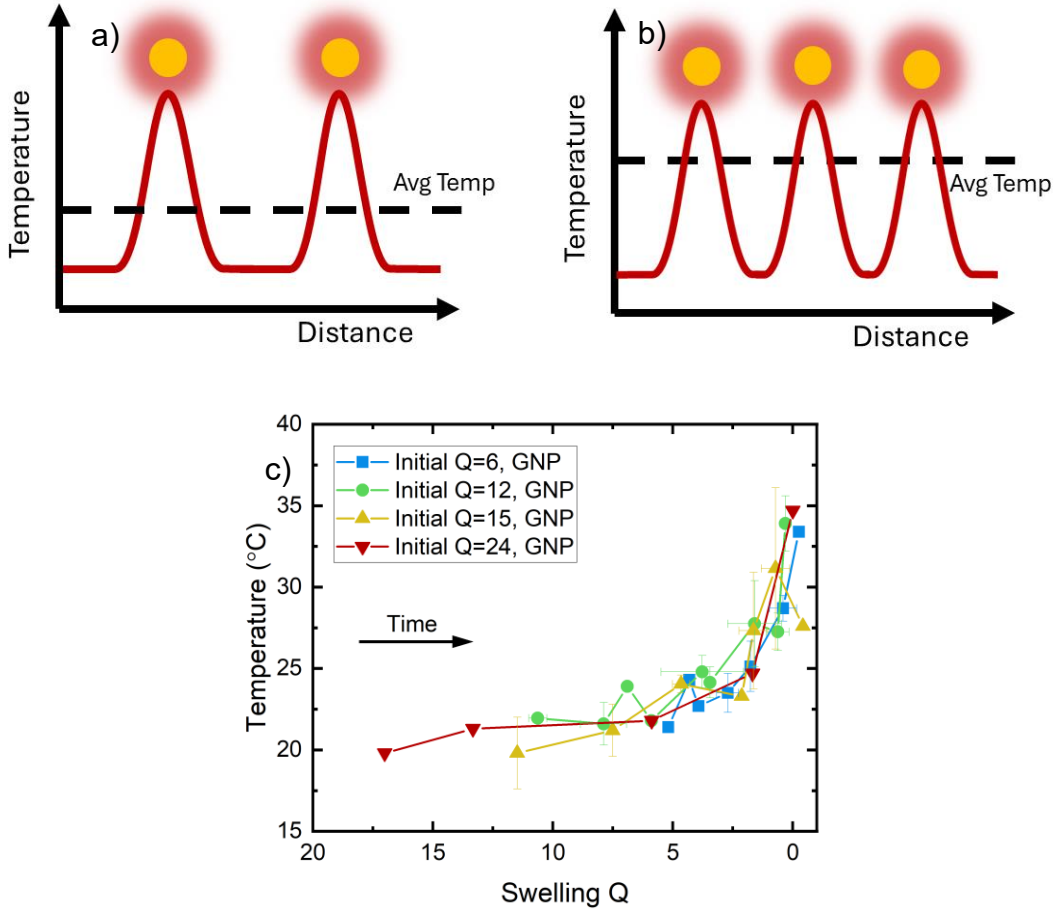

Figure 26: Sketch of how local temperatures contribute to the global temperature, such that (a) nanoparticles with more separation will result in a lower global temperature than (b) nanoparticles with less separation. c) Temperature of a GNP hydrogel undergoing photothermal heating plotted against the swelling throughout the deswelling process. Initial temperature data (when the laser was not on) is removed. In this plot, increasing treatment time goes from left to right. The temperatures for different hydrogel swellings collapse onto a similar curve, regardless of the initial swelling.

oven deswelling as an example, the time for 50% of the water to leave the hydrogel stayed in the range of 1.5 to 2.5 hours, regardless of the initial swelling and without a clear trend (Figure 27a). This necessitates that the rate of water evaporation must be greater for larger initial Q values, in order to remove more water molecules in the same amount of time. Figure 27b demonstrates this by plotting the swelling at a given time during the deswelling process. The slope of the data (the rate of deswelling) for varying starting Q values has a clear negatively increasing value (Figure 27b inset), as expected.

The likely reason for the differences in swellings is the nature of the water bonds within the hydrogel. Water within the hydrogel can be divided into bound water (directly bonded to the polymer chains or side groups within the hydrogel) and bulk water, also known as free water (water that is held through hydrogen bonds with other water, and can be considered independent to the polymer).

Using NIPAM as an example polymer, the bound water occupies two places along the polymer side chain (Figure 28). At the end of the NIPAM side chain, what is referred to as a "water

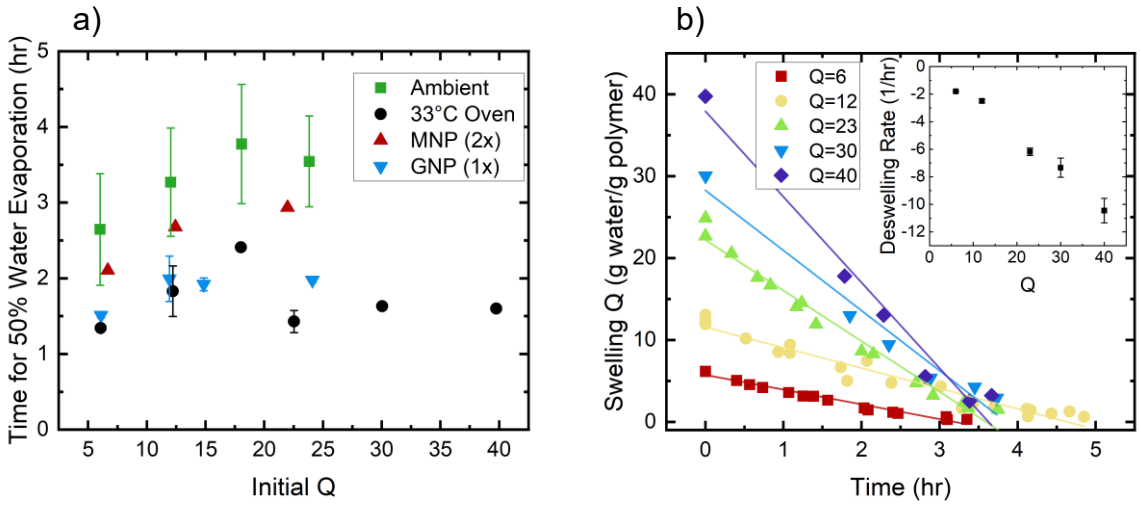

Figure 27: a) Time for 50% of the water to be removed from the hydrogel under various heating conditions. b) Swelling Q over time for initial Q=6 to Q=40 hydrogels in a 33 °C oven.

cage" surrounds the terminating isopropyl groups. During the LCST transition process when the hydrogel is heated, this is the first bound water to be expelled from the hydrogel [186], as it requires the lowest energy to be rearranged into bulk water [187]. The water bonded to the amide groups (C=O and N-H) is removed next, leaving the polymer chains free to form hydrogen bonds with each other (C=O — HN) [186,188]. These new intermolecular hydrogen bonds are what causes the globular state of the hydrogel. The heating of the hydrogel above the LCST changes the bonds within the hydrogel, causing shrinking of the polymer in on itself [158].

Because the experiments were generally conducted below the LCST of the mixed-polymer hydrogel, there was likely only water coming from the lowest energy bonds, or from the bulk water, especially during the initial deswelling process. However, with less water (a lower Q value), the hydrogel is directly bonded to a larger percentage of the water in the system. Increasing the initial swelling increases the percentage of water that acts as bulk water, which is able to evaporate off more easily than bound water, leading to the increased rate of water loss seen in Figure 27b. This is perhaps unintuitive, as more water would usually suggest more volume and thus longer times to remove the water; however, the volume is specifically held constant, and thus the only

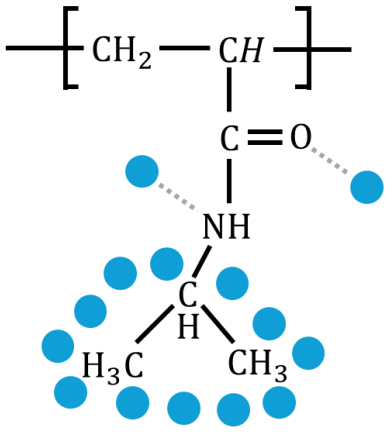

Figure 28: Diagram of water (blue circles) bonded to NIPAM.

change is the increased availability of water to be removed, as well as the proportion of water to polymer. This does bring additional nuance, as the constant volume means that a lower Q value will also contain more microhydrogel particles than a larger Q value. With more microgel particles, there are also more interfaces for water to leave from, and thus the time for diffusion through a microhydrogel would be reduced (as compared to a more swollen microhydrogel). This may lead to an increased water evaporation rate for the lower Q values, though this effect may be more noticeable in a study of isolated microhydrogels, rather than the groups of microhydrogels used here.

The preference for removing free water over bound water further suggests that within one sample, the initial deswelling process should be the quickest, as it will be removing free water. In contrast, the end of the deswelling would have a lower rate of water loss as the hydrogel has no water left available besides the bound water. The presence of a difference in rate between the beginning and end of deswelling will be discussed more in Section 3.4.2**.**

In summary, the hydrogels which underwent oven heating at 33 °C and photothermal heating via GNP were able to remove equal amounts of water in a similar amount of time, while photothermal heating with MNP required more time due to the lower photothermal efficiency of MNP [66,68,185] as compared to the GNP [19–21]. The swelling of the hydrogel did impact the water loss rate, as the time for 50% of the water to be removed remained constant despite increasing water content in the hydrogel, leading to an increased rate of water loss for higher initial water content. In addition, water left the hydrogel when the system was left at ambient conditions.

Evaporation in ambient conditions was very dependent on the humidity of the environment the hydrogel was in. Water will evaporate from a container of water left at room temperature, albeit slowly. The air of a more humid environment is less able to contain more water, causing the evaporation of liquid water to slow. This evaporation process drives the water loss from hydrogels in ambient conditions as well. The deswelling curve of evaporated water versus time (Figure 29a) shows that even for the same initial swelling, the humidity changes the rate of water evaporation. For example, a Q=6 swelling at a low humidity of 3.8 grams water per meter cubed (3.8 g/m^3) of air reached 50% of water evaporated in 2.1 hours, while a Q=6 hydrogel at a humidity of 9.4 g/m^3 took 3.6 hours to reach 50% water evaporated. The humidity also determined the temperature of the hydrogel (Figure 29b), as the lowest humidity is 2 °C cooler than the highest humidity, and all were well below the room temperature. This suggests that the hydrogel was experiencing evaporative cooling, which is the same process by which sweat cools the human body. As the water leaves the hydrogel, it takes heat with it, lowering the overall temperature of the sample.

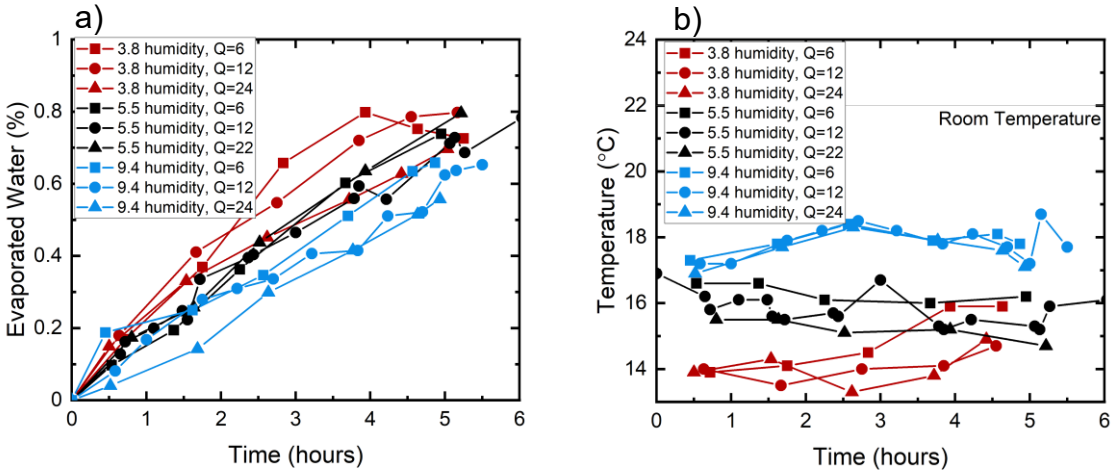

Figure 29: a) The evaporated water over time and b) temperature of hydrogels in ambient conditions at multiple swellings. The swelling dependence is less than the impact on humidity level, as the humidity drives the water loss in this hydrogel system.

The removal of water in ambient conditions is a relatively weak driver of the evaporative process. This can be seen in the dependence on humidity of other heated hydrogels (Figure 30), where humidity matters in the ambient case, but does not impact the oven or photothermally heated hydrogels. A hydrogel in ambient conditions showed a steadily increasing time to remove 50% of the water with increasing humidity. When compared to both oven heated and GNP photothermally heated hydrogels at a similar range of humidities, there was no dependence on the humidity. This implies that applying even minimal heat is enough to overpower the contribution of environmental humidity in driving water loss.

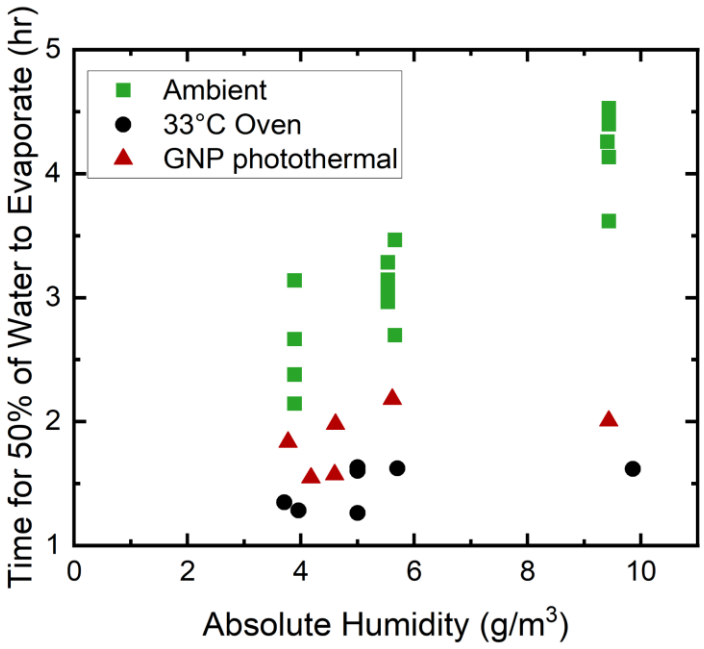

Figure 30: Time for 50% of water to leave the hydrogel for different humidities. Only the hydrogels at ambient conditions display any dependence on the humidity; any applied heat drives the water loss more effectively than the humidity of the environment is able to.

3.4.2 Impact of Heat on Water Output

So far, the impact from geometry, swelling, and humidity on the deswelling of hydrogels has been described, as well as a characterization of the system's more fundamental components that impacted the deswelling. The focus will now turn to a more detailed discussion of the impact of heat on the deswelling process.

The most simple case in modifying the hydrogel heating was done by varying the oven temperature during conventional heating. As seen in Figure 31**,** when starting at the same initial Q of 12, a hydrogel at a higher oven temperature had a faster deswelling process. The time for half of the water to leave the hydrogel (the point at which the swelling is reduced to a Q of 6) dropped from 1.8 hours at 33 °C to 0.5 hours at 65 °C. This was an expected response that would be present with bulk water as well.

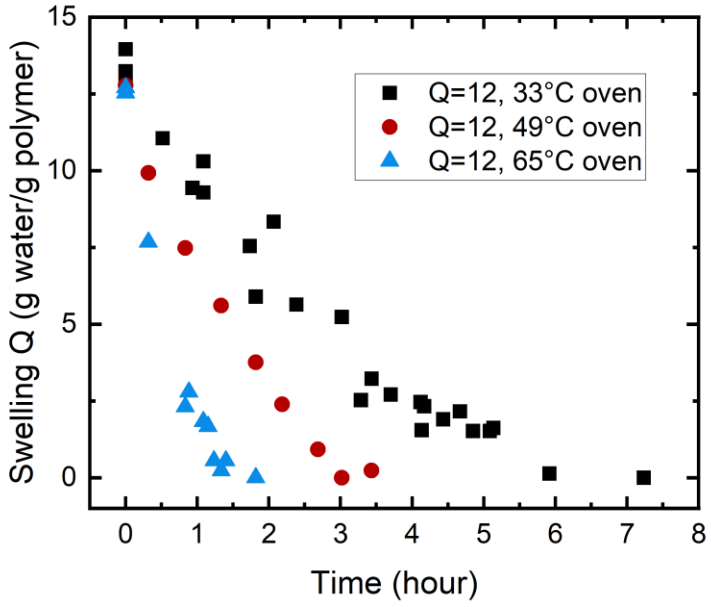

Figure 31: Swelling over time for varying oven temperatures. A warmer oven results in a higher rate of water evaporation, which is expected, and indicates the hydrogel is not interfering with the deswelling process.

In the photothermal case, the temperature was raised by increasing the concentration of nanoparticles with respect to both the polymer and water. Figure 32a shows the temperature over time for both a standard GNP hydrogel and a GNP hydrogel with 4x the extinction of the standard, as well as a MNP hydrogel with 1x, 2x, 8x, 16x the concentration of the standard GNP hydrogel extinction. The increased number of heaters increased both the average temperature and the maximum possible temperature at the end of the photothermal deswelling process. For gold nanoparticle hydrogels, a four times increase of the concentration in the hydrogel decreased the time to remove 50% of the water (Figure 32b) from 1.5 to 1.1 hours (a 26% decrease). Similarly, four times increase in the concentration of the MNPs resulted in a decrease in time to remove half of the water from 2.7 to 1.9 hours (a 30% decrease). The similarity of percent improvement in water output for the same concentration change suggests a similarity in the deswelling process from photothermal heating, regardless of the type of nanoparticle.

As a rough consideration of energy within the hydrogel system, an Arrhenius equation will be used. The Arrhenius equation traditionally describes the energy barrier required to complete a

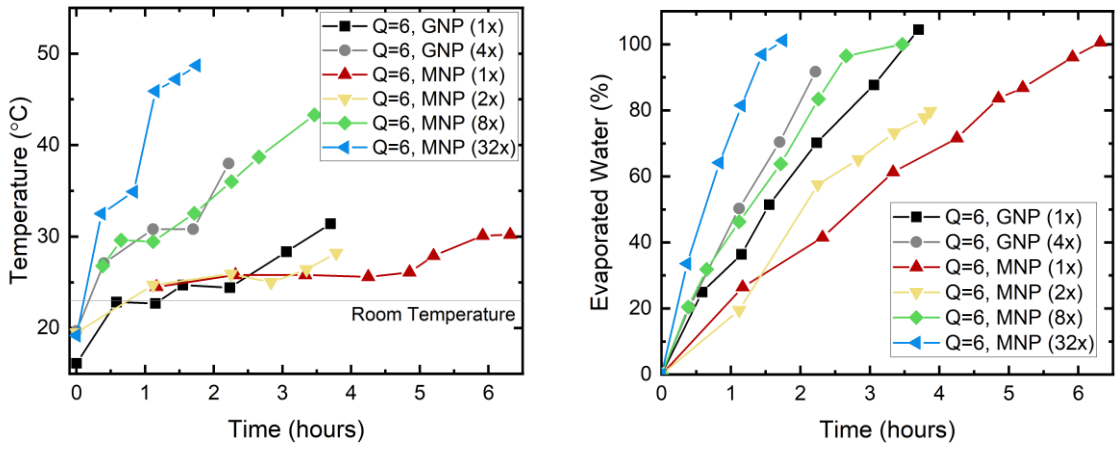

Figure 32: a) Temperature of and b) water evaporated from the hydrogel versus time during photothermal treatment with variable quantities of particles. More nanoparticles increased the temperature and consequently increased the water output at a given time.

chemical reaction [189], however, it can be expanded to model much more [190], including the behavior of water [191–195]. The general Arrhenius equation is

$$k = Ae^{-E_a/RT}. \tag{8}$$

In this work, k is the rate of water evaporation (s^{-1}), R is the universal gas constant (8.314 $J\,mol^{-1}\,K^{-1}$), A is an experimental prefactor (s^{-1}), T is the temperature in Kelvin, and E_a is the activation energy required to remove water from the hydrogel (J). The rate k is calculated from the slope of the fraction of water evaporated over time presented earlier (Figure 25a), though the rate excludes any data points where the hydrogel lost more than 96% of its starting water. This equation can be solved in the form of a linear equation:

$$ln\left(\frac{k}{A}\right) = -\frac{E_a}{R}\left(\frac{1}{T}\right) \tag{9}$$

such that when the $ln\left(\frac{k}{A}\right)$ and inverse temperature is plotted (as in Figure 33), the activation energy is calculated from the slope of the line. The prefactor A is estimated as 10^{13} s^{-1} [194,196]. Using the data presented in Figure 33**,** the energy to remove water from the hydrogel in the case of the conventional oven heating was calculated to be 31.55 ± 3.4 kJ/mol. This value agrees with past work regarding the energy to rearrange water in a hydrogel [159,187] and the general energy required to vaporize water of 40.7 kJ/mol.

With this energy in mind, the GNP and MNP photothermally treated deswelling data can undergo a similar treatment. Because of the temperature variation during the deswelling process, this analysis will not be suited to a discussion about the contribution of the photothermal heating process, but rather a means to consider the theoretical heat requirements that drive the deswelling process at the rates that were measured. As suggested previously, the increasing bulk temperature

may be a means to estimate the local temperature, which may be the primary driver of the deswelling process.

To test this, the GNP and MNP samples were plotted with average temperature over the entire deswelling process. Figure 33 indicates that the GNP and MNP deswelling processes require a notably different energy than the oven requires (activation energies of 52.6 ± 11.9 kJ/mol and 74.8 ± 6.5 kJ/mol, respectively). This is not particularly surprising, as the average temperature is (1) a high-error estimation of the temperature in this process and thus not well described by the Arrhenius relationship and (2) likely not the driver of the deswelling process.

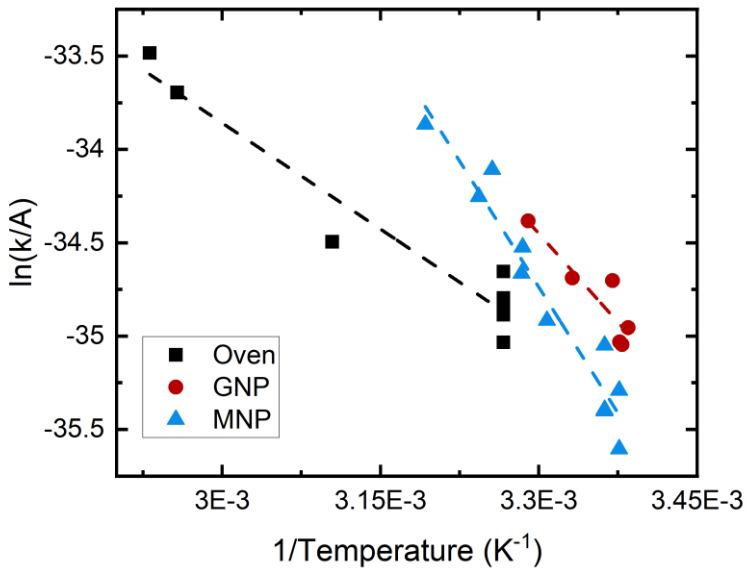

Figure 33: The natural log of the rate vs inverse temperature of conventionally and photothermally heated cases, using the average measured temperature during photothermal heating. Linear fits allow for the calculation of activation energy for removing water from the hydrogels. E_a is calculated to be 31.5 ± 3.4 kJ/mol, 52.6 ± 11.9 kJ/mol, 74.8 ± 6.5 kJ/mol for oven, GNP photothermal heating, and MNP photothermal heating, respectively.

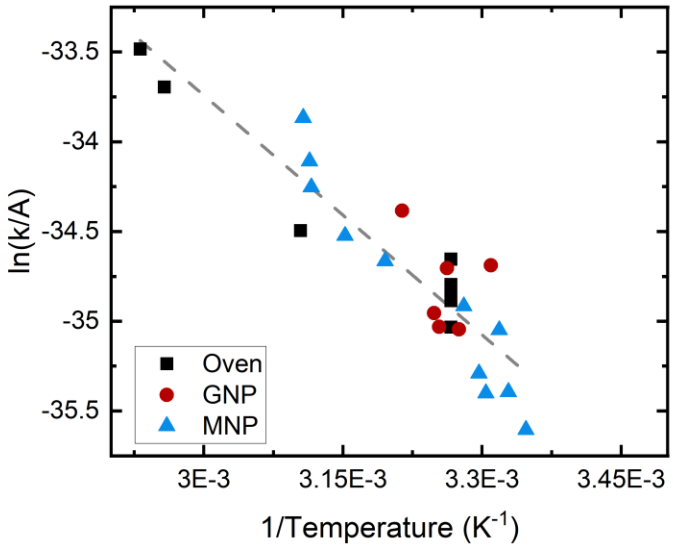

Figure 34: Natural log of the rate versus inverse temperature of conventionally and photothermally treated hydrogels, now with the maximum recorded temperature from the photothermally heated samples. E_a for dotted line (all samples) is 37.0 ± 0.2 kJ/mol

If the local temperature is indeed the driver of the photothermal deswelling process, rather than plotting the rates with average temperature across the deswelling time, plotting with the final temperature of the hydrogel – which may be an approximation of the local temperature near the nanoparticles – should result in a similar plot for the oven and photothermal data. Figure 34 does this, and the alignment of the data supports the hypothesis that the local temperature is the more critical temperature in describing the hydrogel system.

As a reminder, the estimation of local temperatures estimate using final bulk temperature comes from the decreasing volume of the hydrogel moves the particles closer together, reducing the number of "cool" regions in the hydrogel and raising the overall temperature to be closer to the local temperature (Figure 26a, Figure 26b). This may be particularly true in the case of the MNP. As an example, two MNP samples used previously had a volume percent of 4.8% (2x) and 10.5% (16x) MNP to polymer. This corresponds to a distance between nanoparticles in a fully

dried hydrogel of approximately 290 nm and 160 nm, respectively. The spacing is therefore on the scale of the diameter of the nanoparticle itself (78 nm). In contrast, the GNP hydrogels had a volume percent of 1.6E-5% and distance between particles of approximately 5900 nm. Thus, the temperature profile of local heating around the MNP is likely to look very different from a nanoparticle with a lot of space, as the local temperature gradients will add together and raise the average temperature much closer to the local temperature (Figure 35). This temperature profile is more complicated within the experimental system used here, due to the mixing of nanoparticle-microhydrogel with microhydrogel to get specific nanoparticle concentrations and thus may impact the deswelling rates and heating in the hydrogel, however, the basic understanding remains and interesting consideration, particularly since both the GNP and MNP hydrogels were tested with this mixed system.

This work has shown that using MNP - a larger, less efficient photothermal particle - is effective for photothermal heating. Creating an equivalent photothermal response to GNP - a very efficient photothermal heater - however, results in changing the local temperature profiles by increasing the number of nanoparticles, likely resulting a less localized heat.

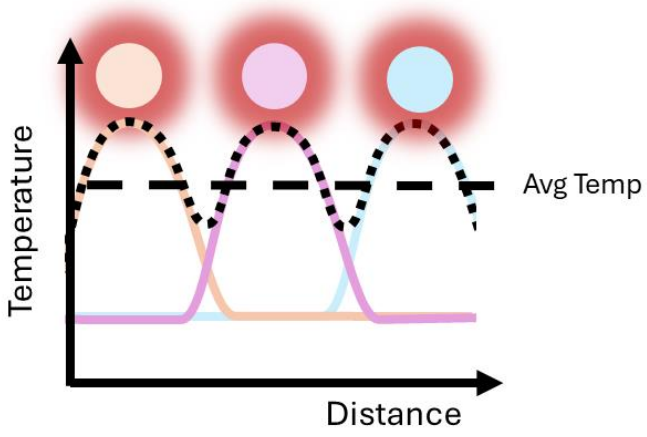

Figure 35: Sketch of the way the temperature profile within the hydrogel may change for close together particles.

Although the temperature may not be particularly localized for the MNP hydrogels, there was still a measurable difference between the photothermal heating and conventional heating. Previously in this work, the rate of water evaporation was calculated across the entire deswelling process (as used in Figure 34). The rate can instead be calculated independently for the first and second halves of the deswelling process to show any changes in how the water deswelling occurs at different points in the process (Figure 36).

Using the average measured temperature during the first and second parts of the deswelling, the rate of deswelling found in Figure 36 was plotted versus average temperature, and the linear fit of this plot was calculated for the two time intervals (Figure 37a). Broadly, the rate of water evaporation decreased for all heating cases (filled data points at a given temperature are generally higher than the unfilled data points marking the second half of the deswelling at the same temperature), though the oven case has a much wider spread between the rates than the photothermally heated cases do. To quantify this spread, the percentage difference between rates

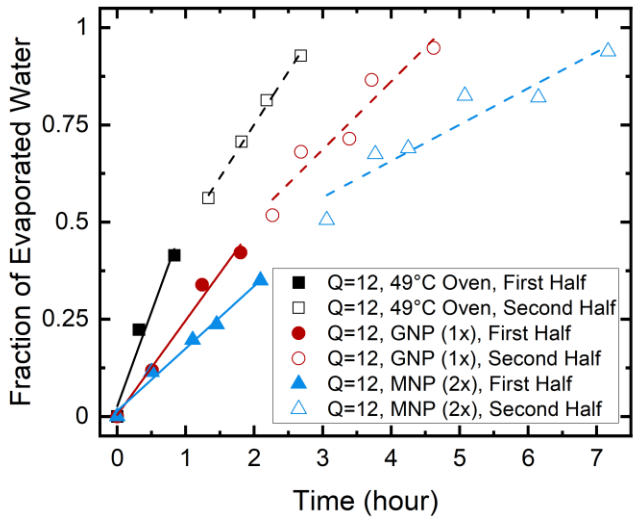

Figure 36: The percent water evaporated over time for Q=12 cases, with points labeled as either the first half of deswelling (solid shapes) or second half (open shapes). The slope of these regions, when compared to each other for a given heating method, are indicators of changes in the dewatering process.

of the first and second half of deswelling (Figure 37b) was calculated. First, the deswelling rate at a given average temperature ($R(T)$) for the different heating methods was calculated from the linear fits of Figure 37a. Then, the percentage difference for the rates at a temperature was found using

$$\%\ Difference(T) = \frac{R_{First\ 50\%}(T) - R_{Second\ 50\%}(T)}{R_{First\ 50\%}(T)} * 100\% \quad (10)$$

where $R_{First\ 50\%}(T)$ is the rate in the first half of deswelling and $R_{Second\ 50\%}(T)$ is the rate of the second half of deswelling at a given average temperature. Figure 37b displays the differences between deswelling rates with increasing temperature for the different heating mechanisms**.** As the overall temperature as increased (using different concentrations nanoparticles of hydrogels), both of the photothermal cases displayed a decreasing difference (lines trend towards zero in Figure 37b) between first and second half dewatering; that is, as there were more photothermal heaters within the hydrogel to make the average temperature larger, the rate of water evaporation became more stable throughout the entire deswelling process, such that the difference between the first and

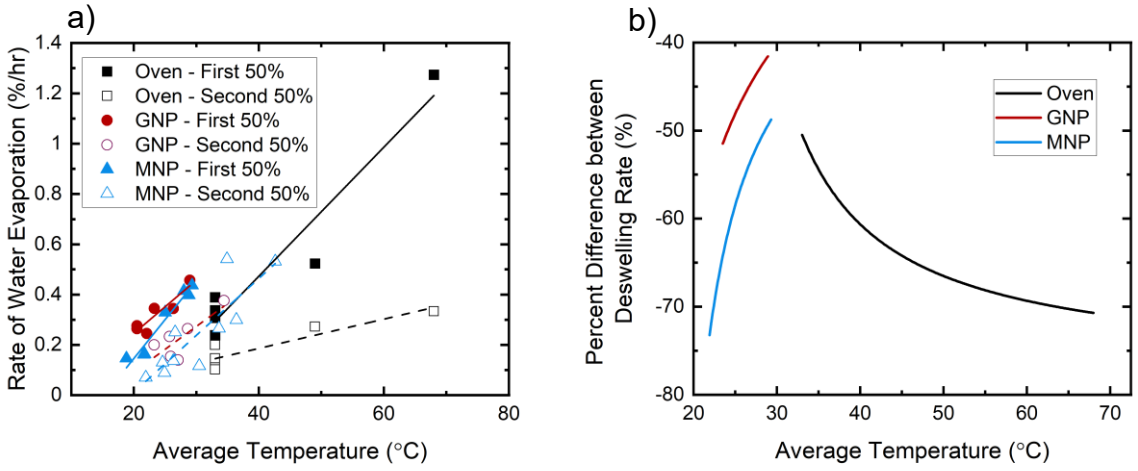

Figure 37: The a) rate of water evaporation versus the average temperature during the period of deswelling. A linear fit of a) was used to calculate the b) percent difference of the rate of deswelling at a given temperature. Data from the first time interval is presented as solid shapes, while the second interval is presented with open markers.

second half of deswelling was reduced. The opposite is true for the oven case- as the temperature increased, the rates between the first and second half of deswelling became more different (larger negative percent difference).

There are two potential sources for the difference in the rate of water loss. Firstly, as discussed in Section 3.4.1, removing the last water of the system is the most challenging, as this is the water most closely bonded with the hydrogel. This explains why the overall rate for all samples is lower for the second half of the deswelling process. However, the photothermal cases also have a self-correcting loop that aids in keeping the rate constant, as the temperature increases by about 15% between the first and second half of deswelling. While water may be more challenging to remove, the overall system temperature increases and provides more energy to that water, mitigating the difficulty in removing the closely bonded water.

Secondly, the hydrogel in the oven may be experiencing a case hardening effect. In an oven, heat moves from the outside of an object inwards, such that the polymer on the surface of

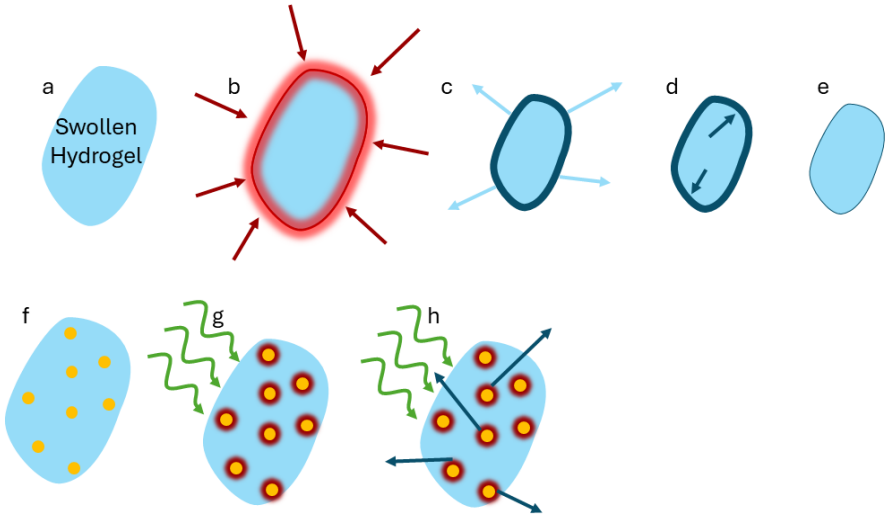

Figure 38: Diagram of the case hardening effect in an oven heated hydrogel and photothermally heated hydrogel. In an oven, a hydrogel (a) is exposed to heat (b). Water from the edges is removed (c), creating a hydrophobic shell (d) until the hydrogel cools or otherwise reswells (e) In contrast, a hydrogel with nanoparticles (f) has heat throughout the system (g), allowing water to exit without the formation of shell on the edge of the polymer (h).

the hydrogel will lose water and become hydrophobic before the center of the hydrogel. This creates a hard, hydrophobic shell around a swollen hydrophilic center (as diagrammed in Figure 38a-e). This effect, known as case hardening [158,187,197,198], slows down the water release process, as the interior water must move past the hydrophobic shell. This is particularly relevant to the end of the deswelling process, as that requires water to move through the most already-hydrophobic hydrogel regions. Although the composite hydrogel used in this work does not have a sharp LCST response, at a high enough temperature, there may still be a case hardening effect, as indicated by the increased difference between the beginning and end of deswelling in Figure 37b.

In contrast, the localized heating of nanoparticles within hydrogels mitigates the impact of case hardening, which is why the GNP and MNP trend the opposite way in Figure 37b. During photothermal heating, the water is heated throughout the sample the entire time, which creates hydrophobic pockets around the nanoparticles instead of on the hydrogel surface (as diagrammed in Figure 38f-h). Water is thus able to continuously leave the hydrogel without the slowdown from case hardening, making photothermal heating an effective option for ensuring all water is recovered.

3.5: Conclusions and next steps

In conclusion, this work has investigated the deswelling mechanics of the composite hydrogel SA+NIPAM by comparing traditional oven heating with the photothermal heating of embedded gold and melanin nanoparticles. The photothermal heating of GNPs was able to drive water loss at rates comparable to that of oven heating, while doing so at a lower bulk temperature. Additionally, photothermal heating kept the water output rate more consistent throughout the entire

dewatering process, due to both the increase in heat near the end of deswelling (from the reduced nanoparticle separation) and the lack of case hardening that became apparent in the case of high temperature oven treatment. Both of these outcomes from photothermal heating would improve the water purification process using hydrogels as a draw agent, as all of the water within the hydrogel would be removed efficiently, with the added benefit of a light-based driver of dewatering that could be set up to use sunlight.

MNPs have been shown previously to be an effective photothermal heater, however with a lower conversion efficiency compared to GNPs. This work showed that reaching the same extinction values or temperatures during photothermal heating required significantly more melanin particles than gold particles (on the order of 4000 times more particles, for an 8 times higher extinction). Such a high concentration of melanin particles is expected to change the temperature profile within the hydrogel to be less heterogeneous than what would occur for gold nanoparticle heating. Despite this, the MNP still resulted in an interior heating that, like the GNP, was able to deswelling hydrogels at rates similar to oven treatment without a slowdown at the end of the water loss process.

There are multiple further questions raised by this work to further enhance the capabilities of hydrogels in water purification and the use of melanin nanoparticles as photothermal heaters. In the context of applying hydrogels to water purification, comparing the MNP heating to the GNP heating in a solar simulator may improve the MNP performance, as the MNPs have a broad absorption spectrum (no LSPR like the GNPs). Comparing MNPs to a different broad absorber may also provide interesting insights into the specifics of MNP as a heater, such as how melanin specifically may interact with the polymer system that it is in, since melanin is a free radical scavenger [58,61], but while keeping the direct photothermal capabilities more similar than those

of MNP and GNP. An analysis of the energies within the hydrogel during photothermal deswelling would provide further insight into the role of photothermal heating compared to oven heating. This would require a more calorimetric approach to monitoring the energy, as the Arrhenius equation is not well suited for the changing temperatures of these hydrogels. Regarding the hydrogel composite itself, there are questions about the role that microhydrogels play in the case hardening effect, as a macrogel would be expected to exhibit a more dramatic case hardening. In such an experiment, using just NIPAM as the hydrogel would provide a more clearly defined translation and thus a sharper difference between the hydrophobic and hydrophilic states. This supplementary work would complement and further describe case hardening seen here, as well as the ability for photothermal heating to minimize the effects of case hardening.

Chapter 4: Degradation of PVA and Melanin Nanoparticles under Photothermal Heating

4.1: Melanin Nanoparticles and Polymer Degradation

Chapter 3 studied melanin nanoparticles (MNPs) in the application of a water purification system and focused on replicating the photothermal response of gold nanoparticles (GNPs). This happened in a biologically similar environment; that is, the MNPs were able to dissipate energy into the water-based environment during the photothermal process, analogous to the environment in which melanin naturally occurs. Placing the MNP in a water-lacking environment may change the heating capabilities or stability of the particles. To look more closely at the fundamental science behind and capabilities of the photothermal heating of MNPs, this section will explore the heating of MNPs in a water-lacking environment, specifically in the polymer poly(vinyl alcohol) (PVA).

In order to examine the heating of MNP in PVA, the low-temperature, fundamental degradation properties from both traditional and photothermal heating of PVA will be presented. The bulk degradation properties of a polymer matrix after photothermal heating have been shown to provide insights into the temperature profile around the particle [91]. This became of particular interest in 2016, when a polymer-independent method of tracking the progress of polymer degradation was proposed [199]. By taking a luminescence measurement of a polymer after thermal treatment, researchers found that regardless of the polymer type or innate luminescence, degrading polymers would luminesce at varying degrees during different stages of degradation. This degradation-based luminescence has distinct characteristics, including being depolarized from the excitation light (such that the emission polarization would not match the excitation polarization) and having a peak location that depends on the excitation wavelength. Eventually, the degradation luminescence decreases and disappears as the optically-active species created during the degradation breaks down with continued thermal treatment. Similar luminescence was

observed from multiple polymers and is hypothesized to be a general property of polymer degradation [92,199–201].

There are several other bulk properties – including mass, absorption, and chemical composition – that can also be used to track changes to the polymer as a result of heating, as this often leads to either solvent loss or polymer degradation. By tracking these quantities, a more complete understanding of the polymer response to heat can be developed. In particular, the reactions and byproducts occurring during thermal polymer degradation may change when driven by conventional versus photothermal heating [91]. Thus, the goal of this work is to investigate the change in mass, optical properties, and chemical composition of a polymer undergoing degradation from both traditional and photothermal heating, and using that to better understand the photothermal capabilities of MNPs.

PVA is a semicrystalline, water soluble, and biodegradable polymer [202–205]. As one of the most widely used polymers, it has been studied in the context of coatings and adhesives [206], stabilizing nanoparticles, drug delivery systems [207,208], and films [209,210]. GNPs and MNPs readily disperse in the polymer without additional modifications. The degradation of PVA has been previously reported [211–214], but past work relied on higher temperatures (generally above 200 °C, as this is near the $T_m$of PVA at 200 °C) than of interest here. Typically, these low temperatures (~100 °C) are used for annealing the samples. However, this annealing process may still modify the polymer properties, depending on the temperature and time of the annealing. Furthermore, the low temperatures studied here are more likely to be encountered by the PVA in real-world applications and thus an understanding of how the PVA responds is important in ensuring the usability of the polymer in a given situation.

This work explores the low temperature degradation of PVA while utilizing bulk polymer changes to compare the photothermal heating of nanoparticles to conventional heating. PVA was degraded conventionally (uniform heating in the oven) and through photothermal heating of gold and melanin nanoparticles. Throughout the process, material characteristics, such as the absorption, luminescence, and chemical composition, were tracked and compared between the different heating mechanisms. In addition, it is proposed that the MNPs undergo a similar universal degradation process, resulting in modified photothermal particles as the MNPs transform into a carbonaceous product.

4.2: Materials and Methods

The same nanoparticles reported in Section 3.2.1 are used here for the PVA samples. Once again, MNPs were used immediately after making them to prevent aggregation. Granular PVA (molecular weight of 95,000 g mol^{-1}) was purchased from Scientific Polymer Products Inc. and used as received. Sample fabrication began with a 10 wt% PVA:deionized water solution that was gently stirred while heated to 85 °C (VWR 325 hotplate/stirrer) to fully dissolve the PVA without the addition of significant bubbles. Nanoparticles were then added in the desired concentration, and 1000 µL of the solution was dropcast onto 2.2 cm x 2.2 cm glass slides. Samples were left to solidify at room temperature overnight. Once dry, samples were removed from the glass coverslips and cut into slices to match the laser illumination region (approximately 2 cm x 0.75 cm). Thickness was measured to be 0.02 cm ± 0.002 cm (The Starrett Co. No. 1230 outside micrometer).

Samples dried at room temperature overnight. Tracking sample mass in ambient conditions over the next two weeks showed both positive and negative fluctuations that were less than 5%. For example, samples were measured after drying at room temperature overnight (Mass 1) and after two additional weeks of sitting at room temperature (Mass 2). Mass 2 was measured to be

94.7% (± 0.48%) of Mass 1. However, this drying process stabilized, and after an additional five days at room temperature, the samples did not lose any further mass (98.48% ± 1.32% of Mass 2). Thus, although the samples did not undergo an annealing process typical in other sample preparation methods, they did reach a stable or cured state before the treatment process.

The GNP/PVA samples had a final concentration of 0.74 nanomolars (nM) (extinction value of 6.6×10^{10} M^{-1} cm^{-1} [8,9,15]), corresponding to a particle spacing of 1.6 μm. As in Chapter 3, the GNPs consisted of 80% spheres (diameter 44 ± 23 nm), 14% triangles (height of 113 nm ± 65 nm), and 6% rods with an aspect ratio of 3.5 (102 nm ± 58 nm by 29 nm ±14 nm). The MNP concentration was chosen to result in a similar to the extinction as the GNPs, such that the 0.02 cm thick samples had measured extinction values of 1.4 and 1.0, for the MNP and GNP samples respectively. The final MNP samples had a concentration of 136 nM (extinction of 4.85×10^{8} M^{-1} cm^{-1}, which is based on particle counting in TEM images and absorption measurements of the PVA samples, and which is consistent with previously reported MNP extinction values [66,67,70,71]), corresponding to a particle spacing of 0.3 μm for the 78 nm ± 25 nm diameter MNPs.

For oven treatment, PVA samples were held at a constant temperature (110 °C to 185 °C, Watlow SD Temperature Controller) for times ranging from 15 minutes to several weeks. The PVA rested on a clean glass petri dish during the oven treatment. Samples that curled during the treatment process were gently flattened immediately after removal from the oven, such that once cooled, samples remained flat. For the case of photothermal heating, the edges of the samples were secured between two glass coverslips (to prevent any warping) before being treated at a laser intensity of 0.6 W/cm^2 (0.5 W, 520 nm laser) for 1 to 70 hours. If samples curled during photothermal heating, some regions would no longer have full exposure to the laser (as some

sections of the sample would end up shadowed). However, excessive contact with glass surfaces could lead to heat exiting the polymer, disrupting the treatment process. This is why only the edges of the sample were secured in order to balance these factors. Measurements of the PVA were taken from the center of the sample, which was not in contact with the glass. Bulk temperatures during treatment were measured by placing a K-type thermocouple (RisePro Thermocouple) on the surface of the samples, in the center of the treatment region.

At regular time intervals during thermal treatment (for example, every hour for the highest treatment temperatures), the samples were removed from heat and allowed to cool, before then being tested for signs of degradation, including changes in the mass (Ohaus Pioneer Balance, 0.001 g), absorption (Agilent Technologies Cary 60 UV-Visible Spectrometer), chemical composition (Agilent Technologies Cary 630 Fourier Transform Infrared (FTIR) Spectrometer), and light emission (PTI QuantaMaster 40 Spectrofluorometer). Data from these measurements were used to characterize the rate and mechanisms of the PVA degradation from heating.

As suggested earlier, a notable signifier of polymer degradation is luminescence. The specifics of measuring this property, and the steps taken to remove machine bias, will now be described.

For the luminescence measurements, the excitation wavelength was selected to be 305 nm, with a corresponding notch filter to block any source leakage. This wavelength has been reported previously to excite the innate luminescence of PVA [215–218]. The luminescence emission from the polymer at that excitation wavelength was measured from 340 nm to 900 nm, with a 370 nm long pass filter to block the excitation beam that may have been reflecting off the sample. The intensity of the source was recorded throughout all measurements and the emission normalized accordingly, allowing for the comparison of emission signals despite any fluctuations in the light

source. General luminescence trends are shown with emission polarization at the magic angle (54.7°), which removes the polarization dependence that may come from the sample's reflections [219].

The polarization dependence of the emitted light was also considered. The degradation-based luminescence is depolarized relative to the excitation polarization, such that the emission from degradation will not match the polarization of the excitation light. This occurs because during the degradation of polymers, many two-level energy systems are formed. Photons are emitted and reabsorbed between these interacting systems, which can subsequently change the polarization of the eventually emitted light. This has been confirmed with multiple polymers and is considered to be a general property of polymer degradation [92,199–201]. Monitoring the polarization dependence in addition to the general luminescence intensity and wavelength (which are other indicators of degradation, as described in Chapter 4.1) thus provides additional confirmation about the degradation state of the polymer.

The luminescence polarization dependence is described with the r-factor [220]. Physically, the r-factor indicates the degree to which the emission and excitation are aligned in polarization. A larger r-factor (approaching 0.4) occurs when the linear excitation and emission polarizations are similar, while a smaller r-factor (approaching -0.2) indicates that the excitation and emission beams have perpendicular polarizations. Therefore, the expected depolarization of the luminescence during degradation should appear as a decreasing r-factor. Mathematically, the r-factor is defined as the relationship between the perpendicular and parallel components of the luminescence emission, in reference to the excitation polarization:

$$r = \frac{I_{VV} - GI_{VH}}{I_{VV} + 2GI_{VH}} \tag{11}$$

where I_{VV} is the intensity parallel to the excitation (vertical excitation-vertical emission polarization), I_{VH} is the intensity perpendicular to the excitation (vertical excitation-horizontal emission polarization), and G is the grating factor, which will be described in greater detail shortly.

During the luminescence measurement, treated samples were excited with vertical polarization, and either the vertical or horizontal polarization of the emission was blocked from the detector with a polarizer. This measurement was repeated with the opposite emission polarization so that the r-factor could be calculated at each stage of thermal treatment.

The calculation of the r-factor requires the grating factor (or G-factor), which quantifies and corrects for innate system polarization bias [219,220]. To measure the grating factor, four fluorophores in dilute solution were measured, such that there was no preferred luminescence polarization direction (due to the fluorophore's random orientations and ability to reorient between excitation and emission in solution) and thus depolarized luminescence. Perylene was dissolved in methanol (8.6×10^{-6} M), while Lumogen F Yellow 083 (2.3×10^{-6} M), Lumogen F Orange 240 (1.65×10^{-6} M), and Lumogen F Rot 305 (4.36×10^{-6} M) were dissolved in DMF (Figure 39a). Each

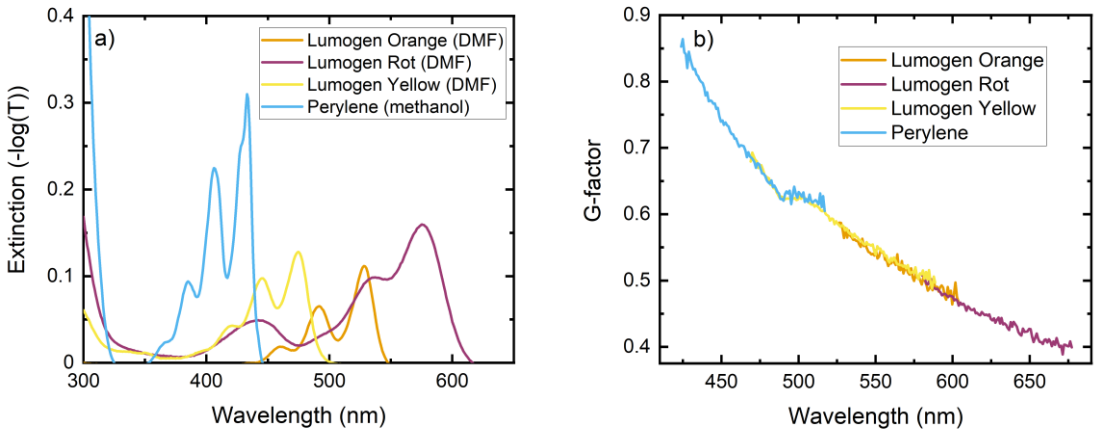

Figure 39: a) Absorption of the four fluorophores in solution used to measure and calculate b) the G-factor. The G-factor is a wavelength-dependent intensity correction used in the calculation of the r-factor.

solution was excited with horizontal polarization at the appropriate wavelength for that fluorophore, and the vertical and horizontal emission were measured. The G-factor was then calculated using the ratio:

$$G = \frac{I_{HV}}{I_{HH}} \tag{12}$$

Using multiple fluorophores with different emission profiles and averaging the results generated a G-factor that spans a longer wavelength range. The final G-factor (the average at each wavelength of Figure 39b) was applied to each wavelength used in the r-factor calculation described above. The wavelength range of the r-factor is thus restricted by the range over which the G-factor has been defined.

4.3: Results

With the samples and characterization methods selected, samples were treated and measured. This section will present the results and describe the internal processes which occurred during both conventional oven treatment and photothermal treatment of GNPs and MNPs. The changes in mass and absorption will first be described, followed by the luminescence of the samples and the indicators of the universal degradation luminescence. The chemical changes and degradation products will be described next, followed by the way those chemical changes modified the PVA solubility. These combined techniques work to accurately present the low-temperature degradation of PVA and describe the photothermal response of MNPs in a water-lacking environment.

First, the general degradation characteristics expected from PVA will be briefly described [211–214,221]. PVA is typically made from poly(vinyl acetate) (PVAc), and thus the first step in the degradation process is the removal of residual PVAc and water (the solvent) [214].

From there, PVA experiences mass loss and breaking of the polymer side chains, forming new chemical crosslinks or radicals [206,211,221], which may also change the crystalline structure [212]. Finally, a range of degradation products may form as the PVA fully breaks down [212]. These physical and optical changes will be described in further detail below.

4.3.1 Absorption, Mass, and Temperature

Perhaps the most obvious indicator of polymer degradation is the discoloring (yellowing) of the polymer after thermal treatment. Figure 40 shows a photo of PVA samples after treatment in a 145 °C oven for variable amounts of time, where there is a clear change from a transparent polymer at 0 hours to a brown sample at 69 hours. This color change is quantified for the oven-treated samples in Figure 41, which shows the initially transparent PVA forming an absorption wall centered around 480 nm with thermal treatment. The yellowing of PVA has been suggested to come from an increase in C=C bonds [206] that form as a degradation byproduct. Double carbon bonds are a common polymer degradation product often attributed to aromatic rings, and are thus a good indicator of the degradation progress. This wall appears to stabilize at a specific treatment time dependent on the treatment temperature (46 hours for the 145 °C, and 1 hr for the 183 °C case due to the difference in temperature and thermal stability of PVA). This may suggest an upper

Figure 40: PVA sample treated at 145 °C for 0 hour to 69 hours. With treatment, the sample yellows and eventually browns.

limit to the degradation process at these temperatures. At the lowest oven temperature used (110 °C), only a slight discoloration is present after nearly 3.5 weeks of thermal treatment. This suggests that an annealing temperature near or below 110 °C will not significantly change the polymer.

Photothermally-treated samples also experienced quick discoloring, indicating a similar thermal response as in the oven-treated samples. The absorption of the GNP-PVA samples included the GNP peak at 555 nm (Figure 42a). With photothermal treatment (which resulted in sample temperatures from 100 °C - 123 °C), there is a visual yellowing of the sample and the formation of the absorption wall. However, compared to the oven-treated samples, the absorption wall stayed at a lower wavelength (415 nm) for photothermal treatment ranging from 1.5 to 12

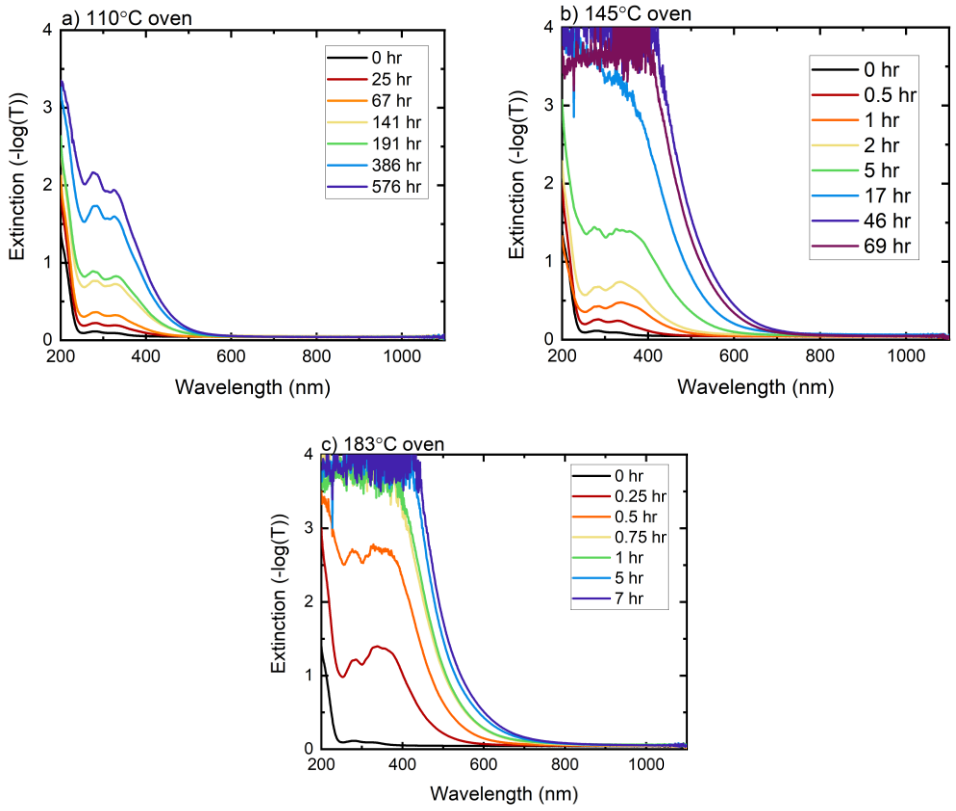

Figure 41: Absorption spectra of PVA treated in an oven at a) 110 °C, b) 145 °C, and c) 183 °C for variable amounts of time, as determined by the treatment temperature. The visual yellowing of the sample is represented by the formation of an absorption wall centered at 480 nm. Noisy signal near an extinction of 4 indicates a maximum measurement of the equipment

hours, suggesting fewer C=C bonds (again, an indicator of degradation products) form than in the oven case.

Similarly, MNP-PVA samples included the broad absorption of the MNPs (Figure 42b). After photothermal treatment that measured temperatures from 105 °C - 125 °C, a wide wall formed on top of the MNP signal. While continued treatment did result in an absorption wall that shifted slightly in wavelength, the impact was not as extreme as in the oven-treated case.

The mass was also tracked throughout treatment, however, the samples never experienced degradation related mass loss. The primary mass loss occurred entirely during the first time a sample was thermally treated, the length of which varied from 0.25 to 25 hours, depending on the temperature and treatment type. This suggests the mass difference is primarily a loss of solvent (as there was no annealing step of the sample preparation), which is water in these samples. These results are displayed in Table 4. All oven-treated samples regardless of treatment temperature experienced an initial percent mass loss (mass loss after the first treatment of a sample, where treatment time depends on the temperature) of around 10.0% (± 3.3%) (Table 4, column d), and

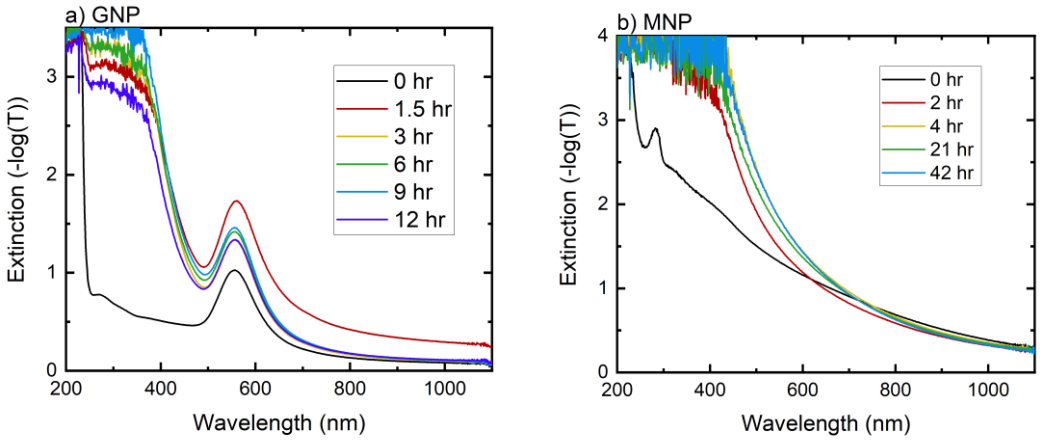

Figure 42: Absorption spectra of a) GNP and b) MNP. Both spectra include characteristic signals from the nanoparticles - a 555 nm peak from the GNP, and a broad absorption signal from the MNP (250 nm – 1100 nm). Noisy signal near an extinction of 4 indicates a maximum measurement of the equipment.

Table 4: Mass loss of PVA exposed to different treatment times, temperatures, and methods.

a) Treatment Method	b) Time (hr)	c) % of initial mass	d) Change from starting mass (%)	e) Change from annealed mass (%)
110 °C Oven	25	86%	-14.38%	
	68	89%		3.48%
	141	90%		5.38%
	191	88%		3.23%
145 °C Oven	0.5	94%	-6.27%	
	5	95%		1.44%
	17	94%		0.38%
	46	93%		-0.60%
	69	91%		-2.54%
183 °C Oven	0.25	91%	-9.38%	
	0.5	94%		3.23%
	0.75	94%		3.56%
	1	91%		0.92%
	1.25	94%		4.09%
	1.5	90%		-1.05%
	2	90%		-1.13%
	5	92%		1.02%
Photothermal, GNP (100 °C - 123 °C)	1	93%	-7.27%	
	2	98%		5.21%
Photothermal, MNP (105 °C - 125 °C)	1	89%	-11.22%	
	2	93%		5.20%

then remained constant (within ± 5.5% of the 'post-annealing' sample mass) throughout the increased treatment time (Table 4, column e). The photothermally heated samples, which reached bulk temperatures above the evaporation point of water, experienced similar levels of water loss and then stabilization. Overall, this indicates that photothermal heating of both MNP and GNP was able to anneal the bulk PVA sample to a similar degree as the oven-treated PVA.

Despite these indicators of bulk degradation, the bulk temperature measured during photothermal treatment of both GNP and MNP samples was generally low and near temperatures of the 110 °C oven, although the temperature did increase with time (Figure 43) from around 100 °C to 125 °C.

However, the expression of degradation processes in a relatively short timescale despite the low bulk temperatures of 100 °C to 125 °C suggests that the local temperatures near the particles during photothermal heating are significantly higher than the bulk temperatures. This then indicates that the local temperatures are able to productively drive the degradation to a point that bulk effects are visible. This will be explored further in the other signals of degradation, but is

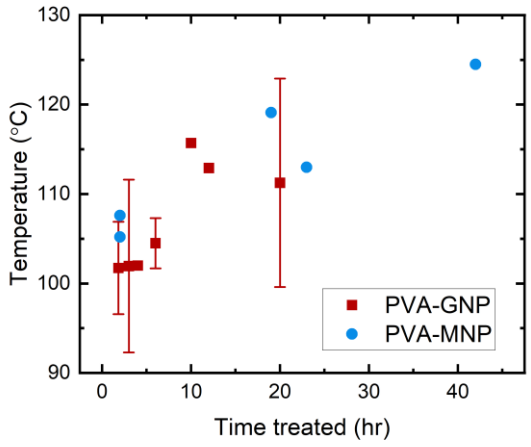

Figure 43: Bulk temperature measured during photothermal treatment for both GNP and MNP. Error bars for PVA-GNP samples are calculated from the standard deviation of temperature measurements across multiple samples at a given time treated.

notable - the nanoparticles are able to produce bulk effects, despite a low bulk temperature. As the 110 °C oven resulted in no noticeable markers of degradation, this suggests the presence of localized, significantly warmer regions around the nanoparticles drive the degradation.

Thus far, absorption spectroscopy has shown a low temperature degradation of PVA, as indicated by the presence of an absorption wall after thermal treatment for both oven and photothermal treatment. The lowest oven temperature test (110 °C) results in minimal discoloring even after 3.5 weeks of thermal treatment. The mass loss indicates an annealing process within the first thermal treatment of all samples, though the stabilizing of the mass afterwards suggests that the temperature was not high enough to degrade the PVA fully (as would be indicated by mass loss [214,221]). These two simple results have shown similarities between GNP and MNP photothermal heating, as both result in the same absorption wall and mass loss, without the significant increase in MNP quantity that was required in Chapter 3. These simple checks for degradation are useful in gauging the polymer state, particularly when matched with the more sophisticated measurements described in the subsequent sections.

4.3.2 Universal Luminescence from Degradation

The attention will now turn to the universal luminescence from polymer degradation, which first requires an understanding of the innate luminescence of the PVA, as this will be present as a background signal.

Typically, luminescence in polymers arises from π-bonds within the molecular structure. PVA does not naturally have π-bonds present, and thus the innate luminescence from PVA has been attributed to the aggregation-induced emission (AIE) [222] from the hydroxyls [215]. According to the AIE understanding, the polymer chains are arranged such that the functional

groups (the hydroxyls, as seen in Figure 44) form electron-dense areas. The hydroxyl groups can be excited by and emit a range of wavelengths, based on the size of the cluster/electron group. However, because the size of the electron group determines the luminescence, that luminescence can be altered by modifications to the polymer structure, such as if water is bonded within the PVA, the water effectively quenches the luminescence signal [216]. Similarly, if a solution of PVA is too dilute to form significant clusters of hydroxyls, the luminescence will have a weak or nonexistent signal. PVA powders or films display significantly stronger luminescence than PVA in solution because of this [215].

The oven-treated PVA samples will be discussed first. For excitation wavelengths near 300 nm, there was an expected luminescence peak at 415 nm [215–218]. This is seen in Figure 45. Looking at the 145 °C treatment, there was an increase in luminescence emission and a wavelength shift to around 450 nm with increasing time. After approximately 5 hours of treatment, the luminescence signal began to decrease, until 46 hours, at which point there were no further changes to the signal. This agrees with the absorption measurement, as the absorption wall similarly stopped changing around this time. For both the 145 °C and 183 °C treatment, the end of the luminescence changes result in two distinct peaks - a broad signal at 555 nm, and a small peak at 380 nm. The 380 nm peak is likely still related to the innate PVA luminescence. The 183 °C samples had a smaller remaining innate luminescence. The broad degradation peak at 555 nm agrees with past work on polymer degradation peaks, and is associated with the formation of

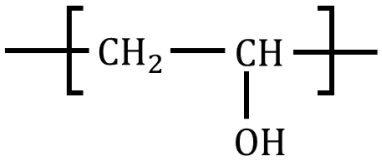

Figure 44: The PVA chemical structure.

carbonyls (C=O) or proto-aromatic rings (including C=C) [199]. In contrast, the 110 °C oven samples only increased in emission.

The two peaks that form in the final stages of treatment for the higher temperature oven cases can be further understood using polarization analysis. As discussed in Chapter 4.2, the r-factor gives a numeric value to the polarization dependence of the emission signal relative to the excitation beam's linear polarization direction. When the r-factor is high, the polarization of the emission is predominately along the same direction as the polarization of the excitation light. As the r-factor decreases, the emission signal becomes depolarized with respect to the excitation.

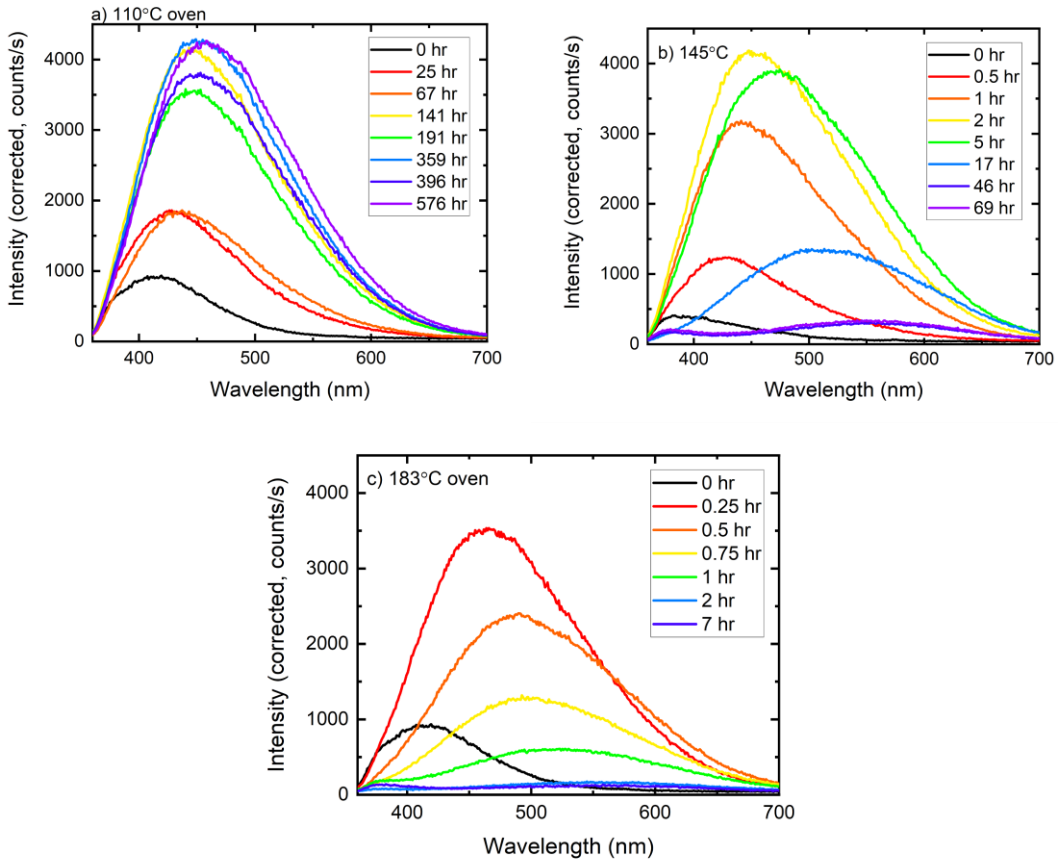

Figure 45: Luminescence measurements for a) 110 °C, b) 145 °C, and c) 183 °C treated PVA samples. The degradation luminescence is associated with a broad increase in luminescence, shift in wavelength, then decrease in luminescence. This is primarily seen in the higher temperature treatments, as the low temperature is not enough to fully degrade the PVA.

Physically, a large r-factor indicates a relatively straightforward excitation and emission pathway within the sample, such as what would be associated with isolated fluorophores in the material. As the polymer degrades, the hypothesis proposed by previous research [92,199] is that there are many isolated two level systems, and luminescence results from many absorption and emission events, which changes both the energy and the polarization of the emission, resulting in a lower r-factor. Therefore, a larger r-factor would indicate luminescence from innate polymer properties, while a low r-factor would indicate luminescence from a more universal degradation process.

The r-factor calculated at both 423 nm (close to the innate luminescence peak) and 555 nm (at the final degradation luminescence peak) for the higher oven treatments is shown in Figure 46. Initially, both 145 °C and 183 °C samples had a high r-factor at the innate luminescence wavelength, as expected. The r-factor then decreased with treatment as the 423 nm signal was overpowered by the universal degradation luminescence, but returned with the separation of the two final peaks seen in Figure 45, particularly for Figure 45b and Figure 45c. The 555 nm signal

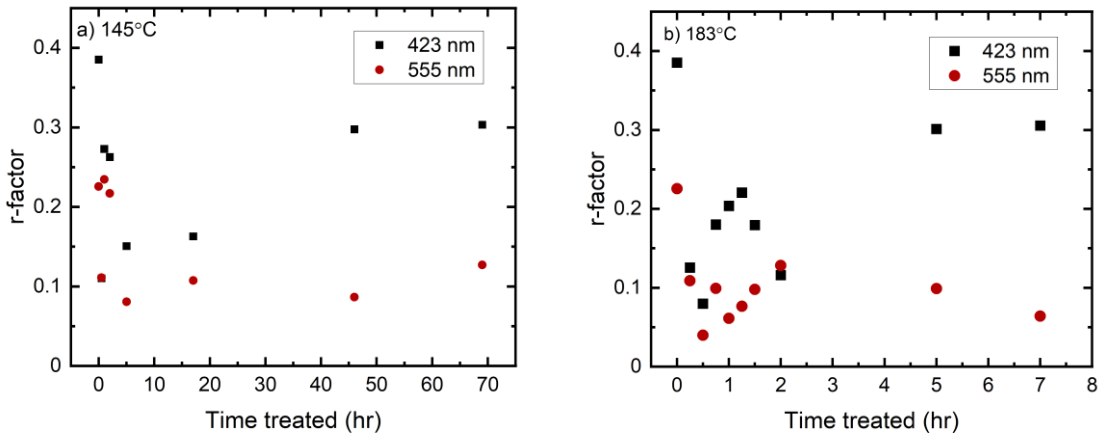

Figure 46: R-factor for the a) 145 °C and b) 183 °C oven treated PVA at both 423 nm (near the innate luminescence) and 555 nm (the final location of the degradation luminescence). For each data point, the intensity of the luminescence signal was extracted at the appropriate wavelength and used in Equation 11. Although the 183 °C oven was measured at longer treatment times, the signal was below the background noise level of the equipment for one of the polarization components, and thus unsuitable for an r-factor calculation.

begins at a somewhat high r-factor, which is likely due to the low signal intensity at the beginning of treatment, and moves to lower r-factor values with treatment, confirming that this peak is from the degradation.

With context from the emission patterns from oven-treated PVA, the photothermal samples will now be similarly described. As before, this must begin with a discussion of the innate luminescence present in the samples.

The GNPs did not exhibit luminescence, and the innate PVA signal was similar to that of PVA without nanoparticles (Figure 47a). In contrast, there is a clear emission signal from the MNPs at 475 nm, overlapping with the innate luminescence of the PVA at 390 nm (Figure 47b). Melanin has been reported to only slightly luminesce until it has been oxidized [223–226], at which point it will have an increasing luminescence signal with increasing oxidation [227]. This oxidation can be done during synthesis (as is done in this work), through light, or through contact with hydrogen peroxide. The melanin luminescence can be excited with many wavelengths [226], including the UV range used to excite the PVA, resulting in a peak around 475 nm.

With photothermal treatment, the GNP samples showcased an increase in luminescence with a shift in wavelength, followed by a decrease in intensity (Figure 47a). The new peak around 475 nm could be a universal luminescence degradation peak, based on the r-factor plotted in Figure 47c**.** The r-factor near the innate luminescence (423 nm) and at the degradation peak (475 nm for the photothermally treated samples) remained similar and relatively low throughout the treatment, likely because of the proximity in wavelength to the degradation peak and thus an overpowering of the degradation signal.

The photothermal heating of MNPs in PVA had a much different response than the GNP in PVA (Figure 47). The emission peak associated with MNPs immediately decreased in intensity

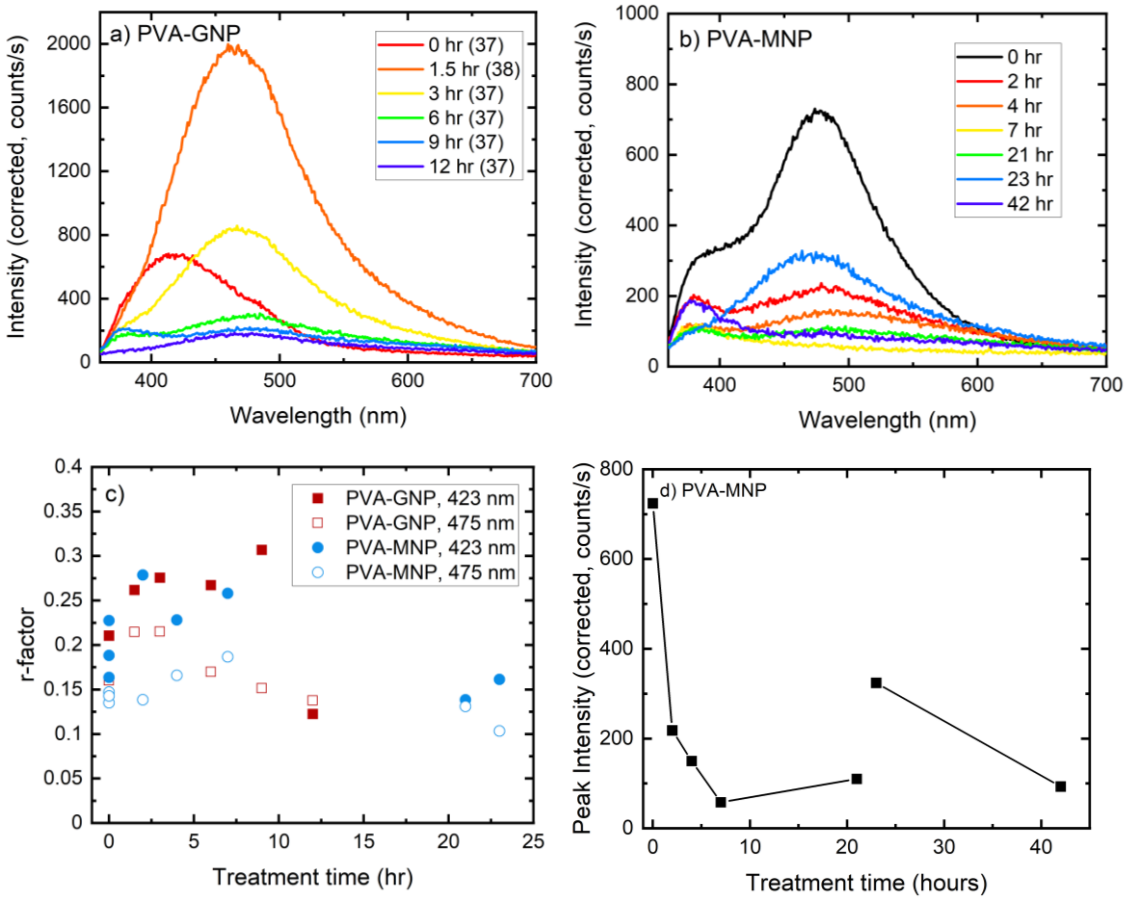

Figure 47: Fluorescence throughout photothermal treatment for a) GNP-PVA and b) MNP-PVA. c) The r-factor of the GNP and MNP treated samples at 475 nm, which is expected to be the degradation peak for photothermal treatment. For each data point, the intensity of the fluorescence signal was extracted at the appropriate wavelength and used in Equation 11. For the 42 hour MNP photothermal treatment, the signal was below the noise level of the machine for one of the polarization components at this wavelength, and thus unsuitable for an r-factor calculation. d) Peak intensity of the PVA-MNP fluorescence. Between 21 and 23 hours of thermal treatment, the peak intensity switches from indicating the MNP (0-21 hours) to indicating the PVA universal degradation fluorescence (23-42 hours).

with photothermal treatment. After seven hours, only the innate luminescence remained, although with a modified shape compared to the PVA with no nanoparticles. With continued treatment, a signal around 475 nm began to grow (visible at 21 and 23 hours), until extended treatment reduced that signal once more, leaving just the innate luminescence of the PVA. Throughout the entire treatment, the signal at 475 nm was relatively depolarized from the excitation wavelength (Figure 47c).

This interesting pattern in the luminescence data of the MNPs in PVA suggests two independent degradation processes, which may be in part due to the free radical scavenging of melanin. It has been shown previously that melanin in PVA will increase the thermal stability, raising the degradation temperature of PVA [221]. PVA degrades via an 'unzipping' of the polymer chains [221,228]. The MNP may scavenge the radicals produced by this process [206,221] and interrupts further degradation. Therefore, it may be that in the first seven hours of treatment, there was no formation of a degradation peak of PVA because the MNPs were interrupting that process.

However, the melanin itself is also a polymer, and thus may be undergoing a universal degradation process during that early treatment, perhaps indicated by the slight shift from 475 nm to 495 nm before a decrease in the luminescence signal. Melanin is known to undergo oxidative degradation when interacting with light, also known as bleaching. This corresponds to a change in the absorption spectrum and a change to the free radical centers [225,229]. As the degraded melanin is no longer able to scavenge free radicals from PVA, the PVA is able to proceed along the same degradation pathway as when photothermally heated with GNPs, considering the similar final emission wavelengths. Although the melanin may be changed, we observe that it can still photothermally heat, perhaps even more effectively than the undegraded MNP, as suggested by the increase in temperature with extended treatment (Figure 43). Despite differences between the two particles, heating from either resulted in PVA emission with a peak wavelength shift that was different from the oven-treated samples. Figure 48 plots the peak luminescence wavelength over normalized treatment time for all heating cases, prioritizing tracking the degradation peak over the innate luminescence. The peak wavelength of the photothermal cases did not shift as far as the oven-treated samples (Figure 48) and stabilized near 475 nm.

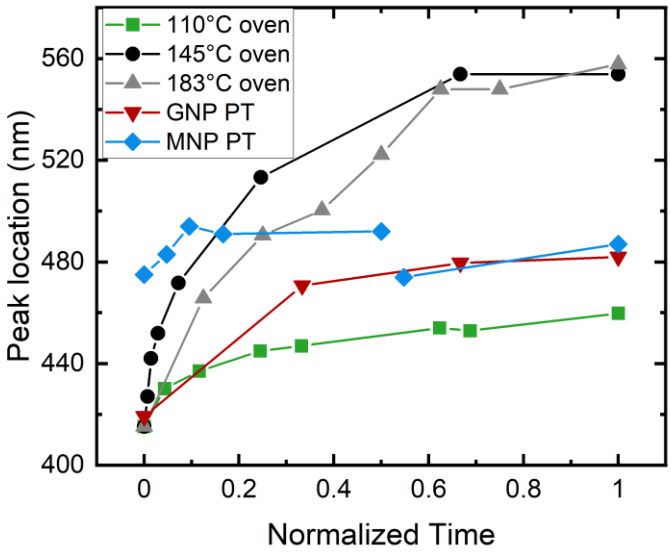

Figure 48: The peak location measured at different treatment times, with preference given for the degradation peak. Peak location is found at the highest intensity value of a smoothed luminescence curve. Time is normalized to the final time the sample was treated to. All samples start at the same innate PVA luminescence wavelength, except for the MNP-PVA samples, as the MNP overpowered the innate PVA luminescence. For the MNP-PVA sample, the first half of the data points correspond to the MNP, while the second half correspond to the PVA degradation luminescence.

4.3.3 Chemical Structure Changes from Thermal Treatment

The information presented so far characterizes the degradation of the PVA, both from oven treatment and photothermal treatment, with indications in the absorption, mass loss, and luminescence of the samples at different stages of the treatment. Several of these signals suggest the presence of C=C or C=O formation. The presence of these bonds and other insights into the changing PVA structure can be found through Fourier Transform Infrared (FTIR) measurements. The changes in structure will then be confirmed with a simple solubility test, as the degraded PVA is expected to become less soluble in water.

The FTIR measurements were taken with a diamond attenuated total reflectance (ATR) sampling tool, with a measuring depth of approximately 2 μm. Therefore, this is functionally a

surface measurement of the approximately 210 μm thick samples. Data was normalized to the transmission value at 1089 cm^{-1}, which is associated with C-O bonds and thus is common in the PVA (Figure 44). Chemical changes are then considered by tracking the relative height of several transmission peaks. This work specifically will look at the crystallinity, C=O, C-O-C, and C=C peaks that experienced the most change from thermal treatment. The crystallinity and C–O-C peaks both give insight into the structural changes occurring within the PVA with treatment, while the C=O and C=C correspond to the degradation products.

The raw FTIR peaks are presented in Figure 49, with notable peaks marked with vertical lines. As before, the signals from the nanoparticles in the PVA must be considered. For the GNP samples, the most notable change from pure PVA was a large peak at 1654 cm^{-1} that disappeared immediately with both photothermal treatments. These nanoparticles were harvested from collapsed CTAB-GNRs, and thus this peak and the small peak at 1387 cm^{-1} can be attributed to aromatic rings that have been previously identified in CTAB-GNRs [230]. Similarly, the C-H bending indicated by the small peak at 840 cm^{-1} is present only when the CTAB is bonded with the GNRs. Finally, the starting crystallinity peak was notably higher, which is discussed more below. The MNP samples did not have any notable peaks compared to pure PVA save for one slight peak increase at 1560 cm^{-1}, which is associated with C=C aromatic rings that are present in MNPs.

As a semicrystalline polymer, PVA exhibits two peaks corresponding to the crystalline (peak located at 1141 cm^{-1}) and amorphous (peak located at 1095 cm^{-1}) C-O structure present in the polymer. The ratio of these two peaks corresponds to the crystallinity, where a higher value of this ratio indicates a more crystalline polymer [231,232].

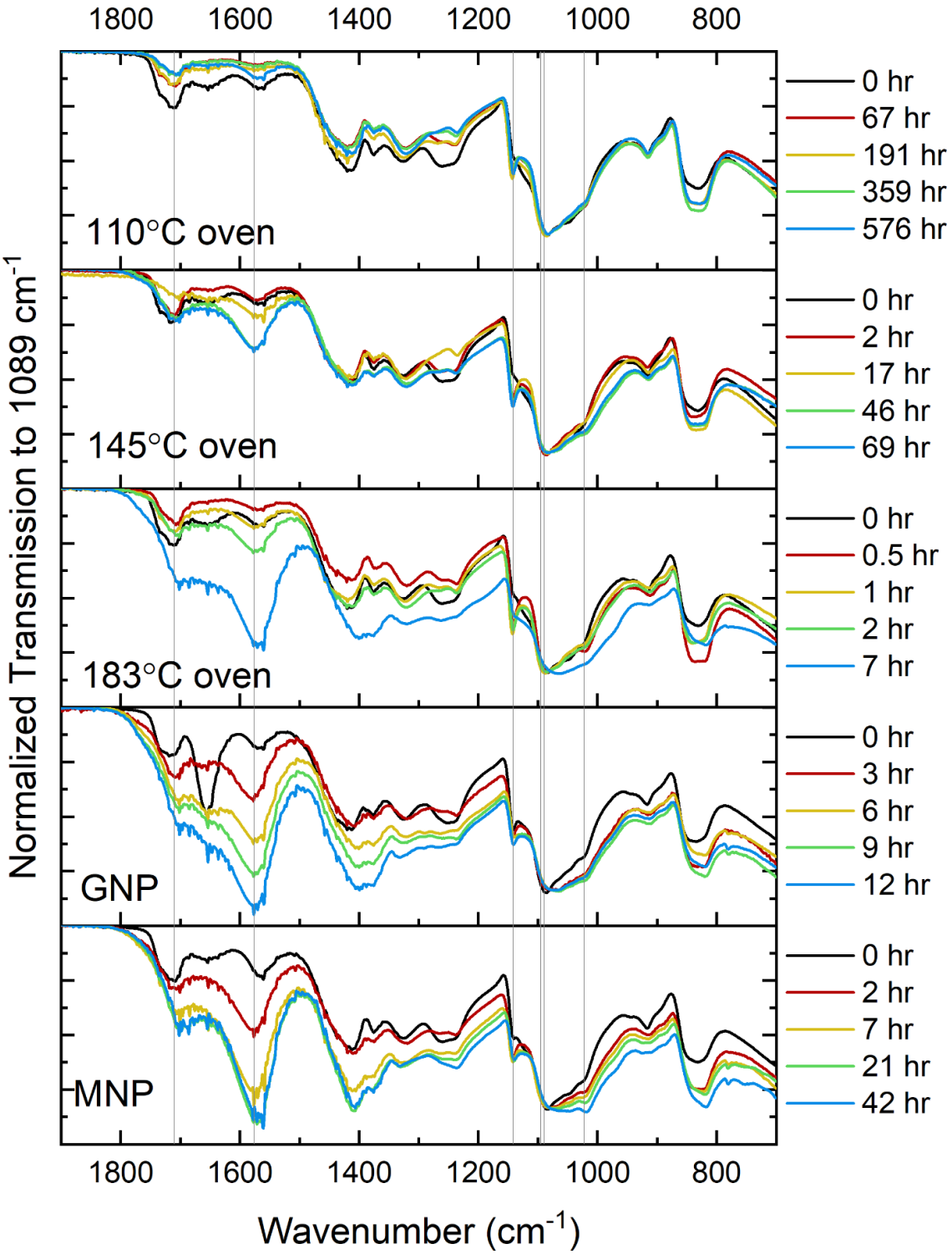

Figure 49: FTIR spectra for all samples. Vertical lines are placed at the notable wavenumbers of (from left to right) 1710,1576, 1141, 1095, 1089, and 1022 cm^{-1}.

The ratio of the crystalline and amorphous peaks is plotted over time normalized to the final treatment (Figure 50). All samples exhibited an initial rise followed by a stabilization, with the 110 °C oven taking more time overall to stabilize. The initial rise in crystallinity suggests an annealing process, where the first thermal treatment adjusts the PVA structure as the solvent is removed [233]. The 110 °C oven sample stabilizes at a lower crystalline/amorphous ratio than the other oven cases or the photothermally treated samples. Both the GNP and MNP samples began with a larger crystallinity ratio than the pure PVA samples (0.66 for nanoparticle samples compared to 0.55 for pure PVA). This is unsurprising, as the nanoparticles can serve as a nucleation site for a crystalline structure. With photothermal treatment, the GNP containing samples stabilized at a ratio of 0.75 ± 0.02, while the MNP containing samples stabilized at 0.73 ± 0.02, which are values comparable to treatment in an 183 °C oven (GNP) and 145 °C oven (MNP).

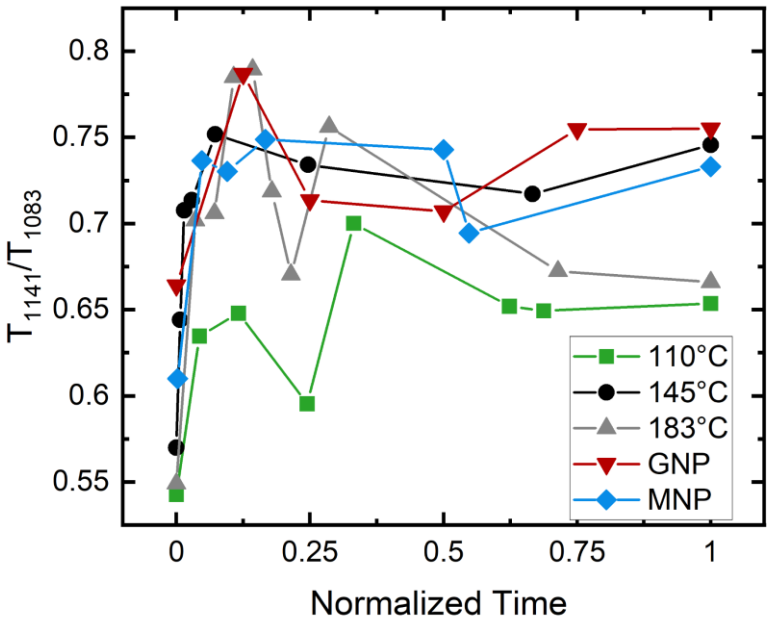

Figure 50: Crystallinity ratio for all thermally treated samples, plotted with time normalized to the end of the treatment process.

The other interesting structure change in the PVA after thermal treatment is apparent in the broadening and shifting of the normalization peak at 1089 cm^{-1} (associated with C-O bonds). Broad peaks in FTIR suggest more complex energy transition possibilities than narrow peaks, which correspond to pure, isolated energy levels. This broadening is much more apparent in both of the photothermal cases.

The broadening of this peak also corresponds to an increase of the 1022 cm^{-1} peak, again particularly for the photothermal cases. This is associated with C-O-C bonds, which may occur during the degradation as radicals are removed from the PVA and the now open bonds form crosslinks with other PVA chains [206,212]. This process is described in Figure 51b.

The attention will now turn to the formation of C=O and C=C, both of which are expected to contribute to the luminescence.

PVA is typically made from poly(vinyl acetate) (PVAc), which naturally includes C=O bonds. Thus, the transmission peak at 1710 cm^{-1} is expected to begin high, then decrease with treatment or annealing as the PVAc is removed from the PVA. This is seen in Figure 52 for the

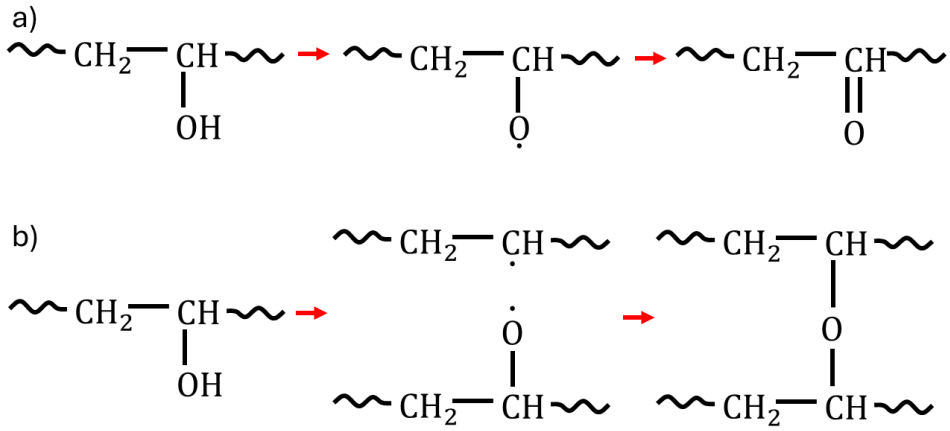

Figure 51: Chemical diagram showing the potential restructuring of bonds with PVA during degradation. a) As energy enters the system, the polymer side group undergoes oxidation (loss of an electron or hydrogen) of the side chains. The radicals are then able to either form C=O bonds or b) C-O-C crosslinking bonds. Based on work by Ref [206,212].

three oven-treated cases. The minimum transmission at this peak occurs at 600, 17, and 0.5 hours for 110 °C, 145 °C, and 183 °C oven temperatures, respectively, though the 110 °C case may continue to decrease with further treatment. After this initial decrease, the 1710 cm^{-1} peak increases again, as new C=O bonds are formed, through oxidation of the polymer side group (Figure 51a) or from the breakdown of the polymer chains into byproducts like ketones and aldehydes [212].

Both photothermal cases show no initial decrease; rather, they show an immediate increase and thus an immediate formation of the degradation products, particularly for the MNP samples. The lack of the PVAc removal signals in the photothermal case suggests one of two possibilities: either the PVAc was removed much faster in the photothermal case, and thus was not visible on the timescales measured; or the PVAc was unable to be removed, and was simply added onto by the degradation products.

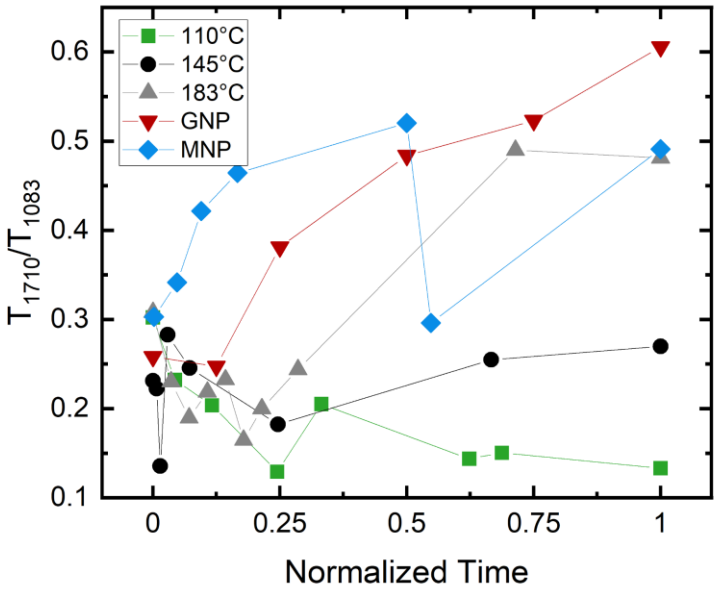

Figure 52: Tracking the C=O peak at 1710 cm^{-1} over normalized time to the end of the treatment process. The photothermal treated cases show an immediate increase in C=O, with the 183C oven treated sample following after an initial decrease indicating a removal of PVAc. The two lower oven temperatures did not ever reach the same final amounts of C=O bonds, as indicated by the comparatively lower ratio values.

The signal at 1576 cm^{-1} was the largest indicator of C=C products (Figure 53), and suggests the presence of aromatic rings. The 110 °C oven did not show a significant peak. However, both the 145 °C and 183 °C oven samples showed a steady increase in the peak size as treatment continued, with the 183 °C growing much more quickly to a higher ratio than the 145 °C oven.

The chemical changes described are consistent with the previous measurements. For example, the innate luminescence of PVA before treatment was larger than the luminescence after (Figure 45 and Figure 47), potentially due to the removal of -OH pendent groups as they turned into C=O (1710 cm^{-1}), or was reshaped into C-O-C bonds (1020 cm^{-1}). The C=O (1710 cm^{-1}) bonds and C=C (1576 cm^{-1}) bonds can both contribute to the universal degradation luminescence.

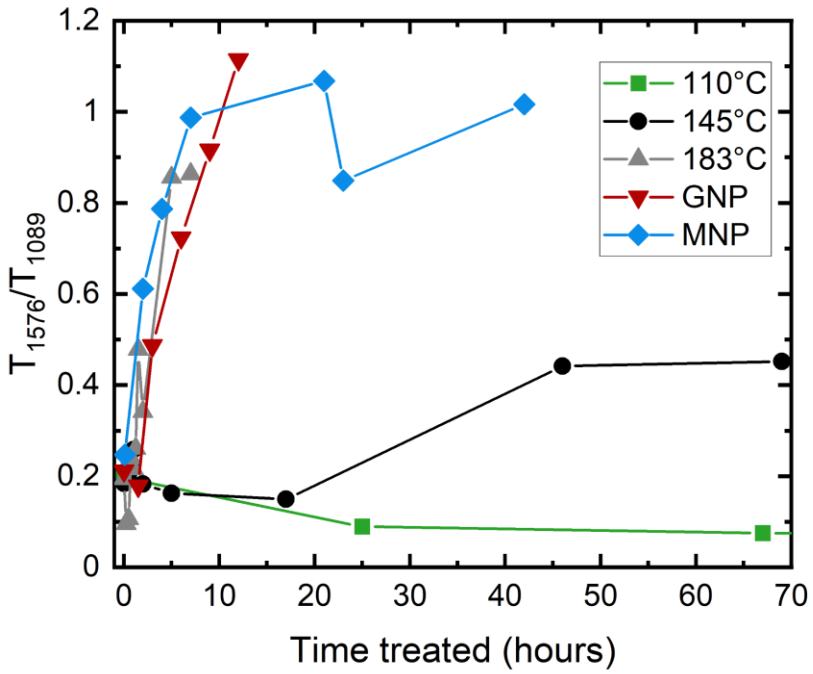

Figure 53: Transmission peak at 1576 cm^{-1} over time for all treatment cases. The 110 °C continues at the same level for the entire treatment time and is not included to ensure visibility of data at lower time scales.

The changing bonds within the PVA lead to an interesting bulk application, as the solubility in water of PVA depends on the presence and availability of the -OH side groups [233–236]. Water acts as a plasticizer for PVA, making the polymer film more like a gel and broadly softening it [233]. As a demonstration of the changing PVA structure, PVA was treated under standard conventional and photothermal conditions for variable amounts of time, and then placed in an excess of DI water for 3 hours to swell completely. With no treatment, the PVA quickly formed a loose gel in the water and was unable to be handled. However, the treated PVA displayed clear changes in the ability to hold water, as will be described below.

The water uptake of the PVA was calculated by a Q value, as used in other hydrogels,

$$Q = \frac{w_t - w_d}{w_d} = \frac{\Delta w}{w_d} \tag{13}$$

where here w_t is the total mass of the water and polymer after three hours, and w_d is the mass of the PVA sample after treatment but before being placed in water. For the untreated PVA samples that become gel-like, the Q value can be assumed as very large.

Table 5: Swelling test of PVA after thermal treatment.

Treatment method	Treatment time (hr)	Q after 3 hours in water (g water/g polymer)
Photothermal - GNP	1	9.28
Photothermal - MNP	1	5.33
Oven - 145 °C	1	1.22
	17	0.28
	69	0.10
Oven - 183 °C	0.25	0.31
	1	0.49
	1.5	0.44

As seen in Table 5, there was a decreasing water content for samples that had been treated for longer times and consequently proceeded further along in the degradation process. This aligns with the breaking of hydroxyls to form new structures or byproducts, as discussed previously. Although the FTIR signals suggested that the GNP and MNP samples resulted in similar degradation products (such as the C=C bond increase shown in Figure 53), both photothermally treated samples showed significantly more water swelling than the conventionally treated samples.

4.4 Conclusion

This chapter has described the low temperature degradation of PVA. The characteristics of this degradation have been detailed, including the changes in the absorption, mass, luminescence, and solubility.

The degradation from photothermal heating of GNPs and MNPs was also described. Both effectively degraded the polymer, with MNPs notably undergoing a similar universal degradation pathway as other polymers. This raises interesting questions about the temperatures being reached by the MNPs, which could be investigated with fluorescence thermometry measurements [21,77]. Isolating the MNPs in the FTIR would additionally provide insight into the changes in structure to the melanin, as the MNPs share many of the same peaks with PVA, making them difficult to isolate.

Chapter 5: Conclusions

5.1 Conclusions and Outlook

The photothermal heating of nanoparticles has been shown to have wide ranging possibilities and capabilities in changing polymer composites. This dissertation has investigated the potential to improve electrical conductivity, increase water evaporation rate, and modify polymer structures through photothermal heating, including through the photothermal heating of non-metallic nanoparticles.

In Chapter 2, we described how the electrical conductivity of MWCNT:PMMA composites could be improved by 2.5 times the starting conductivity. Local temperatures around the nanotubes (which were controlled by the laser intensity) were determined to be the primary driver of the conductivity change and allowed the nanotube junctions to improve electrical connection without large scale particle agglomeration. A simple temperature model suggested that only once the local temperature was above the T_g of the PMMA was there a conductivity improvement, as only then would there be the possibility for slight nanotube adjustments. This result was consistent even with variations to the global temperature. Reducing the thickness of the sample meant single nanotubes were more likely to be in contact with the surface, resulting in a heat loss that lowered the conductivity improvement. In the other direction, increasing the sample thickness eventually resulted in a shadowing effect from the nanotubes, such that the nanotubes near the top surface likely blocked light before it could reach nanotubes near the bottom surface of the sample. This reduced the possible conductivity improvements. Finally, the nature of the local heating allowed the bulk properties that were measured to remain constant. FTIR measurements suggested no polymer degradation, and the nanotube network appeared visually constant throughout treatment.

Several applications of such conductive composites are suggested in Chapter 2. The improvement of such a composite after manufacturing would allow for a reduced cost of the conductive filler. For example, a 0.125 wt% sample used here had a starting conductivity of 2.5×10^{-4} S/cm. A 0.25 wt% sample (2x the number of MWCNTs) had a starting conductivity of 7.0×10^{-4} S/cm (2.8x the conductivity of 0.125 wt%). This level of conductivity improvement for a 0.125 wt% therefore could be achieved by doubling the number of MWCNTs (2.8x improvement), which would double the cost of materials, or through a short laser treatment process that does not modify bulk properties of the material (2.5x improvement). Such improvement could be done for any application of conductive composites, regardless of end application, as long as light was able to penetrate the sample. These conductivity levels (10^{-4} S/cm) are in the correct range to be used in sensor applications (10^{-6} S/cm to 10^{-3} S/cm) [54,121,123–125]. Photothermal treatment would thus allow for a lower quantity of MWCNTs to be used in these sensors, though one could also imagine increasing the conductivity only in specific regions of the sensor by shaping the laser illumination to control the sensitivity in specific regions of the sample.

Chapter 3 investigated the use of photothermal heating in driving water evaporation. To begin, the microhydrogel composite NIPAM and SA, which has been suggested as a draw agent for water purification, was tested for basic properties of swelling capability and lower critical solution temperature (LCST). The combination of the two polymers did not exhibit the low LCST commonly associated with NIPAM, but there was still a transition at higher temperatures. The deswelling process was tracked for different applications of heat (ambient conditions, oven, and photothermal heating of both GNPs and MNPs) and different initial swellings of the hydrogel, though the initial swelling of the hydrogel had a minimal impact on the rate of water output. Once again, the temperatures present during photothermal heating – both globally and locally – were the

most notable aspect of the deswelling process. For photothermal heating, sample temperature was initially below room temperature (due to evaporative cooling) and increased significantly as the hydrogel lost water. The final measured temperature, which corresponds to the point at which all water had evaporated, was suggested to be an estimation of the local temperature. The local temperature is hypothesized to be the primary driver of water loss in the system. Both GNPs and MNPs were able to drive the water evaporation, though more MNPs may be required to achieve equivalent rates as the GNPs, due to the lower photothermal conversion. In comparing the oven heating to photothermal heating, it was seen that heating in an oven exhibited a slowdown at the end of the deswelling process, such that the deswelling rate at the beginning of the process was higher than that at the end. This was not seen in photothermal heating, suggesting that photothermal heating has self-corrective heating that prevents case hardening of the hydrogel.

The design of water purification technologies will become increasingly important in the current climate crisis, and understanding materials that can be used in this process provides options for energy, cost, and complexity. Utilizing photothermal heating in the deswelling process opens avenues in off-the-grid water purification processes, particularly with a broad light absorber like MNP that could use the Sun to power the evaporation process. This work thus investigated the properties and capabilities of both a composite hydrogel and photothermal heating, in an effort to improve understanding of hydrogels and MNPs in this context.

Chapter 4 further investigated and characterized MNPs. MNPs are effective photothermal heaters in hydrogels, which is a water-based environment. However, when placed in a water-lacking environment and photothermally heated, the MNPs appeared to degrade, exhibiting the universal polymer degradation luminescence. Even after degradation, the MNP degradation products were still able to photothermally heat, resulting in the degradation of the surrounding

PVA in a similar outcome as when photothermally heating with GNPs. MNP may provide an excellent option for nanoparticles in a variety of situations, from healthcare to materials, but such application requires a more complete understanding of the MNP in unique environments, which this work has attempted to begin.

In addition to the photothermal experiments, the PVA was degraded at several oven temperatures to both compare to the photothermal heating and to provide detailed results of PVA degradation processes, which previously have not included a tracking of the universal degradation luminescence. Understanding the degradation of polymers, particularly in a non-invasive mechanism such as a luminescence measurement, allows for better analysis of polymer lifespans. If universal degradation luminescence could be correlated with mechanical properties, a polymer material in use could be regularly checked and removed from service before a breaking point, which would allow for better planning and logistics and the prevent of any delays that may come from a sudden breakdown of equipment.

5.2 New Directions

There are several possible avenues to continue this work.

Looking at the conductive composites, there may be higher improvements possible using a different length of MWCNT, or using a different surfactant. In particular, the use of a less thermally stable surfactant may allow for the degradation of the surfactant around the nanotube, potential creating carbon bridges between the nanotubes.

The dewatering of hydrogels has both theoretical and practical directions. In the former, an investigation of the deswelling process (a more mathematical model of how the water evaporates) would allow for predictions of water evaporation and loss from the hydrogel, which could be used in cycling processes where a hydrogel is swollen and deswollen in order to retrieve maximum

water collection. Furthermore, an analysis of the energies within the system would provide a more complete understanding of the mechanisms driving the water loss, especially comparing the low LCST NIPAM with the combined NIPAM+SA. In general, a more theoretical understanding of how the combination of these two polymers may change the swelling and deswelling process would be an interesting study. On the practical side, there was no consideration of collecting the evaporated water in this work, which would naturally be required for any water purification process. An interesting direction here would be to utilize photothermal heating in a low LCST polymer like NIPAM, as that would support the collection of liquid water instead of vapor. Photothermal heating of a low LCST polymer and the use of macrohydrogels in photothermal heating would also provide insight into the case hardening effects and ways to minimize it.

Finally, the work done with MNPs here leaves many questions unanswered. Regarding the photothermal heating process, a study of the local temperature experienced by the MNPs, potentially through fluorescence thermometry, would give a more accurate understanding of the melanin degradation process. Further understanding of the degradation of MNPs could also be done through a more detailed chemical analysis of isolated MNPs (without the background of another polymer) and a variety of environments for the MNPs to degrade within, such as thermal treatment from both an oven and photothermal heating while the MNPs are in air, in solution, or in other polymers.

Overall, the photothermal heating of nanoparticles, as demonstrated here, has a wide range of potential applications. This relatively simple process of generating heat is able to be tailored through the particle composition, structure, spacing, and environment, and thus, this work aimed to expand the understanding of how a variety of nanoparticles could be utilized in a variety of situations.

REFERENCES

[1] I. Freestone, N. Meeks, M. Sax, and C. Higgitt, The Lycurgus Cup — A Roman nanotechnology, Gold Bull 40, 270 (2007).

[2] D. B. Harden and J. M. C. Toynbee, VII.—The Rothschild Lycurgus Cup, Archaeologia 97, 179 (1959).

[3] L. Kool, F. Dekker, A. Bunschoten, G. J. Smales, B. R. Pauw, A. H. Velders, and V. Saggiomo, Gold and silver dichroic nanocomposite in the quest for 3D printing the Lycurgus cup, Beilstein J. Nanotechnol. 11, 16 (2020).

[4] D. J. Barber and I. C. Freestone, An Investigation of the Origin of the Color of the Lycurgus Cup by Analytical Transmission Electron Microscopy, Archaeometry 32, 33 (1990).

[5] M. E. Matter, C. Tagnon, and E. E. Stache, Recent Applications of Photothermal Conversion in Organic Synthesis, ACS Cent. Sci. 10, 1460 (2024).

[6] X. Cui, Q. Ruan, X. Zhuo, X. Xia, J. Hu, R. Fu, Y. Li, J. Wang, and H. Xu, Photothermal Nanomaterials: A Powerful Light-to-Heat Converter, Chem. Rev. 123, 6891 (2023).

[7] N. Li, P. Zhao, and D. Astruc, Anisotropic Gold Nanoparticles: Synthesis, Properties, Applications, and Toxicity, Angewandte Chemie International Edition 53, 1756 (2014).

[8] X. Liu, M. Atwater, J. Wang, and Q. Huo, Extinction coefficient of gold nanoparticles with different sizes and different capping ligands, Colloids and Surfaces B: Biointerfaces 58, 3 (2007).

[9] P. K. Jain, K. S. Lee, I. H. El-Sayed, and M. A. El-Sayed, Calculated Absorption and Scattering Properties of Gold Nanoparticles of Different Size, Shape, and Composition: Applications in Biological Imaging and Biomedicine, J. Phys. Chem. B 110, 7238 (2006).

[10] L. Scarabelli, A. Sánchez-Iglesias, J. Pérez-Juste, and L. M. Liz-Marzán, A "Tips and Tricks" Practical Guide to the Synthesis of Gold Nanorods, J. Phys. Chem. Lett. 6, 4270 (2015).

[11] S. W. Prescott and P. Mulvaney, Gold nanorod extinction spectra, Journal of Applied Physics 99, 123504 (2006).

[12] Y. Hang, A. Wang, and N. Wu, Plasmonic silver and gold nanoparticles: shape- and structure-modulated plasmonic functionality for point-of-caring sensing, bio-imaging and medical therapy, Chem. Soc. Rev. 53, 2932 (2024).

[13] K. L. Kelly, E. Coronado, L. L. Zhao, and G. C. Schatz, The Optical Properties of Metal Nanoparticles: The Influence of Size, Shape, and Dielectric Environment, J. Phys. Chem. B 107, 668 (2003).

[14] K. Park, S. Biswas, S. Kanel, D. Nepal, and R. A. Vaia, Engineering the Optical Properties of Gold Nanorods: Independent Tuning of Surface Plasmon Energy, Extinction Coefficient, and Scattering Cross Section, J. Phys. Chem. C 118, 5918 (2014).

[15] C. J. Orendorff and C. J. Murphy, Quantitation of Metal Content in the Silver-Assisted Growth of Gold Nanorods, J. Phys. Chem. B 110, 3990 (2006).

[16] Y. Liu, E. N. Mills, and R. J. Composto, Tuning optical properties of gold nanorods in polymer films through thermal reshaping, Journal of Materials Chemistry 19, 2704 (2009).

[17] A. D. Kondorskiy and V. S. Lebedev, Size and Shape Effects in Optical Spectra of Silver and Gold Nanoparticles, J Russ Laser Res 42, 697 (2021).

[18] L. Zhu, M. Gao, C. K. N. Peh, and G. W. Ho, Solar-driven photothermal nanostructured materials designs and prerequisites for evaporation and catalysis applications, Mater. Horiz. 5, 323 (2018).

[19] K. Jiang, D. A. Smith, and A. Pinchuk, Size-Dependent Photothermal Conversion Efficiencies of Plasmonically Heated Gold Nanoparticles, J. Phys. Chem. C 117, 27073 (2013).

[20] H. Zhang, H.-J. Chen, X. Du, and D. Wen, Photothermal conversion characteristics of gold nanoparticle dispersions, Solar Energy 100, 141 (2014).

[21] M.-J. Chiu and L.-K. Chu, Quantifying the photothermal efficiency of gold nanoparticles using tryptophan as an in situ fluorescent thermometer, Phys. Chem. Chem. Phys. 17, 17090 (2015).

[22] H. S. Kim and D. Y. Lee, Near-Infrared-Responsive Cancer Photothermal and Photodynamic Therapy Using Gold Nanoparticles, Polymers 10, 961 (2018).

[23] H. H. Richardson, M. T. Carlson, P. J. Tandler, P. Hernandez, and A. O. Govorov, Experimental and Theoretical Studies of Light-to-Heat Conversion and Collective Heating Effects in Metal Nanoparticle Solutions, Nano Lett. 9, 1139 (2009).

[24] S. Maity, K. A. Kozek, W.-C. Wu, J. B. Tracy, J. R. Bochinski, and L. I. Clarke, Anisotropic Thermal Processing of Polymer Nanocomposites via the Photothermal Effect of Gold Nanorods, Particle & Particle Systems Characterization 30, 193 (2013).

[25] W. Haiss, N. T. K. Thanh, J. Aveyard, and D. G. Fernig, Determination of Size and Concentration of Gold Nanoparticles from UV−Vis Spectra, Anal. Chem. 79, 4215 (2007).

[26] G. Frens, Controlled Nucleation for the Regulation of the Particle Size in Monodisperse Gold Suspensions, Nature Physical Science 241, 20 (1973).

[27] I. Pastoriza-Santos, J. Pérez-Juste, and L. M. Liz-Marzán, Silica-Coating and Hydrophobation of CTAB-Stabilized Gold Nanorods, Chem. Mater. 18, 2465 (2006).

[28] S. Barbosa, A. Agrawal, L. Rodríguez-Lorenzo, I. Pastoriza-Santos, R. A. Alvarez-Puebla, A. Kornowski, H. Weller, and L. M. Liz-Marzán, Tuning Size and Sensing Properties in Colloidal Gold Nanostars, Langmuir 26, 14943 (2010).

[29] P. Senthil Kumar, I. Pastoriza-Santos, B. Rodríguez-González, F. Javier García de Abajo, and L. M. Liz-Marzán, High-yield synthesis and optical response of gold nanostars, Nanotechnology 19, 015606 (2007).

[30] A. Miranda, E. Malheiro, P. Eaton, P. A. Carvalho, B. de Castro, and E. Pereira, Synthesis of gold nanocubes in aqueous solution with remarkable shape-selectivity, J. Porphyrins Phthalocyanines 15, 441 (2011).

[31] X. Wu, T. Ming, X. Wang, P. Wang, J. Wang, and J. Chen, High-Photoluminescence-Yield Gold Nanocubes: For Cell Imaging and Photothermal Therapy, ACS Nano 4, 113 (2010).

[32] L. Scarabelli, M. Coronado-Puchau, J. J. Giner-Casares, J. Langer, and L. M. Liz-Marzán, Monodisperse Gold Nanotriangles: Size Control, Large-Scale Self-Assembly, and Performance in Surface-Enhanced Raman Scattering, ACS Nano 8, 5833 (2014).

[33] C. M. Otero, G. B. Simal, M. F. Scocozza, A. Rubert, C. A. Grillo, L. Hannibal, G. Lavorato, M. A. Huergo, D. H. Murgida, and C. Vericat, Optimized Biocompatible Gold Nanotriangles with NIR Absorption for Photothermal Applications, ACS Appl. Nano Mater. 5, 341 (2022).

[34] X. Yu, Z. Wang, H. Cui, X. Wu, W. Chai, J. Wei, Y. Chen, and Z. Zhang, A Review on Gold Nanotriangles: Synthesis, Self-Assembly and Their Applications, Molecules 27, 24 (2022).

[35] J. Zeng, Y. Zhang, T. Zeng, R. Aleisa, Z. Qiu, Y. Chen, J. Huang, D. Wang, Z. Yan, and Y. Yin, Anisotropic plasmonic nanostructures for colorimetric sensing, Nano Today 32, 100855 (2020).

[36] A. M. Alkilany and C. J. Murphy, Toxicity and cellular uptake of gold nanoparticles: what we have learned so far?, J Nanopart Res 12, 2313 (2010).

[37] E. C. Dreaden, A. M. Alkilany, X. Huang, C. J. Murphy, and M. A. El-Sayed, The golden age: gold nanoparticles for biomedicine, Chem. Soc. Rev. 41, 2740 (2012).

[38] Y. Zhang, B. Newton, E. Lewis, P. P. Fu, R. Kafoury, P. C. Ray, and H. Yu, Cytotoxicity of Organic Surface Coating Agents Used for Nanoparticles Synthesis and Stability, Toxicol In Vitro 29, 762 (2015).

[39] M. Gao, L. Zhu, C. K. Peh, and G. W. Ho, Solar absorber material and system designs for photothermal water vaporization towards clean water and energy production, Energy Environ. Sci. 12, 841 (2019).

[40] L. M. Maestro, P. Haro-González, B. del Rosal, J. Ramiro, A. J. Caamaño, E. Carrasco, A. Juarranz, F. Sanz-Rodríguez, J. G. Solé, and D. Jaque, Heating efficiency of multi-walled carbon nanotubes in the first and second biological windows, Nanoscale 5, 7882 (2013).

[41] M. Alrahili, Light to heat conversion efficiency of single-walled carbon nanotubes, Journal of Taibah University for Science 16, 923 (2022).

[42] W. Luo, X. Xuan, J. Shen, P. Cheng, D. Wang, P. Schaaf, Z. Zhang, and J. Liu, High performance photothermal carbon nanotubes/nanostructured hydrogel for solar electricity production and solar water sterilization, Applied Surface Science 643, 158680 (2024).

[43] N. Sahadev and A. A. Anappara, Photothermal effect in solid-state MWCNT: Possible signatures of thermal anisotropy, Journal of Applied Physics 124, 145104 (2018).

[44] Q. Zhang, W. Xu, and X. Wang, Carbon nanocomposites with high photothermal conversion efficiency, Sci. China Mater. 61, 905 (2018).

[45] F. Oudjedi, S. S. Lee, M. Paliouras, M. Trifiro, and A. G. Kirk, Enhancing in vitro photothermal therapy using plasmonic gold nanorod decorated multiwalled carbon nanotubes, Biomed. Opt. Express, BOE 14, 6629 (2023).

[46] S. Awasthi, A. Srivastava, D. Kumar, S. K. Pandey, N. M. Mubarak, M. H. Dehghani, and K. Ansari, An insight into the toxicological impacts of carbon nanotubes (CNTs) on human health: A review, Environmental Advances 18, 100601 (2024).

[47] D. Wang, X. Lin, Y. Wu, L. Li, W. Feng, Y. Huang, and Y. Yang, Hanging Photothermal Fabric Based on Polyaniline/Carbon Nanotubes for Efficient Solar Water Evaporation, ACS Omega 8, 44659 (2023).

[48] H. Wang, A. Du, X. Ji, C. Zhang, B. Zhou, Z. Zhang, and J. Shen, Enhanced Photothermal Conversion by Hot-Electron Effect in Ultrablack Carbon Aerogel for Solar Steam Generation, ACS Appl. Mater. Interfaces 11, 42057 (2019).

[49] S. Cao, Q. Jiang, X. Wu, D. Ghim, H. Gholami Derami, P.-I. Chou, Y.-S. Jun, and S. Singamaneni, Advances in solar evaporator materials for freshwater generation, J. Mater. Chem. A 7, 24092 (2019).

[50] H. Wang, R. Wang, C. Chen, Z. Zhou, and J.-W. Liu, Manipulating Single-Walled Carbon Nanotube Arrays for Flexible Photothermoelectric Devices, JACS Au 2, 2269 (2022).

[51] C. Choi, T. G. Yun, and B. Hwang, Dispersion Stability of Carbon Nanotubes and Their Impact on Energy Storage Devices, Inorganics 11, 10 (2023).

[52] J. Gao, H. Wang, X. Huang, M. Hu, H. Xue, and R. K. Y. Li, Electrically conductive polymer nanofiber composite with an ultralow percolation threshold for chemical vapour sensing, Composites Science and Technology 161, 135 (2018).

[53] B. Philip, J. K. Abraham, A. Chandrasekhar, and V. K. Varadan, Carbon nanotube/PMMA composite thin films for gas-sensing applications, Smart Mater. Struct. 12, 935 (2003).

[54] J. R. Garcia, D. O'Suilleabhain, H. Kaur, and J. N. Coleman, A Simple Model Relating Gauge Factor to Filler Loading in Nanocomposite Strain Sensors, ACS Appl. Nano Mater. 4, 2876 (2021).

[55] T. Wang, J. Yang, J. Berger, N. Boz, S. Tekampe, M. Oeser, and P. Liu, Mechanical and piezoresistive performance of polymethyl methacrylate modified with carbon nanotubes for sensitive road surface, Materials Today Communications 41, 110255 (2024).

[56] S. I. Moseenkov, V. L. Kuznetsov, G. V. Golubtsov, A. V. Zavorin, and A. N. Serkova, Effect of ultrasonic treatment on the properties of multiwalled carbon nanotubes – polymethylmethacrylate composites: Effect of applied voltage and pressure on conductivity of the composites, Express Polym. Lett. 13, 1057 (2019).

[57] W. Xie, A. Dhinojwala, N. C. Gianneschi, and M. D. Shawkey, Interactions of Melanin with Electromagnetic Radiation: From Fundamentals to Applications, Chem. Rev. 124, 7165 (2024).

[58] A. B. Mostert, Melanin, the What, the Why and the How: An Introductory Review for Materials Scientists Interested in Flexible and Versatile Polymers, Polymers 13, 10 (2021).

[59] M. d'Ischia et al., Melanins and melanogenesis: methods, standards, protocols, Pigment Cell Melanoma Res 26, 616 (2013).

[60] A. Liopo, R. Su, and A. A. Oraevsky, Melanin nanoparticles as a novel contrast agent for optoacoustic tomography, Photoacoustics 3, 35 (2015).

[61] K.-Y. Ju, Y. Lee, S. Lee, S. B. Park, and J.-K. Lee, Bioinspired Polymerization of Dopamine to Generate Melanin-Like Nanoparticles Having an Excellent Free-Radical-Scavenging Property, Biomacromolecules 12, 625 (2011).

[62] A. Menichetti, D. Mordini, and M. Montalti, Melanin as a Photothermal Agent in Antimicrobial Systems, International Journal of Molecular Sciences 25, 16 (2024).

[63] Y. Liu, B. Li, C. Yi, X. Chen, and X. Yu, Application of polydopamine as antibacterial and anti-inflammatory materials, Prog. Biomed. Eng. 7, 022005 (2025).

[64] S. Maher, M. Mahmoud, M. Rizk, and H. Kalil, Synthetic melanin nanoparticles as peroxynitrite scavengers, photothermal anticancer and heavy metals removal platforms, Environ Sci Pollut Res 27, 19115 (2020).

[65] Z. Yang, H. Liu, J. Zhao, C. Wang, H. Li, X. Wang, Y. Yang, H. Wu, Z. Gu, and Y. Li, UV absorption enhanced polydopamine coating, Mater. Horiz. 11, 2438 (2024).

[66] W. Bai, P. Yang, H. Liu, Y. Zou, X. Wang, Y. Yang, Z. Gu, and Y. Li, Boosting the Optical Absorption of Melanin-like Polymers, Macromolecules 55, 3493 (2022).

[67] Y. Zou, X. Chen, P. Yang, G. Liang, Y. Yang, Z. Gu, and Y. Li, Regulating the absorption spectrum of polydopamine, Science Advances 6, eabb4696 (2020).

[68] Y. He, Z. Li, H. Su, Y. Sun, W. Shi, Y. Yi, D. Ge, and Z. Fan, Pyrrole-Doped Polydopamine-Pyrrole (PDA-nPY) Nanoparticles with Tunable Size and Improved NIR Absorption for Photothermal Therapy, Pharmaceuticals 16, 12 (2023).

[69] Q. Jiang, Z. Luo, Y. Men, P. Yang, H. Peng, R. Guo, Y. Tian, Z. Pang, and W. Yang, Red blood cell membrane-camouflaged melanin nanoparticles for enhanced photothermal therapy, Biomaterials 143, 29 (2017).

[70] P. Yang, S. Zhang, N. Zhang, Y. Wang, J. Zhong, X. Sun, Y. Qi, X. Chen, Z. Li, and Y. Li, Tailoring Synthetic Melanin Nanoparticles for Enhanced Photothermal Therapy, ACS Appl. Mater. Interfaces 11, 42671 (2019).

[71] Y. Liu, K. Ai, J. Liu, M. Deng, Y. He, and L. Lu, Dopamine-Melanin Colloidal Nanospheres: An Efficient Near-Infrared Photothermal Therapeutic Agent for In Vivo Cancer Therapy, Advanced Materials 25, 1353 (2013).

[72] I. Marcovici, D. Coricovac, I. Pinzaru, I. G. Macasoi, R. Popescu, R. Chioibas, I. Zupko, and C. A. Dehelean, Melanin and Melanin-Functionalized Nanoparticles as Promising Tools in Cancer Research—A Review, Cancers 14, 7 (2022).

[73] C. Ninh, M. Cramer, and C. J. Bettinger, Photoresponsive hydrogel networks using melanin nanoparticle photothermal sensitizers, Biomater. Sci. 2, 766 (2014).

[74] V. Petropoulos, A. Mavridi-Printezi, A. Menichetti, D. Mordini, P. Kabacinski, N. C. Gianneschi, M. Montalti, M. Maiuri, and G. Cerullo, Sub-50 fs Formation of Charge Transfer States Rules the Fate of Photoexcitations in Eumelanin-Like Materials, J. Phys. Chem. Lett. 15, 3639 (2024).

[75] Z. Qin and J. C. Bischof, Thermophysical and biological responses of gold nanoparticle laser heating, Chem. Soc. Rev. 41, 1191 (2012).

[76] S. Maity, W.-C. Wu, J. B. Tracy, L. I. Clarke, and J. R. Bochinski, Nanoscale steady-state temperature gradients within polymer nanocomposites undergoing continuous-wave photothermal heating from gold nanorods, Nanoscale 9, 11605 (2017).

[77] S. Maity, W.-C. Wu, C. Xu, J. B. Tracy, K. Gundogdu, J. R. Bochinski, and L. I. Clarke, Spatial temperature mapping within polymer nanocomposites undergoing ultrafast photothermal heating via gold nanorods, Nanoscale 6, 15236 (2014).

[78] Y. Kumar, A. S. K. Sinha, K. D. P. Nigam, D. Dwivedi, and J. S. Sangwai, Functionalized nanoparticles: Tailoring properties through surface energetics and coordination chemistry for advanced biomedical applications, Nanoscale 15, 6075 (2023).

[79] R. Thiruppathi, S. Mishra, M. Ganapathy, P. Padmanabhan, and B. Gulyás, Nanoparticle Functionalization and Its Potentials for Molecular Imaging, Adv Sci (Weinh) 4, 1600279 (2016).

[80] L. Zhao, X. Zhang, X. Wang, X. Guan, W. Zhang, and J. Ma, Recent advances in selective photothermal therapy of tumor, Journal of Nanobiotechnology 19, 335 (2021).

[81] D. Jaque, L. M. Maestro, B. del Rosal, P. Haro-Gonzalez, A. Benayas, J. L. Plaza, E. M. Rodríguez, and J. G. Solé, Nanoparticles for photothermal therapies, Nanoscale 6, 9494 (2014).

[82] J. Chen, C. Ning, Z. Zhou, P. Yu, Y. Zhu, G. Tan, and C. Mao, Nanomaterials as photothermal therapeutic agents, Progress in Materials Science 99, 1 (2019).

[83] I. Fratoddi, I. Venditti, C. Cametti, and M. V. Russo, How toxic are gold nanoparticles? The state-of-the-art, Nano Res. 8, 1771 (2015).

[84] M. Weng, P. Zhou, L. Chen, L. Zhang, W. Zhang, Z. Huang, C. Liu, and S. Fan, Multiresponsive Bidirectional Bending Actuators Fabricated by a Pencil-on-Paper Method, Advanced Functional Materials 26, 7244 (2016).

[85] H. Li and J. Wang, Ultrafast yet Controllable Dual-Responsive All-Carbon Actuators for Implementing Unusual Mechanical Movements, ACS Appl. Mater. Interfaces 11, 10218 (2019).

[86] H. Šípová-Jungová, D. Andrén, S. Jones, and M. Käll, Nanoscale Inorganic Motors Driven by Light: Principles, Realizations, and Opportunities, Chem. Rev. 120, 269 (2020).

[87] X. Wang, C. Zhang, F. Chen, J. Xiang, S. Wang, Z. Liu, and T. Ding, Optically Triggered Nanoscale Plasmonic Dynamite, ACS Nano 16, 13667 (2022).

[88] J. Dong, G. E. Firestone, J. R. Bochinski, L. I. Clarke, and R. E. Gorga, In situ curing of liquid epoxy via gold-nanoparticle mediated photothermal heating, Nanotechnology 28, 065601 (2017).

[89] S. Fang and Y. H. Hu, Thermo-photo catalysis: a whole greater than the sum of its parts, Chem. Soc. Rev. 51, 3609 (2022).

[90] C. Song, Z. Wang, Z. Yin, D. Xiao, and D. Ma, Principles and applications of photothermal catalysis, Chem Catalysis 2, 52 (2022).

[91] H. Huang, G. Firestone, D. Fontecha, R. E. Gorga, J. R. Bochinski, and L. I. Clarke, Nanoparticle-based photothermal heating to drive chemical reactions within a solid: using inhomogeneous polymer degradation to manipulate mechanical properties and segregate carbonaceous by-products, Nanoscale 12, 904 (2020).

[92] D. Fontecha, C. Mahn, J. Bochinski, and L. Clarke, Tracking the complete degradation lifecycle of poly(ethyl cyanoacrylate): from induced photoluminescence to nitrogen-doped graphene-like residue, Polymer Degradation and Stability 195, 109772 (2022).

[93] O. Neumann, A. S. Urban, J. Day, S. Lal, P. Nordlander, and N. J. Halas, Solar Vapor Generation Enabled by Nanoparticles, ACS Nano 7, 42 (2013).

[94] N. Chen, H. Ma, Y. Li, J. Cheng, C. Zhang, D. Wu, and H. Zhu, Complementary optical absorption and enhanced solar thermal conversion of CuO-ATO nanofluids, Solar Energy Materials and Solar Cells 162, 83 (2017).

[95] G. Ni et al., Volumetric solar heating of nanofluids for direct vapor generation, Nano Energy 17, 290 (2015).

[96] Z. Xu et al., Recent advances in solar-driven evaporation systems, J. Mater. Chem. A 8, 25571 (2020).

[97] M. Zhu, X. Liu, Y. Tian, A. Caratenuto, F. Chen, and Y. Zheng, Dome-arrayed chitosan/PVA hydrogel-based solar evaporator for steam generation, Sci Rep 12, 4403 (2022).

[98] X. Song, Y. Wang, C. Wang, M. Huang, S. Gul, and H. Jiang, Solar-Intensified Ultrafiltration System Based on Porous Photothermal Membrane for Efficient Water Treatment, ACS Sustainable Chem. Eng. 7, 4889 (2019).

[99] L. Zang, C. Finnerty, S. Zheng, K. Conway, L. Sun, J. Ma, and B. Mi, Interfacial solar vapor generation for desalination and brine treatment: Evaluating current strategies of solving scaling, Water Research 198, 117135 (2021).

[100] N. Mohd Nurazzi et al., Fabrication, Functionalization, and Application of Carbon Nanotube-Reinforced Polymer Composite: An Overview, Polymers 13, 1047 (2021).

[101] W. Bauhofer and J. Z. Kovacs, A review and analysis of electrical percolation in carbon nanotube polymer composites, Composites Science and Technology 69, 1486 (2009).

[102] Y. Zare and K. Y. Rhee, Polymer tunneling resistivity between adjacent carbon nanotubes (CNT) in polymer nanocomposites, Journal of Physics and Chemistry of Solids 147, 109664 (2020).

[103] J. Li, P. C. Ma, W. S. Chow, C. K. To, B. Z. Tang, and J.-K. Kim, Correlations between Percolation Threshold, Dispersion State, and Aspect Ratio of Carbon Nanotubes, Advanced Functional Materials 17, 3207 (2007).

[104] B. P. Grady, Recent Developments Concerning the Dispersion of Carbon Nanotubes in Polymers, Macromolecular Rapid Communications 31, 247 (2010).

[105] L. Cao, Y. Liu, J. Wang, Y. Pan, Y. Zhang, N. Wang, and J. Chen, Multi-Functional Properties of MWCNT/PVA Buckypapers Fabricated by Vacuum Filtration Combined with Hot Press: Thermal, Electrical and Electromagnetic Shielding, Nanomaterials 10, 12 (2020).

[106] G. Trakakis et al., Mechanical, Electrical, and Thermal Properties of Carbon Nanotube Buckypapers/Epoxy Nanocomposites Produced by Oxidized and Epoxidized Nanotubes, Materials 13, 19 (2020).

[107] C. Kostaras, C. Pavlou, N. Koutroumanis, G. Paterakis, G. Trakakis, C. Galiotis, and K. Dassios, Rapid Resistive Heating in Graphene/Carbon Nanotube Hybrid Films for De-icing Applications, ACS Appl. Nano Mater. 6, 5155 (2023).

[108] R. H. Schmidt, I. A. Kinloch, A. N. Burgess, and A. H. Windle, The Effect of Aggregation on the Electrical Conductivity of Spin-Coated Polymer/Carbon Nanotube Composite Films, Langmuir 23, 5707 (2007).

[109] Y. Y. Huang and E. M. Terentjev, Dispersion of Carbon Nanotubes: Mixing, Sonication, Stabilization, and Composite Properties, Polymers 4, 275 (2012).

[110] J. K. W. Sandler, J. E. Kirk, I. A. Kinloch, M. S. P. Shaffer, and A. H. Windle, Ultra-low electrical percolation threshold in carbon-nanotube-epoxy composites, Polymer 44, 5893 (2003).

[111] I. Hattenhauer, P. P. Tambosi, C. A. Duarte, L. A. F. Coelho, A. Ramos, and S. H. Pezzin, Impact of Electric Field Application During Curing on Epoxy-Carbon Nanotube Nanocomposite Electrical Conductivity, J Inorg Organomet Polym 25, 627 (2015).

[112] J. W. Hur, H. J. Yoo, J. W. Cho, and K. H. Kim, Orientation and mechanical properties of laser-induced photothermally drawn fibers composed of multiwalled carbon nanotubes and poly(ethylene terephthalate), Journal of Polymer Science Part B: Polymer Physics 54, 603 (2016).

[113] B. H. Lee, J. W. Cho, and K. H. Kim, Crystallization, orientation, and mechanical properties of laser-heated photothermally drawn polypropylene/multi-walled carbon nanotube fibers, European Polymer Journal 91, 70 (2017).

[114] A. T. Roberts, J. Yang, M. E. Reish, A. Alabastri, N. J. Halas, P. Nordlander, and H. O. Everitt, Plasmonic nanoparticle-based epoxy photocuring: A deeper look, Materials Today 27, 14 (2019).

[115] Y. Liu, Z. Lin, P. Wang, F. Huang, and J.-L. Sun, Measurement of the Photothermal Conversion Efficiency of CNT Films Utilizing a Raman Spectrum, Nanomaterials (Basel) 12, 1101 (2022).

[116] S. Siregar, S. Oktamuliani, and Y. Saijo, A Theoretical Model of Laser Heating Carbon Nanotubes, Nanomaterials (Basel) 8, 580 (2018).

[117] H. Jiang, Y.-J. Jang, C. Tagnon, E. A. Medina, and E. E. Stache, Emerging Plastic Recycling Strategies Based on Photothermal Conversion, ACS Appl. Polym. Mater. 7, 1163 (2025).

[118] Y. Ren, Y. Yan, and H. Qi, Photothermal conversion and transfer in photothermal therapy: From macroscale to nanoscale, Advances in Colloid and Interface Science 308, 102753 (2022).

[119] M. Sabet, Innovations in carbon nanotube polymer composites: Electrical, thermal, and mechanical advancements for aerospace and automotive applications, Synthetic Metals 310, 117794 (2025).

[120] R. Rahman and P. Servati, Effects of inter-tube distance and alignment on tunnelling resistance and strain sensitivity of nanotube/polymer composite films, Nanotechnology 23, 055703 (2012).

[121] F. Avilés, A. I. Oliva, G. Ventura, A. May-Pat, and A. I. Oliva-Avilés, Effect of carbon nanotube length on the piezoresistive response of poly (methyl methacrylate) nanocomposites, European Polymer Journal 110, 394 (2019).

[122] S. Shang, L. Li, X. Yang, and Y. Wei, Polymethylmethacrylate-carbon nanotubes composites prepared by microemulsion polymerization for gas sensor, Composites Science and Technology 69, 1156 (2009).

[123] G. T. Pham, Y.-B. Park, Z. Liang, C. Zhang, and B. Wang, Processing and modeling of conductive thermoplastic/carbon nanotube films for strain sensing, Composites Part B: Engineering 39, 209 (2008).

[124] S. Bharadwaj, T. K. Gupta, G. S. Chauhan, M. Sehrawat, A. Kumar, S. R. Dhakate, and B. P. Singh, Long Length MWCNT/TPU Composite Materials for Stretchable and Wearable Strain Sensors, Sensors and Actuators A: Physical 357, 114364 (2023).

[125] G. S. Kumar and T. U. Patro, Tuning the piezoresistive strain-sensing behavior of poly(vinylidene fluoride)–CNT composites: The role of polymer–CNT interface and composite processing technique, Journal of Applied Polymer Science 139, 51516 (2022).

[126] T. Wang, Yang ,Jun, Oeser ,Markus, and P. and Liu, Improved micromechanics model for piezoresistive polymethyl methacrylate modified with carbon nanotubes: considering the effect of mineral fillers, International Journal of Pavement Engineering 25, 2405029 (2024).

[127] Q. Cheng, S. Debnath, L. O'Neill, T. G. Hedderman, E. Gregan, and H. J. Byrne, Systematic Study of the Dispersion of SWNTs in Organic Solvents, J. Phys. Chem. C 114, 4857 (2010).

[128] S. M. Fatemi and M. Foroutan, Study of dispersion of carbon nanotubes by Triton X-100 surfactant using molecular dynamics simulation, J IRAN CHEM SOC 12, 1905 (2015).

[129] R. Rastogi, R. Kaushal, S. K. Tripathi, A. L. Sharma, I. Kaur, and L. M. Bharadwaj, Comparative study of carbon nanotube dispersion using surfactants, Journal of Colloid and Interface Science 328, 421 (2008).

[130] J. W. Essam, Percolation theory, Reports on Progress in Physics 43, 833 (1980).

[131] P. H. da S. L. Coelho, M. S. Marchesin, A. R. Morales, and J. R. Bartoli, Electrical percolation, morphological and dispersion properties of MWCNT/PMMA nanocomposites, Mat. Res. 17, 127 (2014).

[132] E. J. Garboczi, K. A. Snyder, J. F. Douglas, and M. F. Thorpe, Geometrical percolation threshold of overlapping ellipsoids, Phys. Rev. E 52, 819 (1995).

[133] M. Foygel, R. D. Morris, D. Anez, S. French, and V. L. Sobolev, Theoretical and computational studies of carbon nanotube composites and suspensions: Electrical and thermal conductivity, Phys. Rev. B 71, 104201 (2005).

[134] M. Ferriol, A. Gentilhomme, M. Cochez, N. Oget, and J. L. Mieloszynski, Thermal degradation of poly(methyl methacrylate) (PMMA): modelling of DTG and TG curves, Polymer Degradation and Stability 79, 271 (2003).

[135] Z. G. Ayanoğlu and M. Doğan, Characterization and thermal kinetic analysis of PMMA/modified-MWCNT nanocomposites, Diamond and Related Materials 108, 107950 (2020).

[136] M. L. Saladino, T. E. Motaung, A. S. Luyt, A. Spinella, G. Nasillo, and E. Caponetti, The effect of silica nanoparticles on the morphology, mechanical properties and thermal degradation kinetics of PMMA, Polymer Degradation and Stability 97, 452 (2012).

[137] S. Ramesh, K. H. Leen, K. Kumutha, and A. K. Arof, FTIR studies of PVC/PMMA blend based polymer electrolytes, Spectrochimica Acta Part A: Molecular and Biomolecular Spectroscopy 66, 1237 (2007).

[138] V. V. Soman and D. S. Kelkar, FTIR Studies of Doped PMMA - PVC Blend System, Macromolecular Symposia 277, 152 (2009).

[139] K. Mitsuda, H. Kimura, and T. Murahashi, Evaporation and decomposition of Triton X-100 under various gases and temperatures, J Mater Sci 24, 413 (1989).

[140] E. Santacesaria, D. Gelosa, M. Di Serio, and R. Tesser, Thermal stability of nonionic polyoxyalkylene surfactants, Journal of Applied Polymer Science 42, 2053 (1991).

[141] M. Neumann, G. di Marco, D. Iudin, M. Viola, C. F. van Nostrum, B. G. P. van Ravensteijn, and T. Vermonden, Stimuli-Responsive Hydrogels: The Dynamic Smart Biomaterials of Tomorrow, Macromolecules 56, 8377 (2023).

[142] Z. Zhang, H. Fu, Z. Li, J. Huang, Z. Xu, Y. Lai, X. Qian, and S. Zhang, Hydrogel materials for sustainable water resources harvesting & treatment: Synthesis, mechanism and applications, Chemical Engineering Journal 439, 135756 (2022).

[143] H. M. Wilson, H. W. Lim, and S. J. Lee, Highly Efficient and Salt-Rejecting Poly(vinyl alcohol) Hydrogels with Excellent Mechanical Strength for Solar Desalination, ACS Appl. Mater. Interfaces 14, 47800 (2022).

[144] D. Qin, Z. Liu, H. Bai, X. Song, Z. Li, and D. D. Sun, Fine-tuning selective layer architecture of hydrogel membrane towards high separation performances for engineered osmosis, Journal of Membrane Science 592, 117370 (2019).

[145] H. Zhang, J. Li, H. Cui, H. Li, and F. Yang, Forward osmosis using electric-responsive polymer hydrogels as draw agents: Influence of freezing–thawing cycles, voltage, feed solutions on process performance, Chemical Engineering Journal 259, 814 (2015).

[146] A. A. Salehi, M. Ghannadi-Maragheh, M. Torab-Mostaedi, R. Torkaman, and M. Asadollahzadeh, Hydrogel materials as an emerging platform for desalination and the production of purified water, Separation & Purification Reviews 1 (2020).

[147] D. Li, X. Zhang, G. P. Simon, and H. Wang, Forward osmosis desalination using polymer hydrogels as a draw agent: Influence of draw agent, feed solution and membrane on process performance, Water Research 47, 209 (2013).

[148] W. Ali, B. Gebert, T. Hennecke, K. Graf, M. Ulbricht, and J. S. Gutmann, Design of Thermally Responsive Polymeric Hydrogels for Brackish Water Desalination: Effect of Architecture on Swelling, Deswelling, and Salt Rejection, ACS Appl. Mater. Interfaces 7, 15696 (2015).

[149] H. Chang, H. Zhao, F. Qu, Z. Yan, N. Liu, M. Lu, Y. Liang, B. Lai, and H. Liang, State-of-the-art insights on applications of hydrogel membranes in water and wastewater treatment, Separation and Purification Technology 308, 122948 (2023).

[150] S. Zhao, L. Zou, and D. Mulcahy, Brackish water desalination by a hybrid forward osmosis–nanofiltration system using divalent draw solute, Desalination 284, 175 (2012).

[151] N. Akther, A. Sodiq, A. Giwa, S. Daer, H. A. Arafat, and S. W. Hasan, Recent advancements in forward osmosis desalination: A review, Chemical Engineering Journal 281, 502 (2015).

[152] T. Y. Cath, A. E. Childress, and M. Elimelech, Forward osmosis: Principles, applications, and recent developments, Journal of Membrane Science 281, 70 (2006).

[153] D. Li, Y. Yan, and H. Wang, Recent advances in polymer and polymer composite membranes for reverse and forward osmosis processes, Progress in Polymer Science 61, 104 (2016).

[154] R. K. McGovern and J. H. Lienhard V, On the potential of forward osmosis to energetically outperform reverse osmosis desalination, Journal of Membrane Science 469, 245 (2014).

[155] A. Halperin, M. Kröger, and F. M. Winnik, Poly(N-isopropylacrylamide) Phase Diagrams: Fifty Years of Research, Angewandte Chemie International Edition 54, 15342 (2015).

[156] H. G. Schild, Poly(N-isopropylacrylamide): experiment, theory and application, Progress in Polymer Science 17, 163 (1992).

[157] T. G. Park and A. S. Hoffman, Deswelling characteristics of poly(N-isopropylacrylamide) hydrogel, Journal of Applied Polymer Science 52, 85 (1994).

[158] Q. Zhang, C. Weber, U. S. Schubert, and R. Hoogenboom, Thermoresponsive polymers with lower critical solution temperature: from fundamental aspects and measuring techniques to recommended turbidimetry conditions, Mater. Horiz. 4, 109 (2017).

[159] A. Razmjou, Q. Liu, G. P. Simon, and H. Wang, Bifunctional polymer hydrogel layers as forward osmosis draw agents for continuous production of fresh water using solar energy, Environ Sci Technol 47, 13160 (2013).

[160] J. Zeng, S. Cui, Q. Wang, and R. Chen, Multi-layer temperature-responsive hydrogel for forward-osmosis desalination with high permeable flux and fast water release, Desalination 459, 105 (2019).

[161] J. Wei, Z.-X. Low, R. Ou, G. P. Simon, and H. Wang, Hydrogel-polyurethane interpenetrating network material as an advanced draw agent for forward osmosis process, Water Research 96, 292 (2016).

[162] H. Geng, Q. Xu, M. Wu, H. Ma, P. Zhang, T. Gao, L. Qu, T. Ma, and C. Li, Plant leaves inspired sunlight-driven purifier for high-efficiency clean water production, Nat Commun 10, 1512 (2019).

[163] H. Kawaguchi, Thermoresponsive microhydrogels: preparation, properties and applications, Polymer International 63, 925 (2014).

[164] H. Kawaguchi, Functional polymer microspheres, Progress in Polymer Science 25, 1171 (2000).

[165] T. Tanaka and D. J. Fillmore, Kinetics of swelling of gels, The Journal of Chemical Physics 70, 1214 (1979).

[166] M. Andersson, Swelling kinetics of poly(N-isopropylacrylamide) gel, Journal of Controlled Release 50, 273 (1998).

[167] C. Hou, L. Ji, Q. Zhang, Y. Li, and H. Wang, Environment-sensitive carbon nanotube/polymer composite microhydrogels synthesized via a microfluidic reactor, Journal of Applied Polymer Science 127, 2422 (2013).

[168] S. A. Hashemifard, M. A. Ghanavatyan, A. Jangizehi, H. Salehi, A. Shakeri, Q. F. Alsalhy, D. Al-Timimi, C. Bantz, M. Maskos, and S. Seiffert, Challenges of forward osmosis desalination processes using hydrogels as draw agents, Journal of Membrane Science 714, 123408 (2025).

[169] A. Razmjou, M. R. Barati, G. P. Simon, K. Suzuki, and H. Wang, Fast Deswelling of Nanocomposite Polymer Hydrogels via Magnetic Field-Induced Heating for Emerging FO Desalination, Environ. Sci. Technol. 47, 6297 (2013).

[170] D. Li, X. Zhang, J. Yao, Y. Zeng, G. P. Simon, and H. Wang, Composite polymer hydrogels as draw agents in forward osmosis and solar dewatering, Soft Matter 7, 10048 (2011).

[171] K. Zhang, F. Li, Y. Wu, L. Feng, and L. Zhang, Construction of ionic thermo-responsive PNIPAM/γ-PGA/PEG hydrogel as a draw agent for enhanced forward-osmosis desalination, Desalination 495, 114667 (2020).

[172] Y. Hartanto, M. Zargar, X. Cui, B. Jin, and S. Dai, Non-ionic copolymer microgels as high-performance draw materials for forward osmosis desalination, Journal of Membrane Science 572, 480 (2019).

[173] S. N. Ellis, M. F. Cunningham, and P. G. Jessop, A forward osmosis hydrogel draw agent that responds to both heat and CO2, Desalination 510, 115074 (2021).

[174] X. Fan, H. Liu, Y. Gao, Z. Zou, V. S. J. Craig, G. Zhang, and G. Liu, Forward-Osmosis Desalination with Poly(Ionic Liquid) Hydrogels as Smart Draw Agents, Advanced Materials 28, 4156 (2016).

[175] Y. Zeng, L. Qiu, K. Wang, J. Yao, D. Li, G. P. Simon, R. Wang, and H. Wang, Significantly enhanced water flux in forward osmosis desalination with polymer-graphene composite hydrogels as a draw agent, RSC Adv. 3, 887 (2012).

[176] Y. Le, Y. Yun, M. Wang, W. Liu, S. Dong, K. Yang, S. T. Ud Din, W. Yang, and G. Liu, N-isopropyl acrylamide/sodium acrylate hydrogel as draw agent for forward osmosis to concentrate esterification wastewater, Korean J. Chem. Eng. 38, 975 (2021).

[177] Y. M. Mohan, T. Premkumar, D. K. Joseph, and K. E. Geckeler, Stimuli-responsive poly(N-isopropylacrylamide-co-sodium acrylate) hydrogels: A swelling study in surfactant and polymer solutions, Reactive and Functional Polymers 67, 844 (2007).

[178] X. Xu, H. Li, J. Cheng, L. Zhang, and Z. Cheng, Thermo-sensitive hydrogels for forward osmosis with NIR light-induced freshwater recovery, Polym. Chem. 14, 697 (2023).

[179] X. Xu, S. Ozden, N. Bizmark, C. B. Arnold, S. S. Datta, and R. D. Priestley, A Bioinspired Elastic Hydrogel for Solar-Driven Water Purification, Advanced Materials 33, 2007833 (2021).

[180] D. Duracher, A. Elaïssari, and C. Pichot, Preparation of poly(N-isopropylmethacrylamide) latexes kinetic studies and characterization, Journal of Polymer Science Part A: Polymer Chemistry 37, 1823 (1999).

[181] N. Kato and F. Takahashi, Acceleration of deswelling of NIPAM Hydrogel by the Treatment of a Freeze-Dry and Hydration Process, Bull. Chem. Soc. Jpn 70, 1289 (1997).

[182] N. Kato, Y. Takizawa, and F. Takahashi, Magnetically Driven Chemomechanical Device with Poly(N-isopropylacrylamide) Hydrogel Containing γ-Fe2O3, Journal of Intelligent Material Systems and Structures 8, 588 (1997).

[183] J. A. Galicia, F. Cousin, E. Dubois, O. Sandre, V. Cabuil, and R. Perzynski, Static and dynamic structural probing of swollen polyacrylamide ferrogels, Soft Matter 5, 2614 (2009).

[184] N. S. Satarkar and J. Z. Hilt, Magnetic hydrogel nanocomposites for remote controlled pulsatile drug release, Journal of Controlled Release 130, 246 (2008).

[185] M. A. Kim, S. D. Yoon, J. S. Lee, and C.-M. Lee, Melanin-PEG nanoparticles as a photothermal agent for tumor therapy, Materials Today Communications 25, 101575 (2020).

[186] B. Sun, Y. Lin, P. Wu, and H. W. Siesler, A FTIR and 2D-IR Spectroscopic Study on the Microdynamics Phase Separation Mechanism of the Poly(N-isopropylacrylamide) Aqueous Solution, Macromolecules 41, 1512 (2008).

[187] E. C. Cho, J. Lee, and K. Cho, Role of Bound Water and Hydrophobic Interaction in Phase Transition of Poly(N-isopropylacrylamide) Aqueous Solution, Macromolecules 36, 9929 (2003).

[188] S. Sun, J. Hu, H. Tang, and P. Wu, Chain Collapse and Revival Thermodynamics of Poly(N-isopropylacrylamide) Hydrogel, J. Phys. Chem. B 114, 9761 (2010).

[189] J. E. House, *Principles of Chemical Kinetics* (Elsevier Science & Technology, San Diego, UNITED STATES, 2007).

[190] K. J. Laidler, Unconventional applications of the Arrhenius law, J. Chem. Educ. 49, 343 (1972).

[191] B. Vázquez, J. San Roman, C. Peniche, and M. E. Cohen, Polymeric Hydrophilic Hydrogels with Flexible Hydrophobic Chains. Control of the Hydration and Interactions with Water Molecules, Macromolecules 30, 8440 (1997).

[192] P. Rahimi Borujerdi, B. Shotorban, S. Mahalingam, and D. R. Weise, Modeling of water evaporation from a shrinking moist biomass slab subject to heating: Arrhenius approach versus equilibrium approach, International Journal of Heat and Mass Transfer 145, 118672 (2019).

[193] A. Percq, D. Dubois, and J. W. Nicholson, Water Transport in Resin-modified Glass-ionomer Dental Cement, J Biomater Appl 23, 263 (2008).

[194] K. C. Waugh, Prediction of global reaction kinetics by solution of the Arrhenius parameterised component elementary reactions: microkinetic analysis, Catalysis Today 53, 161 (1999).

[195] J. F. Brennan, J. S. Shapiro, and E. C. Watton, Evaporation of liquids: A kinetic approach, J. Chem. Educ. 51, 276 (1974).

[196] Z. Wang and E. G. Seebauer, Estimating pre-exponential factors for desorption from semiconductors: consequences for a priori process modeling, Applied Surface Science 181, 111 (2001).

[197] A. Bar, O. Ramon, Y. Cohen, and S. Mizrahi, Shrinkage behaviour of hydrophobic hydrogel during dehydration, Journal of Food Engineering 55, 193 (2002).

[198] S. Khalloufi and P. Bongers, Mathematical investigation of the case hardening phenomenon explained by shrinkage and collapse mechanisms occurring during drying processes, Computer Aided Chemical Engineering 30, 1068 (2012).

[199] R. Steffen, G. Wallner, J. Rekstad, and B. Röder, General characteristics of photoluminescence from dry heat aged polymeric materials, Polymer Degradation and Stability 134, 49 (2016).

[200] R. Steffen, M. Meir, J. Rekstad, and B. Röder, Kinetics of degradation-induced polymer luminescence: A polyphenylene sulfide/elastomer blend under dry heat exposure, Polymer 136, 71 (2018).

[201] R. Tian, K. Li, Y. Lin, C. Lu, and X. Duan, Characterization Techniques of Polymer Aging: From Beginning to End, Chem. Rev. 123, 3007 (2023).

[202] M. Teodorescu, M. Bercea, and S. Morariu, Biomaterials of PVA and PVP in medical and pharmaceutical applications: Perspectives and challenges, Biotechnology Advances 37, 109 (2019).

[203] C. C. DeMerlis and D. R. Schoneker, Review of the oral toxicity of polyvinyl alcohol (PVA), Food and Chemical Toxicology 41, 319 (2003).

[204] N. Hameed, V. Glattauer, and J. A. M. Ramshaw, Evaluation of polyvinyl alcohol composite membranes containing collagen and bone particles, Journal of the Mechanical Behavior of Biomedical Materials 48, 38 (2015).

[205] E. Chiellini, A. Corti, S. D'Antone, and R. Solaro, Biodegradation of poly (vinyl alcohol) based materials, Progress in Polymer Science 28, 963 (2003).

[206] Y. Mori, T. Honda, R. Lu, N. Hayakawa, and T. Miyakoshi, Ultraviolet degradation of poly(vinyl alcohol) used in restoration of historical and cultural properties, Polymer Degradation and Stability 114, 30 (2015).

[207] K.-J. Kim, Y.-H. Yun, J.-Y. Je, D.-H. Kim, H. S. Hwang, and S.-D. Yoon, Photothermally controlled drug release of naproxen-incorporated mungbean starch/PVA biomaterials adding melanin nanoparticles, Process Biochemistry 129, 268 (2023).

[208] B. Narasimhan and N. A. Peppas, Molecular Analysis of Drug Delivery Systems Controlled by Dissolution of the Polymer Carrier, Journal of Pharmaceutical Sciences 86, 297 (1997).

[209] Y. Wang, Z. Wang, Y. Liu, T. Li, P. Ma, H. Bai, Y. Xie, M. Chen, and W. Dong, Structure and thermal behaviors of poly(vinyl alcohol)/surfactant composites: Investigation of molecular interaction and mechanism, Polymers for Advanced Technologies 29, 2224 (2018).

[210] Y. Wang, Z. Wang, P. Ma, H. Bai, W. Dong, Y. Xie, and M. Chen, Strong nanocomposite reinforcement effects in poly(vinyl alcohol) with melanin nanoparticles, RSC Adv. 5, 72691 (2015).

[211] H. Yang, S. Xu, L. Jiang, and Y. Dan, Thermal Decomposition Behavior of Poly (Vinyl Alcohol) with Different Hydroxyl Content, Journal of Macromolecular Science, Part B 51, 464 (2012).

[212] A. Uda, S. Morita, and Y. Ozaki, Thermal degradation of a poly(vinyl alcohol) film studied by multivariate curve resolution analysis, Polymer 54, 2130 (2013).

[213] P. S. Thomas, J.-P. Guerbois, G. F. Russell, and B. J. Briscoe, FTIR Study of the Thermal Degradation of Poly(vinyl Alcohol), Journal of Thermal Analysis and Calorimetry 64, 501 (2001).

[214] B. J. Holland and J. N. Hay, The thermal degradation of poly(vinyl alcohol), Polymer 42, 6775 (2001).

[215] J. Wang, L. Xu, S. Zhong, Y. Yang, G. Feng, Q. Meng, Y. Gao, and X. Cui, Clustering-triggered emission of poly(vinyl) alcohol, Polym. Chem. 12, 7048 (2021).

[216] S. Ram and T. K. Mandal, Photoluminescence in small isotactic, atactic and syndiotactic PVA polymer molecules in water, Chemical Physics 303, 121 (2004).

[217] K. K. Dey, P. Kumar, R. R. Yadav, A. Dhar, and A. K. Srivastava, CuO nanoellipsoids for superior physicochemical response of biodegradable PVA, RSC Adv. 4, 10123 (2014).

[218] J. Mieloszyk, R. Drabent, and J. Siódmiak, Phosphorescence and fluorescence of poly(vinyl alcohol) films, Journal of Applied Polymer Science 34, 1577 (1987).

[219] E. Kitchner, M. Seung, J. Chavez, L. Ceresa, J. Kimball, I. Gryczynski, and Z. Gryczynski, Fluorescence measurements: importance of G-factor correction, magic angle, and observation wavelengths, Methods Appl. Fluoresc. 10, 043001 (2022).

[220] Z. Gryczynski and I. Gryczynski, *Practical Fluorescence Spectroscopy* (CRC Press, Boca Raton, 2019).

[221] W. Dong, Y. Wang, C. Huang, S. Xiang, P. Ma, Z. Ni, and M. Chen, Enhanced thermal stability of poly(vinyl alcohol) in presence of melanin, J Therm Anal Calorim 115, 1661 (2014).

[222] J. Luo et al., Aggregation-induced emission of 1-methyl-1,2,3,4,5-pentaphenylsilole, Chem. Commun. 1740 (2001).

[223] J. M. Gallas and M. Eisner, Fluorescence of Melanin-Dependence Upon Excitation Wavelength and Concentration, Photochemistry and Photobiology 45, 595 (1987).

[224] B. Fernandes, T. Matamá, D. Guimarães, A. Gomes, and A. Cavaco-Paulo, Fluorescent quantification of melanin, Pigment Cell Melanoma Res 29, 707 (2016).

[225] T. Sarna and H. A. Swartz, *The Physical Properties of Melanins*, in *The Pigmentary System*, edited by J. J. Nordlund, R. E. Boissy, V. J. Hearing, R. A. King, W. S. Oetting, and J.-P. Ortonne (Blackwell Publishing Ltd, Oxford, UK, 2006), pp. 311–341.

[226] G. Perna, M. C. Frassanito, G. Palazzo, A. Gallone, A. Mallardi, P. F. Biagi, and V. Capozzi, Fluorescence spectroscopy of synthetic melanin in solution, Journal of Luminescence 129, 44 (2009).

[227] P. Kayatz, G. Thumann, T. T. Luther, J. F. Jordan, K. U. Bartz–Schmidt, P. J. Esser, and U. Schraermeyer, Oxidation Causes Melanin Fluorescence, Investigative Ophthalmology & Visual Science 42, 241 (2001).

[228] B. J. Holland and J. N. Hay, The thermal degradation of poly(vinyl acetate) measured by thermal analysis–Fourier transform infrared spectroscopy, Polymer 43, 2207 (2002).

[229] T. Sarna, J. M. Burke, W. Korytowski, M. Różanowska, C. M. B. Skumatz, A. Zaręba, and M. Zaręba, Loss of melanin from human RPE with aging: possible role of melanin photooxidation, Experimental Eye Research 76, 89 (2003).

[230] G. Su, C. Yang, and J.-J. Zhu, Fabrication of Gold Nanorods with Tunable Longitudinal Surface Plasmon Resonance Peaks by Reductive Dopamine, Langmuir 31, 817 (2015).

[231] O. N. Tretinnikov and S. A. Zagorskaya, Determination of the degree of crystallinity of poly(vinyl alcohol) by FTIR spectroscopy, J Appl Spectrosc 79, 521 (2012).

[232] J. Xu, B.-H. Guo, R. Yang, Q. Wu, G.-Q. Chen, and Z.-M. Zhang, In situ FTIR study on melting and crystallization of polyhydroxyalkanoates, Polymer 43, 6893 (2002).

[233] A. Xiang, C. Lv, and H. Zhou, Changes in Crystallization Behaviors of Poly(Vinyl Alcohol) Induced by Water Content, Journal of Vinyl and Additive Technology 26, 613 (2020).

[234] C. E. Macias, H. Bodugoz-Senturk, and O. K. Muratoglu, Quantification of PVA hydrogel dissolution in water and bovine serum, Polymer 54, 724 (2013).

[235] S. I. Song and B. C. Kim, Characteristic rheological features of PVA solutions in water-containing solvents with different hydration states, Polymer 45, 2381 (2004).

[236] S. K. Mallapragada and N. A. Peppas, Dissolution mechanism of semicrystalline poly(vinyl alcohol) in water, Journal of Polymer Science Part B: Polymer Physics 34, 1339 (1996).